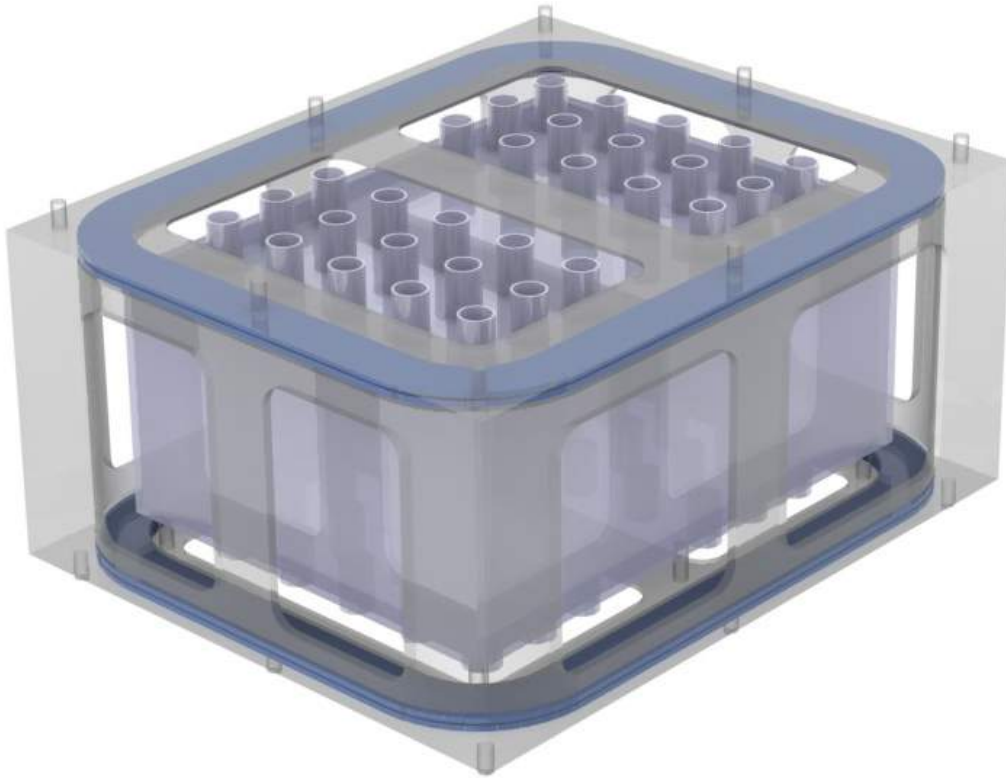


Design Optimization of a new Superconducting Magnet System for a LAr Neutrino Detector

*A technical design report performed within the framework of a bachelor assignment as part of the
Advanced Technology bachelor programme at the ATLAS magnet group at CERN.*



L.Y. van Dijk

Date

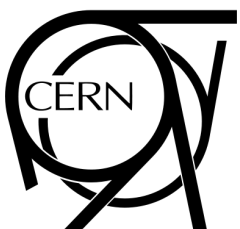
July 15, 2014

Examination Committee

Prof. Dr. Ir. Herman ten Kate

Dr. Ir. Herbert Wormeester

Dr. Marc Dhallé



UNIVERSITY OF TWENTE.

Abstract

This report presents a design optimization of a new superconducting magnet system for a liquid Argon neutrino detector. The optimization study is performed within the framework of a bachelor assignment as part of the Advanced Technology bachelor programme at the ATLAS magnet group at CERN.

For the design of the superconducting magnet system, two options are investigated. A double racetrack configuration and a uniformly wound solenoid. As a basis for the optimization study, a pre-existing Matlab based design tool named Field is used. The optimization study is performed by making use of the text based interface of Field and consists of a single optimization cycle accompanied by a parametric sweep. The result of the optimization study is a set of optimized models for both the double racetrack and the solenoid option. As a result of the performed parametric sweeps, all models have a different geometry and satisfy different design requirements. To be able to continue the design study, a so-called working model is selected for both configurations. Further analysis concerning the thermal and mechanical behaviour of both design options is performed with respect to these working models.

Contents

Contents	1
1 Introduction	3
1.1 Fundamental Particles	3
1.1.1 Standard Model	3
1.1.2 CERN and the LHC	4
1.2 Neutrino Detection	5
1.2.1 The Neutrino	5
1.2.2 Liquid Argon detector	5
1.3 Design Requirements	6
1.4 Assignment and Chapter Layout	6
2 Superconductivity and Magnet Design	7
2.1 Superconductivity and the Critical Surface	7
2.1.1 Niobium Titanium	8
2.1.2 Magnesium di-Boride	8
2.2 Magnetic Field	8
2.2.1 Emf and Inductance	8
2.2.2 Stored Energy	9
2.2.3 Lorentz Force	9
2.3 Design Concepts	9
2.3.1 Superconducting Coil	9
2.3.2 Current density	11
2.3.3 Stability and Quenching	12
2.3.4 Forces and Structures	13
2.3.5 Cryogenics	13
2.4 Magnetic Field Calculation	13
3 Numerical Method	15
3.1 Geometry Definition	15
3.1.1 Geometrical Parameters	15
3.1.2 Field Parameters	15
3.2 Current Density Calculation Method	15
3.3 Optimization Algorithm	17
3.3.1 Targets and Variables	17
3.3.2 Parameter Sweep	18
3.3.3 Optimization Cycle	18
3.4 Conclusion	19
4 Double Racetrack Layout Optimization	20
4.1 Conductor Settings	20
4.2 Design Choices	21
4.3 Parametric Study	22
4.3.1 L1 and L2	22
4.3.2 R and Bedgereg	26
4.3.3 General results	28

4.4	Working Model and Analysis	30
4.4.1	Magnetic Field	30
4.4.2	Magnetic peak field reduction	30
4.5	Conclusion	35
5	Solenoid Layout Optimization	36
5.1	Conductor Settings	36
5.2	Design Choices	36
5.3	Parametric Study R and hcoil	37
5.4	Working Model and Analysis	39
5.4.1	Magnetic Field	39
5.5	Conclusion	41
6	Quench Analysis	42
6.1	Determination of the average temperature rise	42
6.1.1	Influence of the stabfactor	43
6.2	Determination of the peak temperature	44
6.2.1	Influence of an external dump resistor and quench heaters	45
6.3	Comparison of the quench model	49
6.4	Conclusion	49
7	Mechanical Analysis	51
7.1	Forces	51
7.2	Structure	51
7.3	Deformation and Von Mises stress	53
7.3.1	Von Mises stress	53
7.3.2	Deformation	53
7.4	Conclusion	55
	Conclusion	56
	Discussion and Recommendations	57
	Acknowledgements	59
	Bibliography	59
A	Field Harmonics	61
B	Data Tables	63
B.1	Double racetrack configuration: Parametric study R and Bedgereq	63
B.2	Double racetrack configuration: Parametric study L1 and L2	65
B.3	Solenoid configuration: Parametric study R and hcoil	66

1 Introduction

This report presents a design optimization of a new superconducting magnet system for a liquid Argon neutrino detector. The optimization study is performed within the framework of a bachelor assignment as part of the Advanced Technology bachelor programme at the ATLAS magnet group at CERN. In this chapter an introduction is given to particle physics, CERN, neutrino detection, the design requirements and the assignment itself.

1.1 Fundamental Particles

1.1.1 Standard Model

The standard model of particle physics (figure 1.1) is a theory that describes the basic building blocks our universe is made of and the forces that govern their interactions. It was developed during the late 1970s as a collaborative effort of scientists around the world. The model predicted the existence of the bottom quark, the top quark, the tau neutrino and the Higgs boson. Confirmed to exist experimentally in respectively 1977, 1995, 2000 and 2013. Because of its success in explaining a wide variety of experimental results, the standard model is sometimes called the ‘theory of almost everything’. However, the standard model falls short of being complete since it does not incorporate the full theory of gravitation and neither accounts for the accelerating expansion of the universe.

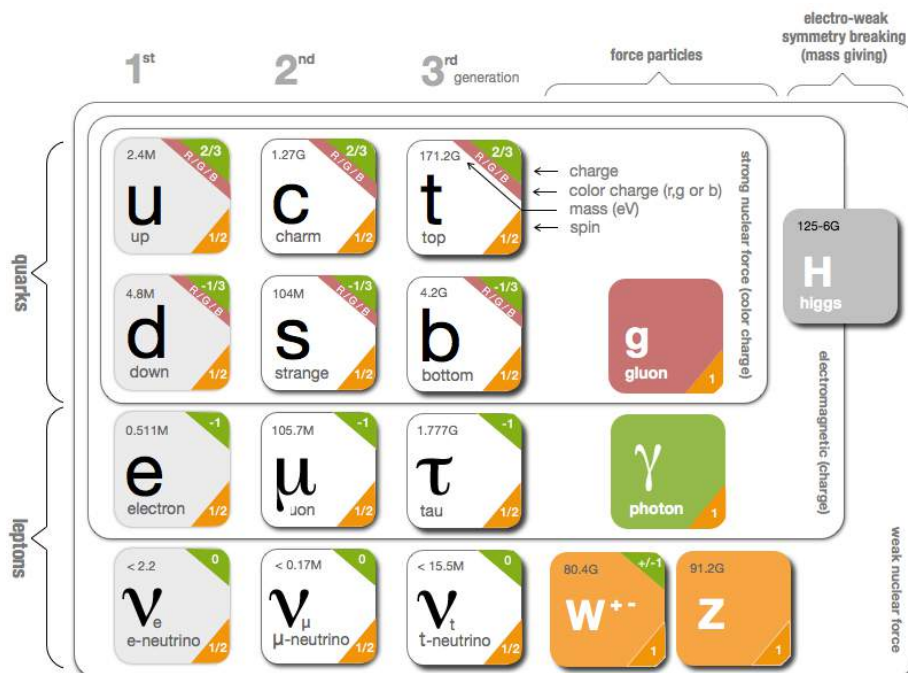


Figure 1.1: Standard model of particle physics. Reprinted from ISGTW [1].

1.1.2 CERN and the LHC

One of the largest institutes involved in particle physics is the 'European Council for Nuclear Research', better known as CERN. It was founded in 1954 by 12 Western European countries and is located on the Franco-Swiss border near Geneva. CERN's main function is to provide particle accelerators and other infrastructure needed for high-energy physics research. The institute accommodates an accelerator complex which is a succession of machines that accelerate particles to increasingly higher energies. Each machine boosts the energy of a beam of particles, before injecting the beam into the next accelerator in the sequence. The last element in this chain is the Large Hadron Collider (LHC) which is the world's largest and most powerful circular particle accelerator. The LHC was first operated in 2008, is located 100 m underground and has a total circumference of 27 km. Inside the accelerator, two high-energy proton beams travel in opposite directions. The beams are guided around the ring by a strong magnetic field, maintained by superconducting magnets. The LHC accommodates seven experiments of which four are located at the ring (see figure 1.2). All experiments are organized independently from CERN and the LHC and are supported by different collaborations of institutes and countries.

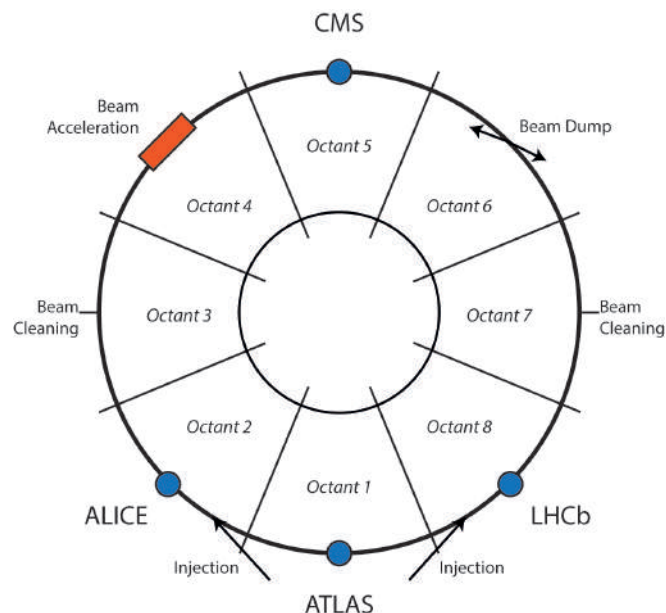


Figure 1.2: Schematic representation of the Large Hadron Collider (LHC) located at CERN. Adapted from van Nugteren [2].

The ATLAS detector

ATLAS (A Toroidal LHC Apparatus) is one of the four experiments located at the LHC ring. With a length of 46 m and a height of 25 m it is the largest and most elaborate particle detector ever constructed. It is used to investigate many different types of physics that might become detectable in the energetic collisions of the LHC. One of the most important goals of ATLAS was the search for the Higgs boson, which was confirmed to exist in March 2013. The detector consists of a series of concentric cylinders positioned around the interaction point where the LHC beams collide. It can be divided in four major parts: the inner detector, the magnet system, the Muon spectrometer and the calorimeters (see figure 1.3). The magnet system provides a magnetic field which is used to determine the momenta of the particles that emerge during the collisions. It is composed of four large superconducting magnets, one Barrel Toroid, two End Cap Toroids and one Central Solenoid.

1.2 Neutrino Detection

1.2.1 The Neutrino

One of the particles described by the standard model (figure 1.1) is the neutrino (ν). It was introduced by Wolfgang Pauli in 1931 to explain the conservation of energy, momentum and angular momentum during beta decay. A neutrino is an electrically neutral particle with a relatively small mass. Its interactions are governed by the weak sub-atomic force, which is of much shorter range than electromagnetism and gravity. Therefore a typical neutrino passes through normal matter unimpeded. Due to their electrical neutrality, neutrinos are very hard to detect. There are three types (or flavours) of neutrinos: electron neutrinos (ν_e), muon neutrinos (ν_μ) and tau neutrinos (ν_τ). For each type there is an associated antiparticle, the antineutrino. A very interesting phenomenon predicted by Bruno Pontecorvo is neutrino oscillation, which describes the oscillation of neutrinos among the three available flavours while they propagate through space [3].

1.2.2 Liquid Argon detector

Although neutrinos are very hard to detect, it is possible to study them by means of large, specialized detectors. One type of detectors is the Liquid Argon Time Projection Chamber (LAr TPC). This technology, proposed by Carlo Rubbia in 1977, was implemented for the first time in the ICARUS experiment located at Gran Sasso. An LAr TPC is a tracking detector and consists of a large volume of liquid Argon which is used as a target material [4]. Incoming neutrinos interact with the Argon, producing leptons corresponding to their flavours. The leptons will ionize the Argon, creating ionization electrons which are collected on wire planes. Based on the information acquired by the wire planes, a 3D view of the neutrino interaction can be constructed. However, this view provides no information concerning the identities of the particles, which is useful for studying phenomena such as neutrino oscillation. To make particle identification possible, the detector is placed in a magnetic field. By measuring the bending of the particles due to the magnetic field, the momenta and therefore the identity of the particles can be determined.

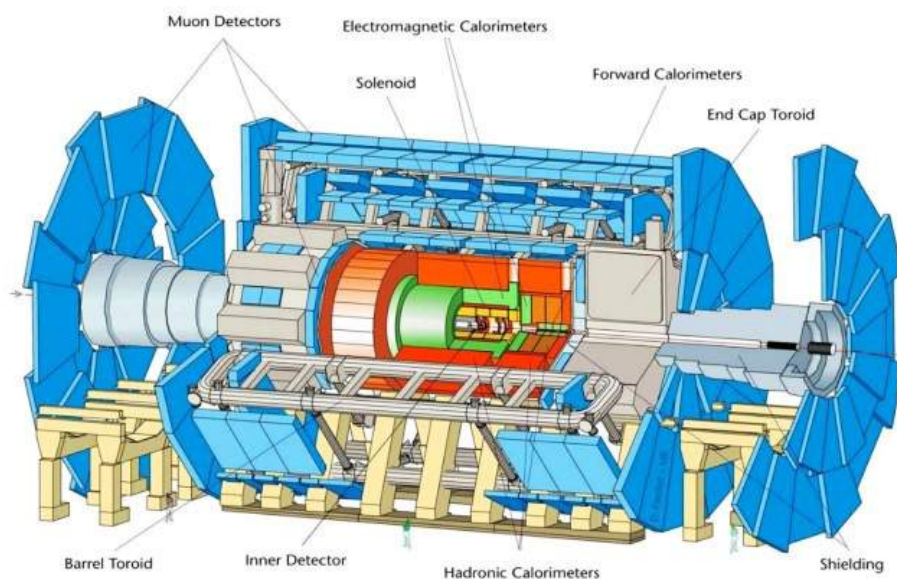


Figure 1.3: Schematic representation of the ATLAS detector. Reprinted from the ATLAS Experiment [5].

1.3 Design Requirements

As part of CERN's effort to strengthen the research of neutrino based particle physics, a proposition was made for a new liquid Argon neutrino detector. The design of the superconducting magnet system, which is part of the total detector configuration, was assigned to the ATLAS magnet group. This section describes the relevant detector specifications and design requirements.

The neutrino detector exists of a cubic liquid Argon vessel which is surrounded by a cryostat. The dimensions of this combined system are 12 m x 9 m x 5 m (length x width x height). To isolate the detector from cosmic rays and other background radiation, the neutrino detector will be placed in an underground cavern. Since the construction of such a cavern is expensive, it is desirable to keep the dimensions of the total system as small as possible. The superconducting magnet system needs to satisfy the following requirements:

- The magnitude of the magnetic field at the center of the detector volume has to be 1 T.
- The magnitude of the field at the edge of the detector volume can not be smaller than 0.5 T.
- The magnetic field inside the detector volume should be homogeneous. Note that this is quantified by the second argument.
- The system has to be designed in such a way that it does not intersect the liquid Argon vessel.
- The design has to be scalable in length.
- The system has to be designed in such a way that the detector volume is accessible from the top.
- The design has to be simple, cheap and its production time should be short.

1.4 Assignment and Chapter Layout

The objective of this bachelor assignment is to perform a design optimization for the superconducting magnet system of a new LAr neutrino detector. An introduction to the basic concepts of superconductivity and superconducting magnet design is presented in chapter 2. The numerical method used to perform the optimization study is described in chapter 3. For the design of the superconducting magnet system of the LAr neutrino detector, two options are proposed. The first one is a double racetrack configuration which uses Nb-Ti as a superconductor and has an operating temperature of 4.5 K. The optimization study performed for this design is presented in chapter 4. The second option is based on a uniformly wound solenoid which uses MgB_2 as a superconductor and has an operating temperature of 20 K. The optimization study performed for this design is presented in chapter 5. The result of the optimization studies is a set of optimized models for both the double racetrack and solenoid option. To perform further analysis, a so-called working model is selected for both configurations. Chapter 6 provides an analysis of the thermal behaviour of both working models and an analysis of the mechanical properties of both working models is presented in chapter 7.

2 Superconductivity and Magnet Design

Superconducting magnets are often used instead of normal electromagnets for the generation of magnetic fields above 1 T. Since the power dissipation of a normal electromagnet becomes very large for high fields, extreme cooling methods are required. Application of normal electromagnets is therefore in most cases undesirable. This chapter introduces the basic concepts of superconductivity, magnetic fields and superconducting magnet design. Furthermore, it gives a description of Field, a pre-existing Matlab based design tool which is used for all magnetic field calculations performed in this report.

2.1 Superconductivity and the Critical Surface

Superconductivity is a phenomenon that causes the electrical resistivity in certain materials to reduce to zero below a so called critical temperature. It was discovered in 1911 by Dutch physicist Kamerling Onnes who tried to determine the electrical properties of Mercury at cryogenic temperatures experimentally. Unfortunately it is not feasible to run an infinite current inside a superconductor. The current density inside the superconductor is limited at the critical current density (J_c) above which the superconductor is saturated. This critical current is in essence the boundary between superconductivity and normal resistivity and can be visualized using the critical surface, which shows the critical current density as a function of the temperature and the applied magnetic field (figure 2.1). The critical field (B_c), critical temperature (T_c) and critical current density are material properties and therefore the shape of the critical surface is specific for each material.

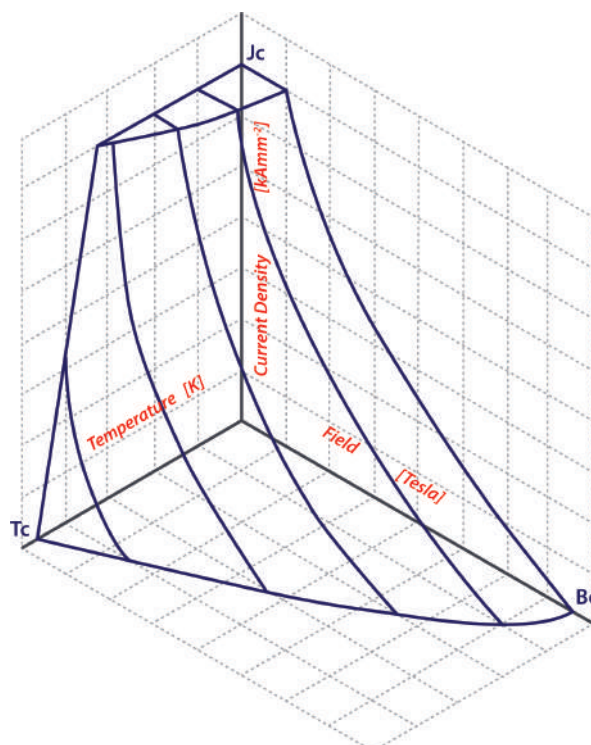


Figure 2.1: Critical surface of Niobium Titanium. Adapted from Wilson [6].

2.1.1 Niobium Titanium

Niobium Titanium (Nb-Ti) is the most commonly used superconductor over the last decades and has been successfully implemented in the LHC and the ATLAS magnet system. Its superconducting properties were discovered in 1962 by Berlincourt and Hake [7]. Nb-Ti is a ductile alloy, which makes production and application relatively easy. It has a critical temperature of 9.2 K and can remain superconductive in magnetic fields up to 15 T. Because some margin is needed the practical limit for magnets lies around 10 T. The critical surface of Nb-Ti is calculated using the Bottura scaling relation [8] and is presented by figure 2.1.

2.1.2 Magnesium di-Boride

The superconducting properties of Magnesium di-Boride (MgB_2) were discovered in early 2001. In spite of its recent discovery, several practical applications of MgB_2 as a conductor have already been realized. For example, in 2006 an MgB_2 -based magnet was successfully implemented in an MRI system [9]. However, it is important to note that these applications concern only relatively small systems. A large scale application of MgB_2 as a conductor has yet not been accomplished. MgB_2 has a critical temperature of 39 K and can remain superconductive in magnetic fields up to 20-25 T at 4.2 K and 25-30 T at 0 K [10]. The calculation of the critical surface of MgB_2 is based on the Fietz-and-Webb scaling type [11], adapted for MgB_2 [12].

2.2 Magnetic Field

A magnetic field is produced by moving charges such as a current in a wire. It is a vector field which is at any given point in space specified by a direction and a magnitude. The magnetic field is denoted by the symbol \vec{B} and its magnitude is measured in Tesla (T). A very convenient way for calculation of magnetic fields generated by steady line currents is the Biot-Savart law (section 2.4). The theory of magnetic fields is a very important part of magnet design. This section introduces a few basic concepts of magnetic field theory relevant to the design study performed in this report.

2.2.1 Emf and Inductance

The phenomenon that is responsible for the circulation of charges in an electric circuit is the electromotive force (emf). The emf is defined as the tangential force per unit charge in a wire integrated over the length of the complete circuit. It is actually not a 'real' force, but can be seen as the work done per unit charge [13]. Faraday discovered that whenever the magnetic flux through a loop changes an emf will appear in the loop. In other words a changing magnetic field induces an electric field. Since magnetic fields are created by currents, it can be stated that a changing current induces a voltage (which is an emf). The voltage induced in a loop by a changing current is described by

$$V = L \frac{dI}{dt}, \quad (2.1)$$

where V is the induced voltage, $\frac{dI}{dt}$ is the change of current per unit time in the circuit and L is a constant of proportionality which is called the self-inductance (or simply the inductance) that depends on the geometry of the current loop [14]. A changing current can also induce a voltage in any nearby loops in the same way it induces a voltage in the source loop itself. This is called mutual inductance (M) and just like L , it depends on the geometry (and orientation) of the loops.

2.2.2 Stored Energy

To start a current flowing in an electrical circuit a certain amount of work has to be done against the back emf to get the current going [13]. This energy is stored in the magnetic field and can be recovered when the current is turned off. The stored energy (E_{st}) is given by

$$E_{st} = \frac{1}{2}LI^2, \quad (2.2)$$

where L is the self inductance of the circuit and I is the current. Note that the amount of energy stored in the circuit is independent of the time it takes to build up the current.

2.2.3 Lorentz Force

A moving charged particle experiences electromagnetic forces when placed in an electromagnetic field. The total electromagnetic force on a charged particle can be described by the Lorentz force [14] which is a combination of the electric and magnetic force and is given by

$$\vec{F} = q(\vec{E} + \vec{v} \times \vec{B}), \quad (2.3)$$

where q is the charge of the particle, \vec{E} is the electric field vector, \vec{v} is the velocity vector of the charged particle and \vec{B} is the magnetic field vector. The right side of the formula presents the magnetic force which clearly depends on the velocity of the charged particle. The magnetic force exerted on a current-carrying wire placed in a magnetic field can be derived by looking at a number of charged particles moving with the velocity v along the wire. The force per unit volume can then be described by

$$\vec{F} = \vec{J} \times \vec{B}, \quad (2.4)$$

where \vec{J} is the current density vector, \vec{B} is the magnetic field vector and \vec{F} is the volumetric force in $\frac{N}{m^3}$. Note that the magnetic force on a wire due to moving charges only depends on the total current.

2.3 Design Concepts

Superconducting magnet design is an engineering challenge that combines the knowledge of multiple disciplines such as cryogenics, mechanical engineering and electrical engineering. Because of its multidisciplinary character, superconducting magnet design is a very complex discipline, which therefore is very interesting, but also very hard to study. This section provides a brief introduction to the basic concepts of magnet design relevant to the design study performed in this report.

2.3.1 Superconducting Coil

A superconducting magnet consists of one or multiple coils combined in a specific way regarding the purpose of the magnet. Each coil is wound using multiple turns of either a cable or, for smaller magnets, a wire. Although superconducting materials form the basis for operation of superconducting magnets, the conductor itself does not exclusively exist of it. For thermodynamic reasons (described in section 2.3.3), superconducting materials are always used in combination with a good normal conductor. By looking at

the structure of the coil windings two different parts can be distinguished, the cable and the conductor. The composition and functions of both parts are described in the next paragraphs.

Conductor

The name conductor is used to describe the overall structure of a superconducting coil winding. Figure 2.2 presents a schematic drawing of the cross section of the ATLAS Barrel Toroid conductor [15]. It consists of a superconducting cable, illustrated by the blue square, a good normal conductor that serves as a stabilizer (in this case pure Aluminium), illustrated by the grey square and an insulation layer to preserve the electric current in the conductor volume. Furthermore, a small percentage of the conductor volume is considered as void. The conductor can be constructed in many different geometrical shapes and sizes, depending on the requirements for the coil.

Cable

A superconducting cable exists of multiple strands that are combined in a specific configuration. The current through each strand is limited (typical values are 100-500 A), therefore the number of strands depends on the required current density of the magnet system (for large systems in the order of 10-100 kA). To ensure intimate mixing between the superconductor and the normal conductor in the strands, the superconductor is constructed in the form of fine filaments which are embedded in a so called matrix of the normal conductor. For the ATLAS Barrel Toroid conductor (figure 2.2), a Copper matrix is used. The ratio between the volume of superconductor and the volume of normal conductor in the cable is named the Cu/Sc ratio. The cable strands (illustrated by the blue circles in figure 2.2) all carry a large current which generate a magnetic self field. When the strands are closely packed together, the self field generates a magnetic flux between the neighbouring strands. To avoid flux linkage between the filaments the individual strands are twisted around their symmetry axis. The length over which a strand is fully twisted is indicated by the twist pitch. Unfortunately, twisting the strands does not prevent flux linkage between the different strands themselves since their position relative to the other strands does not change. In order to prevent flux linkage between the strands, the strands have to be fully transposed. This means that every strand has to change places with all other strands along the length of the cable so that on average the total enclosed flux is zero. The length over which all strands are transposed once is indicated by the transposition pitch.

There are multiple types of superconducting cables. Two examples are the Rutherford cable and the Cable-in-Conduit Conductor (CICC). A Rutherford cable is a fully transposed and flattened cable that contains 12-40 twisted strands of 0.8-1.2 mm diameter. The cable is cooled by a bath and is mostly used in accelerator magnets. A CICC contains 100-1000 strands of 0.8-1.0 mm diameter which are twisted, transposed and inserted in a stainless steel tube. The strands are cooled by a forced flow of Helium through the tube. This type of cable is mostly used for fusion and large scale laboratory magnets, such as the ITER magnet system.

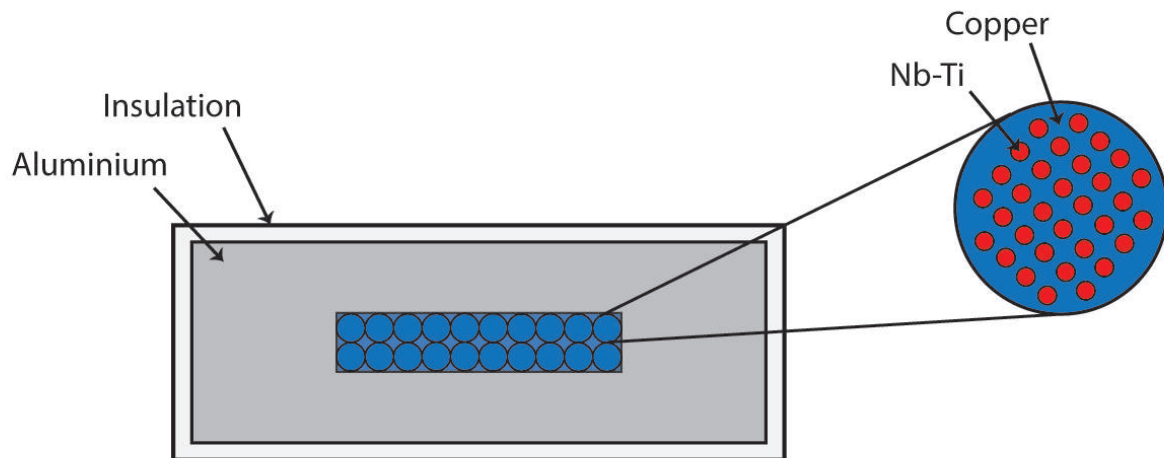


Figure 2.2: Schematic representation of the cross section of the ATLAS Barrel Toroid conductor [15]. The conductor consists of pure Aluminium as a stabilizer, an insulation layer of epoxy impregnated glass fiber ribbon and a Rutherford cable composed of Nb-Ti filaments embedded in a Copper matrix.

Double Pancake winding

A commonly used configuration for superconducting coils is the so called double pancake winding (figure 2.3). It is a combination of two layers of conductor on top of each other separated by a thin layer of insulation. The advantage of this particular configuration is that it simplifies the electrical connections, which are by making use of this set up, only located on the outside of the coil. Another advantage of stacking multiple conductor decks is that a larger magnetic field can be created, while the width of the coil is kept small. Therefore, this type of configuration is in many cases (like the ATLAS Barrel Toroid) a very convenient choice.

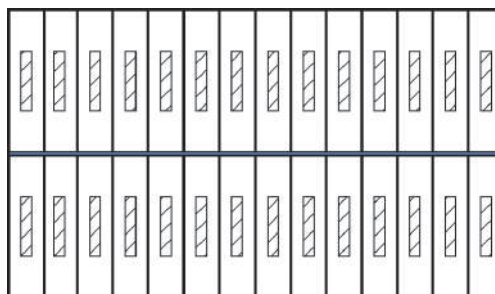


Figure 2.3: Schematic representation of a double pancake configuration. Two conductor decks are placed on top of each other with an insulation layer in between.

2.3.2 Current density

In the field of magnet design three different types of current density are used to indicate the amount of current flowing through a specific area. The first one is the critical current density (J_c) which is an upper limit for the current density inside the superconductor itself (as explained in section 2.1). The second one is the engineering current density (J_{eng}), which is the critical current at the average operating temperature over the cross section of the superconducting cable, stabilizer and insulation. The engineering current density is much lower than the critical current density. The last type is the operating current density (J_{op}) which is the current density that is used for operating the superconducting magnet. The operating current density is obtained by applying a safety margin to the engineering current density (see section 3.2).

2.3.3 Stability and Quenching

To maintain the superconducting state, the conductor has to be operated below the critical surface which is determined by the critical current, critical magnetic field and critical temperature. Due to various reasons a magnet can quench, which happens when the superconducting material undergoes a sudden, unexpected and unrecoverable transition to the normal state. This sudden transition enforces the energy stored in the magnetic field to converse into mostly heat, which can lead to destruction of the magnet. It is therefore very important to impose safety measures to protect the magnet system.

A quench can be caused by multiple events. It could for instance originate from internal problems, such as design flaws or wire movement, but also from external problems such as a control system error or radiation. Although quenching should generally be avoided, it is part of 'normal operation' of a magnet and therefore should be considered explicitly during the design process. The design adjustments that have to be made in order to avoid quenching can be separated in two groups, one for prevention and one for protection. The following paragraphs will provide some insight in concepts of prevention and protection.

Quench Prevention

Since a quench occurs when a magnet is operating above the critical surface, one way to reduce the risk of quenching is to choose an operating current that is located far below the critical surface. This can be done by maintaining a sufficiently large temperature or loadline margin as explained in section 3.2.

A second way of prevention is to limit the heat release inside the coils by avoiding internal movements. The heat capacity (C_p) of a material is a strongly temperature dependent property [16] and is extremely small at temperatures below 10 K. Since superconducting magnets are operated at such low temperatures, tiny movements and other small disturbances of the system can cause relatively large temperature changes leading to transition of the superconducting filaments to the normal state. These changes can be reduced by allowing the displacements, but reducing friction due to movements or by avoiding any displacements by fully connecting the conductors together by means of vacuum impregnation with resins [17]. However it is impossible to rule out the generation of heat completely since for example heat can be released by cracking resins or due to local failure of fully connecting the system.

Another very important factor in quench prevention is the minimum propagation zone (MPZ). This is the minimum length (in 1D) for which a heat disturbance will propagate along a superconducting wire. If the length of a disturbance is smaller than the MPZ, the wire will recover (heat will be conducted to neighbouring parts of the wire) and the disturbance will disappear. Since the thermal conductivity (κ) of a bare superconducting filament such as Nb-Ti at low temperature is very small and the resistivity (ρ) is very large, the MPZ of a single filament is extremely small. This means that it only requires a small amount of energy to reach the critical temperature [17] which causes a transition to the normal state. The length of the MPZ is generally increased by the addition of a normal conducting matrix, usually made of copper, to the superconducting filaments (see section 2.2). In detector magnets also often a stabilizer, such as Aluminium, is added as well. A stabilizer is a material with low resistivity and large thermal conductivity. The percentage of stabilizer available in the conductor volume is indicated by the stabfactor. These additions increase the MPZ by an enormous factor and therefore enlarge the amount of heat that is required to reach the critical temperature. As an example, for a single 0.3 mm bare Nb-Ti filament at $B = 5$ T, $T = 7$ K and $J = 3 \frac{kA}{mm^2}$ the length of the MPZ is 0.3 μm and it requires 1 nJ to reach the critical temperature. This in comparison to the ATLAS Barrel Toroid conductor [15] which has an MPZ of 500 mm shows that it is impossible to operate superconducting magnets without stabilizing materials.

Quench Protection

When a quench does occur there are multiple ways to protect a superconducting magnet from getting damaged. What plays a very important role in this protection is a quench detection system. This system should be able to detect a quench and switch on protection systems within a short period of time. When a quench is detected the power supply of the system is shut down immediately. The remaining current will decrease and the energy stored in the magnetic field will be released. This energy will be absorbed in the form of heat by the conductor windings near the origin of the quench and causes a large and often very local rise in temperature which could damage the system.

Because a temperature rise up to more than about 120 K is not acceptable the system should be designed in such a way that the peak temperature stays below this limit. This can be done by addition of an external dump resistor and quench heaters. This allows part of the released energy to be dissipated in the external resistor and therefore the peak temperature will decrease. Quench heaters are used to spread the heat in a more uniform way over the coils and will therefore also lower the peak temperature.

2.3.4 Forces and Structures

Equation 2.4 illustrates that the magnetic force exerted on a superconducting coil is linearly dependent on the current density and the magnetic field. Since superconducting magnets are usually operated at high current densities and fields, the total force will become significantly large and the system will experience a lot of mechanical stress. To prevent damage and deformation, the system must be supported by a mechanical structure that has to withstand the magnetic forces. During the design of the magnet layout, it is important to take the magnetic forces into account because the magnitude of the forces is directly related to the dimensions of the mechanical structure.

2.3.5 Cryogenics

Since a superconducting magnet can only be operated at very low temperatures a cooling system is needed to keep the coils at the desired temperature. To maintain the low cryogenic temperature of the system a so called cryostat is constructed around the superconducting coils. The most common way of cooling is by a bath of liquid Helium, but for different operating temperatures, different coolants can be used. One of the challenges for the design of a cryostat is to design it in a thermal efficient way [18]. Next to cooling, the cryostat also functions as a mechanical housing. It can for example be used for alignment of the coils and to provide mechanical support. It is favourable to place the mechanical structure inside the cryostat because the amount of material to take the large forces often leads to unacceptable heat inleaks. In addition some material properties improve at low temperatures. The mechanical structure will then be connected to the cryostat in order to transfer the forces. Because a detailed discussion of cryogenics lies beyond the scope of this design study, the subject will not be further addressed in this report¹.

2.4 Magnetic Field Calculation

In this report for all magnetic field calculations, a pre-existing Matlab based design tool named Field [2] is used, which approximates the current distribution of the coils by a cloud of simple straight line-current

¹Interested readers are referred to Flynn [20].

elements. The total magnetic field (at position \vec{r}_2) is obtained by summation over all individual line-current contributions (at positions \vec{r}_1) following from the Biot-Savart Law given by

$$\vec{B}(r_2) = \int \frac{\mu_0 I d\vec{l} \times \vec{r}}{4\pi |\vec{r}|^3}, \quad (2.5)$$

where $\vec{B}(r_2)$ is the magnetic field at the target point r_2 , I is the current, $d\vec{l}$ is a vector whose magnitude is the length of the differential element of the wire, and whose direction is the direction of conventional current, μ_0 is the magnetic permeability of vacuum and $\vec{r} = \vec{r}_2 - \vec{r}_1$ is the displacement vector from the source element to the target point at which the field is being computed.

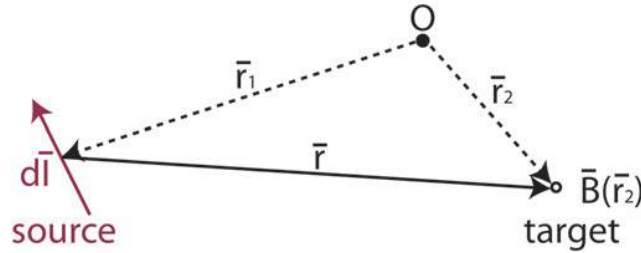


Figure 2.4: Explanation of the variables used for the calculation of the magnetic field with the Biot-Savart law. Reprinted from van Nugteren. [2]

To speed up the calculations Field employs a Multilevel Fast Multipole Method [19], which reduces the computational complexity from $O(N \cdot M)$ to $O(N + M)$, where N is the number of source elements and M the number of target points. This in combination with the text based interface makes Field very suitable for parametric optimization studies.

3 Numerical Method

This chapter describes the numerical method that is used for the optimization study of the superconducting magnet system of the LAr neutrino detector. First an overview of the geometry of the magnet system and the corresponding parameters is presented. Second, an explanation of the current density calculation method is provided, followed by a detailed description of the optimization algorithm. The optimization study is performed by making use of the text based interface of Field and exists of a single optimization cycle accompanied by a parametric sweep. It is the aim of the optimization to find a set of geometrical parameters that satisfies the magnetic field requirements.

3.1 Geometry Definition

In the design study of the neutrino detector magnet a lot of different parameters are used to define the geometry of the magnet and the shape and magnitude of the magnetic field. This section explains the meaning of these parameters and their relation to the overall design. First the geometrical parameters will be explained by means of a side and a topview of the detector magnet. Second, the field parameters will be explained by means of a 3D view of the detector magnet.

3.1.1 Geometrical Parameters

Figure 3.1 presents an overview of the geometry of the magnet system and the parameters used to describe its different parts. The sideview (figure 3.1(a)) indicates hcoil and dcoil, which represent the height and width of the coil respectively. The vertical distance between the coils is represented by hsplit and the length of the coil in the y-direction by L2. The topview (figure 3.1(b)) indicates R, which is the inner radius of the corner, and L1 and L2 which represent the length of the coil in the x- and y-directions respectively. For both views the relevant coordinate system is displayed in the lower left corner.

3.1.2 Field Parameters

Figure 3.2 presents the volume of the neutrino detector by the blue box that is located in between the two superconducting magnets, which are depicted in gray. The points that are used to define the size and shape of the magnetic field inside the detector magnet are presented by the red dots. Bcen is located at the center of the detector volume, its position relative to the coordinate system is (0,0,0). Bedge1 and Bedge2 provide the magnetic fields at the center of the short and long edge of the detector volume. Their relative coordinates are (-6,0,0) and (0,-4.5,0).

3.2 Current Density Calculation Method

As discussed in section 2.1 the current density, magnetic peak field and temperature are limiting factors on the existence of the superconducting state. In order to operate a superconducting magnet the superconducting state has to be maintained and a decent combination of the limiting factors has to be applied to the system.

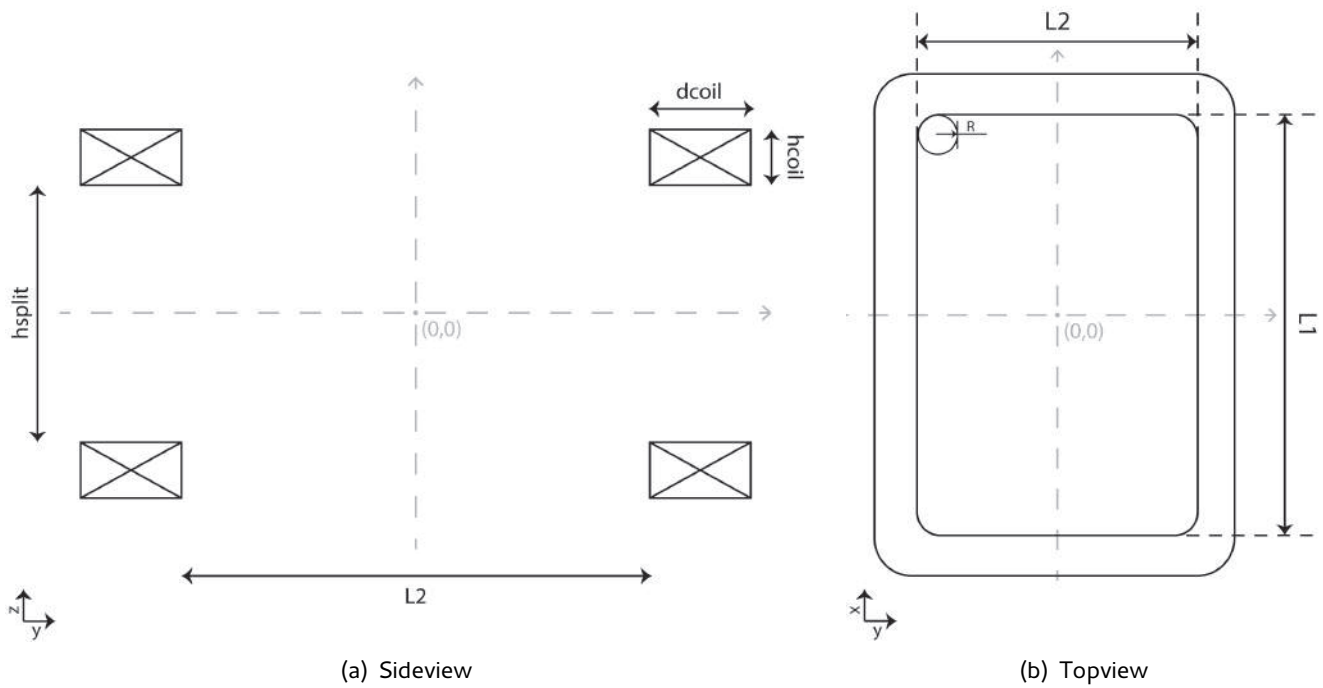


Figure 3.1: Explanation of the geometry and the parameters used in the optimization study of the detector magnet. Note that the parameter 'hsplit' is not relevant for the solenoid system (chapter 5) since it exists of only one coil. For the double racetrack system (chapter 4) it is possible to split the coils horizontally and separate them by a vertical distance 'hdeck'.

The operating temperature is mainly determined by the type of cryogen that is used to cool the magnet below the critical temperature. For Niobium Titanium the best way to cool the magnet is to use liquid Helium at its boiling point of 4.2 K. Because the system will be cooled by a pressurized Helium loop, this boiling point is elevated slightly to 4.5 K, determining the operating temperature of the magnet. The advantage of Magnesium di-boride however is that the cooling costs of the system can be kept low by operating at a higher temperature of approximately 20 K. Such a system would be cooled by Helium gas.

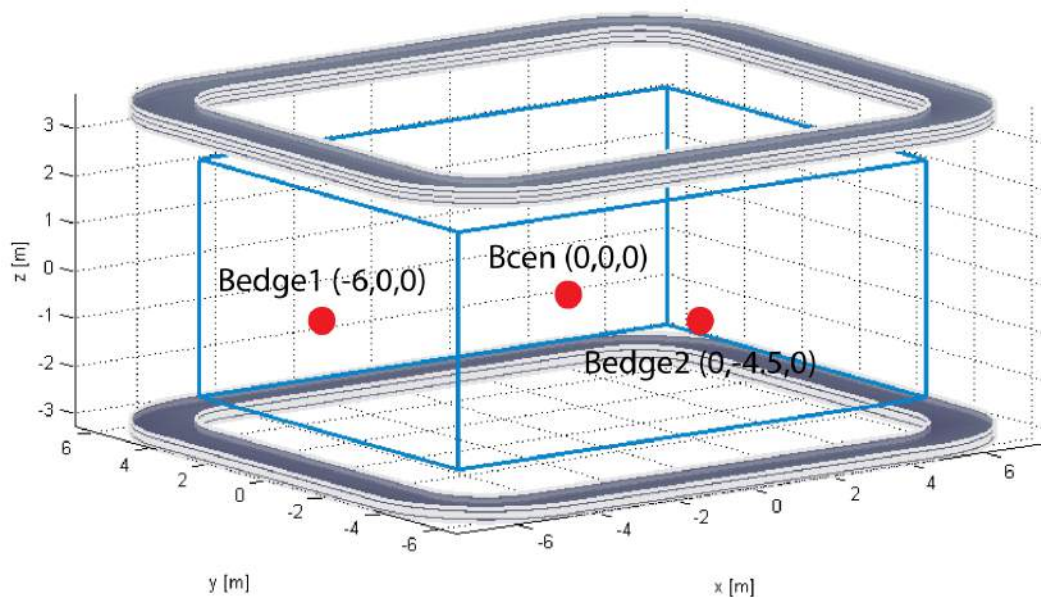


Figure 3.2: Coordinates of the points used in the optimization study of the detector magnet to define the size and shape of the magnetic field.

To calculate the current density at a certain operating temperature a so called loadline fit is performed on the corresponding critical surface slice. First the magnetic peak field is calculated for an arbitrary current density. By making use of the linear relation between the magnetic peak field and the current density, following from Biot-Savart (equation 2.5), a loadline can be drawn by extrapolation of the calculated point through the origin. The intersection of the loadline with the critical surface provides the upper limit for the current density. Superconductivity can only be maintained when the operating current is equal or lower to this upper limit. Beyond this point it is certain the magnet will quench (see section 2.3.3). For safety reasons it is common to include a margin while determining the operating current density. There are two ways to implement a safety margin to the current density calculation (see figure 3.3). The first option is to set a temperature margin. This temperature margin is added to the set operating temperature and therefore changes the critical surface slice that is used for the calculation of the intersection point with the loadline. By adding the temperature margin, the upper limit for the current density is lowered. The second option is to set a loadline margin. This margin is represented by a percentage that is taken on the loadline in order to determine the operating current density. By applying this percentage, the operating point on the loadline will be chosen at a sufficient distance from the critical surface. Commonly only a percentage on the loadline to determine a safe operating current density is applied.

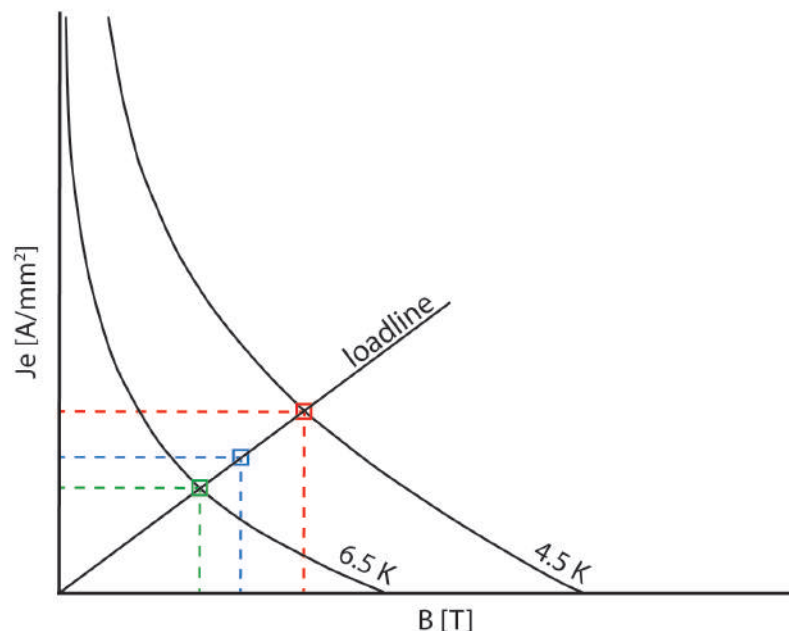


Figure 3.3: Loadline fit performed on a critical surface slice for an operating temperature of 4.5 K. The red square represents the upper limit for the operating point, the blue square represents the operating point after application of a loadline margin and the green square represents the operating point after addition of a 2 K temperature margin to the operating temperature of 4.5 K.

3.3 Optimization Algorithm

As introduced in section 2.4, Field provides the basis for the magnetic field calculations. By making use of the text based interface, optimization studies can be performed. This section introduces the numerical method used for the optimization study executed in this report.

3.3.1 Targets and Variables

In order to satisfy a set of requirements, for example the magnitude of the magnetic field at the center of the detector volume, the parameters describing the geometry can be set as optimization variables.

The requirements can then be seen as the targets that have to be achieved. The optimization of such a system can be compared to solving a system of non-linear equations. To ensure that there exists only one solution, the number of variables has to be equal to the number of equations. This also applies to the optimization problem. In order to optimize a system with N variables, N so called targets are required. During the optimization, the solver linearises the system of equations at a pre-set start point, after which the solution of the linear system becomes the new start point. After multiple iterations, the system converges to a final solution. The optimization study described in this report was implemented in MATLAB and the function `fsolve` was chosen to perform the optimization. `Fsolve` solves a system of non-linear equations in the form of $f(x) = 0$. The Levenberg-Marquadt algorithm[21][22] was selected to perform the calculations. When performing an optimization study, it is important to keep in mind that the optimal set of variables does not always exist within the given bounds. For instance, this could happen when different targets are competing. Therefore it is very important to think through the choices of targets and variables before running an optimization.

3.3.2 Parameter Sweep

Next to the parameters that are used as a variable for the achievement of a target, a system usually contains other parameters. These remaining parameters can be included in the optimization study in two ways. The first option is to link them to new targets and to run a second optimization around the first one. During this double optimization, the variables in the inner (first) optimization are used to meet specific magnetic field requirements and the variables in the outer (second) optimization are used to obtain a global objective such as the minimization of the conductor volume. This however, is a time consuming process. The variables that are altered in the outer optimization affect the values of the targets of the inner optimization and the other way around. Therefore a lot of optimization cycles have to be run before both the inner and the outer optimization reach the optimal configuration of variables for the system. The second option is to perform a parametric sweep on the remaining parameters. The value of each parameter is varied over a certain range and for every combination a single optimization is performed. The result is an optimal configuration for each combination of remaining parameters. Based on experience, the second option proves to be much more valuable because it provides insight on the influence of the remaining parameters on the system properties, whereas the first option only gives a single optimal configuration for the system. Therefore the optimization towards the magnetic field requirements accompanied by a parameter sweep is chosen as method for this design study.

3.3.3 Optimization Cycle

The optimization process can be represented by a cycle that consists of four parts of different operations (see figure 3.4). In the first part the system variables are set by `fsolve`. In the second part the system geometry is created based on the input variables, the peak field is calculated and a loadline fit is performed to set the operating current (J_{op}). The third part calculates the values of the selected targets, in this case the field parameters. Furthermore, the deviation from the required values is determined and returned to `fsolve`. In the fourth part `fsolve` tries to minimize the deviations by changing the variables corresponding to the targets in a 'clever' way. The changed variables are then sent to the first part and the optimization cycle repeats. The process goes on until `fsolve` finds a set of variables that sets all deviations below a pre-defined tolerance threshold. This final set of variables corresponds to a geometry that satisfies the demanded field requirements, while taking the imposed safety margins into account.

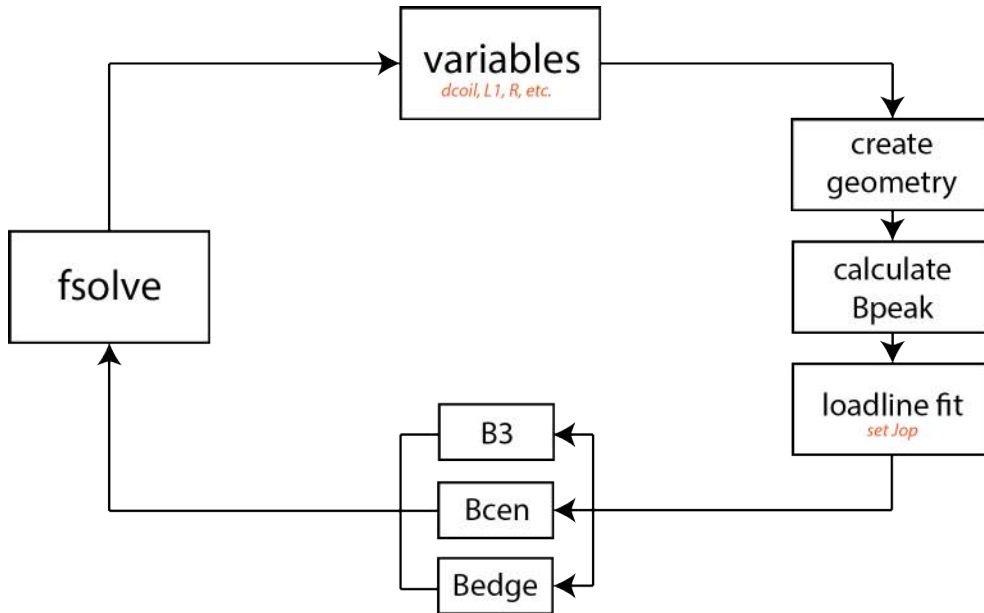


Figure 3.4: Schematic representation of the optimization process used to meet the field requirements.

3.4 Conclusion

In this section, a numerical method has been developed for the optimization of the superconducting magnet system. The optimization study will be performed by making use of the text based interface of Field.

4 Double Racetrack Layout Optimization

This chapter presents the layout optimization performed for the double racetrack configuration. First, the conductor settings are described followed by an overview of the design choices made concerning the geometrical design of the double racetrack system. For the optimization of the double racetrack system two different parametric studies are performed. The aim of both sweeps is to obtain insight in the relation between the geometrical parameters and the properties of the magnetic field. The result of the layout study is a set of optimized models for the double racetrack system. To be able to continue the preliminary design study, a so-called working model is selected. Further analysis is performed with respect to this model.

4.1 Conductor Settings

Since the optimization performed in this report is part of a preliminary design study, the geometrical and electrical properties of the conductor are not well defined. The conductor used for the ATLAS barrel toroid [15] has been successfully implemented and adheres similar requirements for the magnetic field as the neutrino detector. Therefore its properties are used as a first approximation for the optimization study of the racetrack magnet system. The conductor settings used for the layout optimization of the racetrack are listed in table 4.1, 4.2 and 4.3.

Table 4.1: Type and operating parameters of the conductor used for the layout optimization of the double racetrack configuration.

Type	Nb-Ti
Operating Temperature	4.5 K
Temperature margin	0 K
I/Ic along the loadline	65 %

Table 4.2: Geometric parameters of the ATLAS barrel toroid conductor which are assumed as a first approximation for the superconducting magnet system of the LAr neutrino detector.

Dimensions	bare	57.0 * 12.0	mm
	insulated	57.8 * 12.8	mm
	corner radius	57.0 * 12.0	mm
Total cross-section	bare	684	mm ²
	insulated	737	mm ²
Aluminium area		632	mm ²
Metal area		42.5	mm ²

Table 4.3: Cable parameters of the ATLAS barrel toroid conductor which is assumed as a first approximation for the superconducting magnet system of the LAr neutrino detector.

Dimensions	22.0 * 2.3 mm
Number of strands	32
Strand diameter	1.30 mm
Filament diameter	0.050 mm
Twist pitch	50 mm
Transposition pitch	140 mm
Cu/Sc ratio	1.30
Section of Nb-Ti	18.5 mm ²
Section of Cu	24.0 mm ²

4.2 Design Choices

Before performing the optimization a few choices are made concerning the geometrical design of the double racetrack system. These design choices are based on experiences acquired in an earlier stage of the design study and are applied by setting the corresponding parameters to a fixed value. This section explains the reasoning behind these choices. The fixed values for the corresponding parameters are summarized in table 4.4.

Vertical coil height – hcoil Previous optimization steps revealed that there exists no optimal value for the vertical height of the coils. To reach an optimized system with respect to the field requirements, the coil height tends to converge to zero in order to minimize the applied volume of conductor material. Since the size and shape of the conductor put a lower limit on the height of the coils, the value of hcoil is set at the height of a single double pancake coil. This means that the value of hcoil is determined by the combination of the height of two pancakes of the chosen conductor with an insulation layer in between. The short side of the windings is placed along the vertical z-axis.

Two double pancake decks – hdeck Preceding optimization steps showed that to reach the required magnetic field of 1 T in the center of the detector volume, the horizontal coil width (dcoil) had to take up values in the range of 1.00 m to 2.00 m, which is relatively large. Although manufacturing coils of large width is not impossible, it is more favourable to avoid them in order to reduce the total size of the system and to simplify coil production. Additionally the accumulation of forces over the width of the coil reduces, resulting in lower peak pressures. To be able to reduce the horizontal coil width and still meet the magnetic field requirements, the single double pancake coil is replaced by two double pancake coils separated by a fixed distance, hdeck. This ‘double double pancake’ coil configuration is similar to the coil construction of the ATLAS barrel toroid system [15]. The vertical distance between the two double pancake decks of the ATLAS barrel toroid is used for the optimization study performed in this section.

Coil corner radius – R The coil corner radius determines the value of the magnetic peak field (at the surface of the racetrack coils) and therefore influences the total required volume of conductor material. Previous optimization steps indicated that to reduce the conductor volume, the coil corner radius had to become very large¹. Because a large radius increases the size of the total magnet system a suitable value has to be chosen. For the parametric study of L1 and L2 (section 4.3.1) the radius is set at a fixed value of 1.50 m.

¹To minimize the magnetic peak field and therefore the necessary conductor volume, the coil corner radius has to become as large as L1/2. For this radius, the coil becomes a circle, which is the configuration with the lowest possible peak field.

Coil lengths – L1 and L2 Since placement of the magnet system within the detector volume is not an option, the values for the coil lengths (L1 and L2) can not become smaller than the size of the liquid Argon vessel (see section 1.3).

Table 4.4: Summary of the design choices made for the double racetrack configuration, the corresponding parameters and their values.

Parameter	Value	Description
hcoil	118.1 mm	Vertical coil height
hdeck	50 mm	Vertical spacing between two double pancake decks
R*	1.50 m	Coil corner radius

* The value of the coil corner radius is only set to a fixed value for the parametric sweep over L1 and L2 (section 4.3.1).

4.3 Parametric Study

As described in section 3.3.2 the optimization study performed in this report is based on the combination of a single optimization cycle accompanied by a parameter sweep. The parameters are varied over a fixed range of values and for each different combination of parameters the optimizer (section 2.4) attempts to find the optimal design with respect to the set targets. For the double racetrack system two different parametric studies are performed. First, the systems with different values for the inner lengths of the coils (L1 and L2) are optimized. Second, a parametric sweep is performed over the coil radius (R) and the required field at the edge of the detector (Bedgereq). Since both parametric studies have to satisfy the same central field requirement, one could say that the results of both studies are actually the same. This is in fact true, but by looking at the optimization in two ways, different relations between parameters are discovered and different approaches of determining the most suitable model can be applied. If for instance the length of the coils is the limiting factor for the magnet design, the results of the sweep over L1 and L2 should be used to determine an appropriate model. If the field requirement on the edge of the detector is a limiting factor, the results of the sweep over R and Bedgereq should be used to find a suitable model. The results of both parametric studies and an overview of the applied optimization settings are presented in the subsections below.

4.3.1 L1 and L2

For the parametric study of the inner lengths of the coils the values of both L1 and L2 are swept over a specific range. L1 is varied from 11.00 m to 15.00 m with increments of 1.00 m and L2 is varied from 8.00 m to 13.00 m with increments of 0.50 m. The targets and corresponding variables that are used to perform the optimization for each different combination of L1 and L2 are presented in table 4.5.

The aim of this sweep is to obtain knowledge about the relationship between the length of the coil and the magnetic field at the edges of the detector while the value of the magnetic field at the center is kept at a fixed value of 1 T.

Figure 4.1 and 4.2 illustrate the influence of L1 and L2 on the magnetic field at Bedge1. It can be seen from both figures that the magnitude of the magnetic field at Bedge1 increases for larger values of L1. This can be explained by the fact that by enlarging the coil length, the zone in between the two racetrack coils, where the magnetic fields of both coils cancel each other, is positioned farther away from the

Table 4.5: Explanation of the targets and variables used for the optimization accompanying the parametric study of L1 and L2

Target	Variable	Description
$B_{cen} = 1 \text{ T}$	dcoil	By varying the coil width for a fixed coil height the conductor volume will be varied. Since the current density is fixed by the loadline fit, the total current is linearly related to the conductor volume. Therefore variation of the conductor volume will influence the magnetic field magnitude at the center of the detector.
$B_3 = 0 \text{ T}$	hsplit	Homogeneity of the magnetic field inside the detector can be achieved by forcing all the higher harmonics of the magnetic field to be zero (for a detailed explanation of field harmonics see appendix A). The remaining first harmonic, the dipole field, will establish the required uniform field. Since the contribution of higher harmonics reduces exponentially it is sufficient to set the first non-zero harmonic after the dipole to zero. Therefore B3 is set to be zero in order to obtain a homogeneous field. Since the value of B3 is determined by the geometry of the magnet system, the target is coupled to the vertical distance between the two racetrack sets.

detector volume. Therefore, the magnitude of the field at the edge of the detector volume becomes larger. Figure 4.1 shows that the relation between the magnetic field at Bedge1 and L2 changes after L1 becomes larger than 12 m, which is the size of the long side of the detector volume. This change is caused by the fact that for values of L1 smaller than the long side of the detector volume, the magnitude of the magnetic field at Bedge1 is mainly determined by the coil length L2. For values of L1 larger than the long side of the detector volume, the magnitude of the magnetic field at Bedge1 is mainly determined by L1. Large values of L2 lead to an increase of the magnetic peak field and therefore to a decrease of the operating current density (for an explanation see section 4.3.2). Therefore, the magnitude of the magnetic field at Bedge1 is smaller for larger values of L2 (in combination with a value of L1 which is equal or larger than the long side of the detector). This relation can also be recognized in figure 4.2. For small values of L1, an increase in the value of L2 leads to a slightly larger magnetic field at Bedge1. For values of L1 larger than 12 m, an increase in the value of L2 leads to a smaller magnetic field at Bedge1. The figure also illustrates that for very large values of L2, the magnitude of the magnetic field at Bedge1 becomes independent of L2.

The relation between the magnitude of the magnetic field at Bedge2 and the length of the coils is presented by figure 4.3 and 4.4. Both figures clearly illustrate that the magnitude of the magnetic field at Bedge2 becomes larger for increasing values of L2. This relation is very similar to the relation between Bedge1 and L1 (figure 4.1) and also originates from the fact that the magnetic field at the edge of the detector volume becomes larger when it is positioned farther away from the cancellation zone between the two coils. Interesting though is that both graphs illustrate that the magnitude of the magnetic field at Bedge2 is independent of the value of L1. A similar relation holds for Bedge2 and L1. Due to this decoupling the double racetrack system can be seen as a combination of two independent two-dimensional planes.

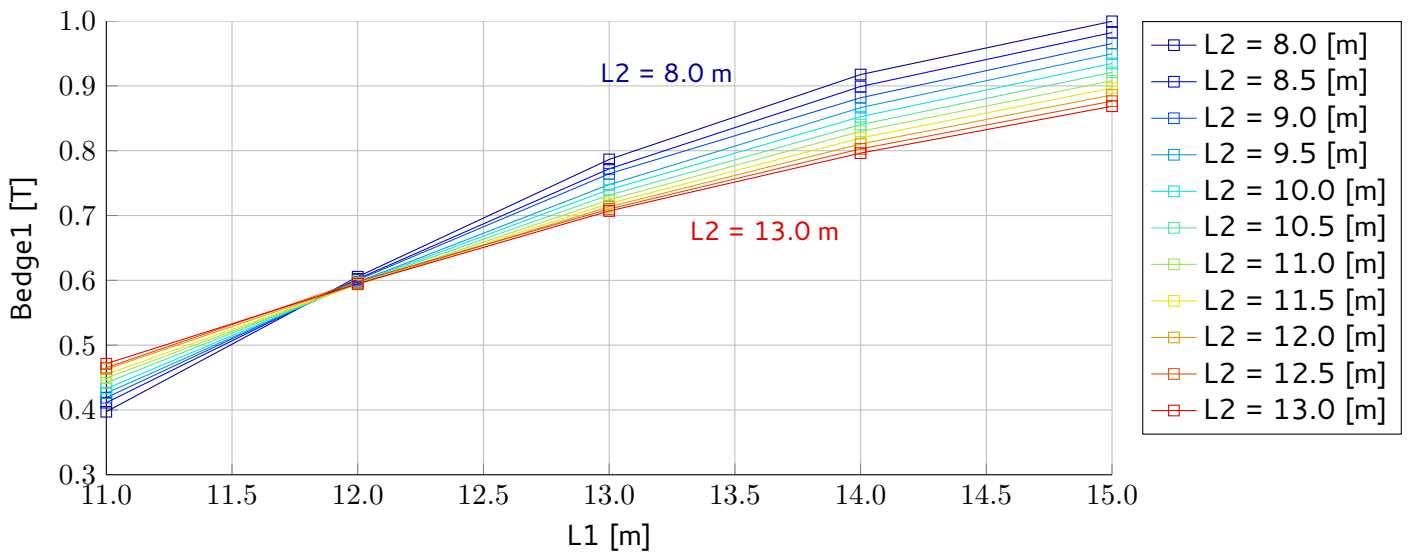


Figure 4.1: Magnitude of the magnetic field at Bedge1 as a function of L1 for various values of L2. Note that the way in which L2 influences the magnetic field at Bedge1 changes at the intersection at L1 = 12m.

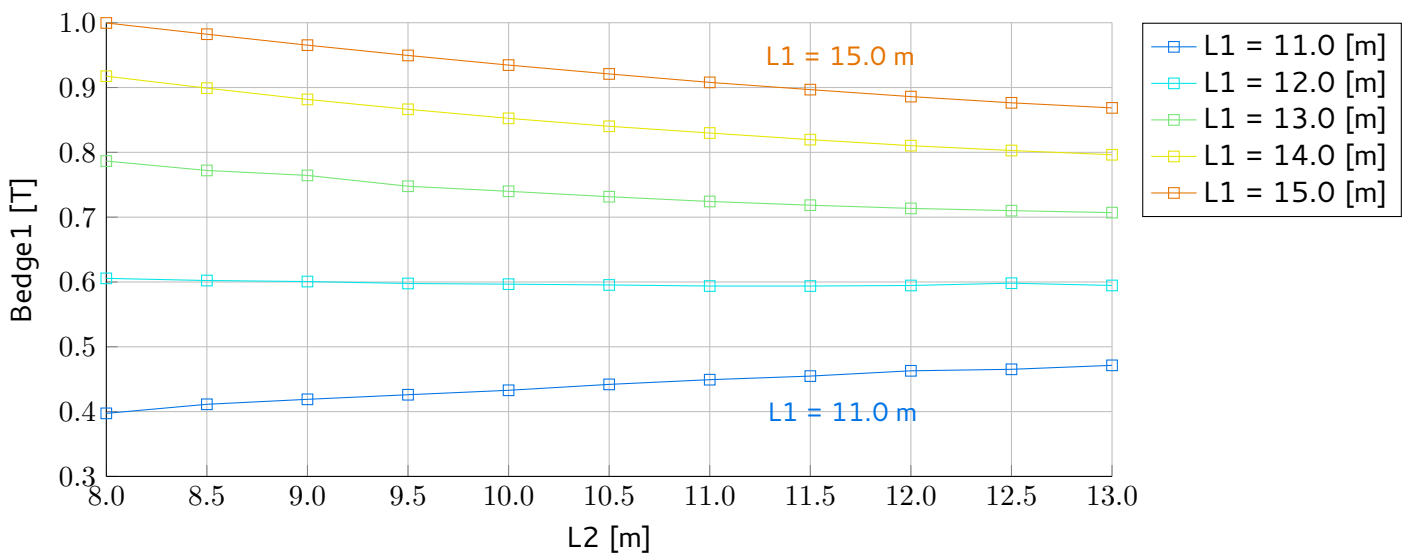


Figure 4.2: Magnitude of the magnetic field at Bedge1 as a function of L2 for various values of L1. Note that for large values of L2, the magnitude of Bedge1 only depends on the value of L1.

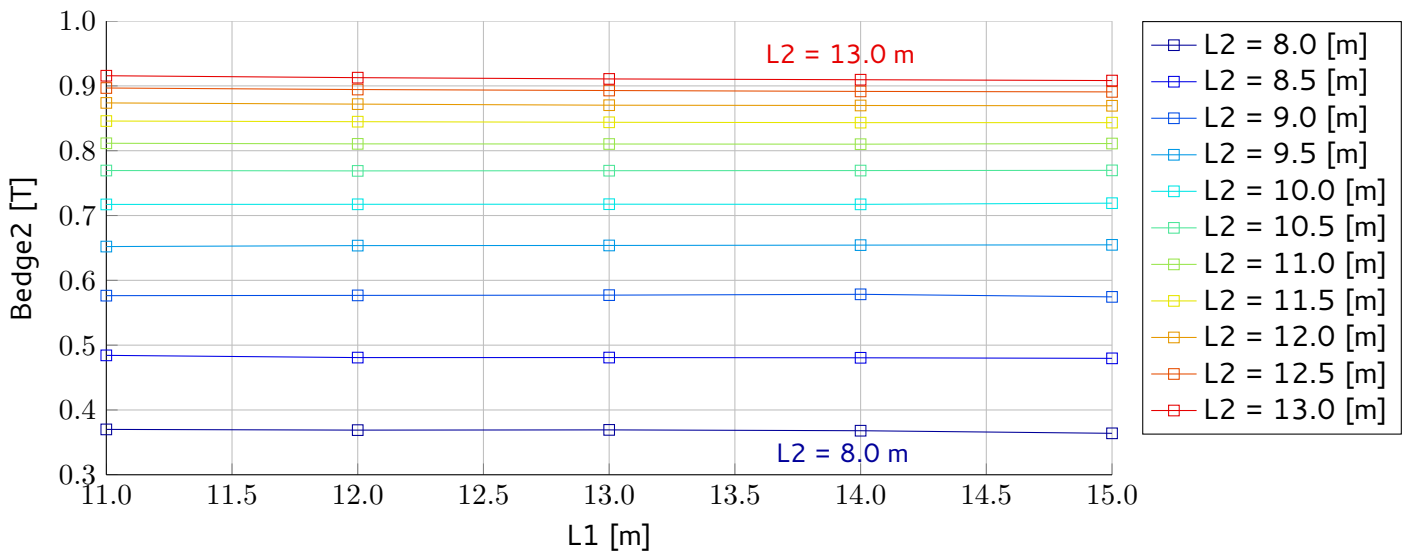


Figure 4.3: Magnitude of the magnetic field at Bedge2 as a function of L1 for various values of L2. Note that the magnitude of the magnetic field at Bedge2 is independent of the value of L1.

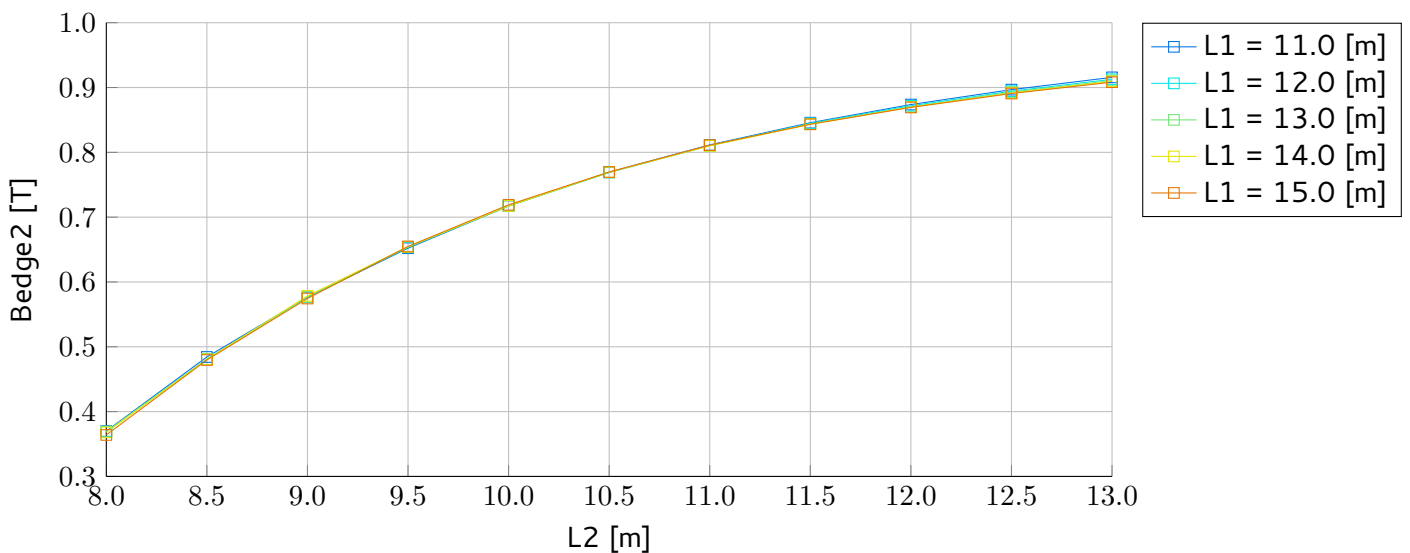


Figure 4.4: Magnitude of the magnetic field at Bedge2 as a function of L2 for various values of L1. Note that the magnitude of the magnetic field at Bedge2 is independent of the value of L1.

4.3.2 R and Bedgereq

For the parametric study of the coil radius and the required value of the magnetic field at the edges of the detector volume the values of both R and Bedgereq are swept over a specific range. R is varied from 1.00 m to 2.00 m with increments of 0.50 m and Bedgereq is varied from 0.500 T to 0.900 T with increments of 0.025 T. The targets and corresponding variables that are used to perform the optimization for each different combination of R and Bedgereq are presented in table 4.6.

Table 4.6: Explanation of the targets and variables used in/for the parametric study of R and Bedgereq

Target	Variable	Description
Bcen = 1 T	dcoil	By varying the coil width for a fixed coil height the conductor volume will be varied. Since the current density is fixed by the loadline fit, the total current is linearly related to the conductor volume. Therefore variation of the conductor volume will influence the magnetic field magnitude at the center of the detector.
B3 = 0 T	hsplit	Homogeneity of the magnetic field inside the detector can be achieved by forcing all the higher harmonics of the magnetic field to be zero (for a detailed explanation of field harmonics see appendix A). The remaining first harmonic, the dipole field, will establish the required uniform field. Since the contribution of higher harmonics reduces exponentially it is sufficient to set the first non-zero harmonic after the dipole to zero. Therefore B3 is set to be zero in order to obtain a homogeneous field. Since the value of B3 is determined by the geometry of the magnet system, the target is coupled to the vertical distance between the two racetrack sets.
Bedge1	L1	In between the two racetrack coils there exists a zone where the magnetic fields of both coils cancel each other. The distance between this zone and the edge of the detector volume is related to the magnitude of the magnetic field at the edge of the detector volume. By changing the length of the coil in the x-direction (L1), the distance between the short edge of the detector volume and the cancellation zone is varied. Therefore variation of L1 will influence the magnitude of the magnetic field at Bedge1.
Bedge2	L2	In between the two racetrack coils there exists a zone where the magnetic fields of both coils cancel each other. The distance between this zone and the edge of the detector volume is related to the magnitude of the magnetic field at the edge of the detector volume. By changing the length of the coil in the y-direction (L2), the distance between the long edge of the detector volume and the cancellation zone is varied. Therefore variation of L2 will influence the magnitude of the magnetic field at Bedge2.

The result of the combination of the parametric sweep and optimization is a list of 85 optimized models that all satisfy the imposed magnetic field requirements. The geometric design, field specifications and other important system properties are summarized in appendix B.1.

Figure 4.5 and figure 4.6 present the conductor volume as a function of the coil corner radius for various values of the required magnetic field at the edges of the detector volume and vice versa. It can be seen that for all Bedgereq values, the conductor volume becomes smaller for increasing values of the radius. Since a larger radius reduces the magnetic peak field (see 4.7), less conductor is needed to meet the field requirements. The larger vertical shift in conductor volume for large values of Bedgereq in figure 4.7 can be explained by the non-linear relation between the conductor volume and the value of Bedgereq which is illustrated by figure 4.8. This non-linear relation originates from the fact that the value of the magnetic field at the edge of the conductor volume does not vary linearly with the length of the coils, as can be

seen in figure 4.1 and figure 4.4. Since relatively large coils are needed to produce a large magnetic field at the edge of the detector volume, a larger volume of conductor material is necessary to create these fields.

The relation between the magnetic peak field (B_{peak}), the coil corner radius (R) and the required magnetic field at the edges of the detector volume ($B_{edgereq}$) is illustrated by figure 4.7 and 4.8. Both figures show that for all values of $B_{edgereq}$, the magnitude of magnetic peak field becomes smaller for increasing values of the radius. This can be explained by the fact that in the corners where the short and long sides of the racetrack meet, both coils contribute to the overall magnetic field, which therefore becomes higher. By adding a radius between the coils, the distance between the two meeting sides becomes larger, their contributions to the overall magnetic field in the corner drop and therefore the magnetic peak field becomes smaller. Figure 4.7 clearly shows that the effect of the radius increase on the magnitude of the magnetic peak field becomes smaller for larger values of R . Both figures also show that for all values of R , the magnitude of the magnetic peak field becomes larger for increasing values of $B_{edgereq}$. In order to produce a larger magnetic field at the edges of the detector, the coils have to be placed at a larger distance from the detector volume (see table 4.6). When $L1$ and $L2$ are increased, the operating current density needed to create the required magnetic field of 1 T in the center of the detector goes up. Therefore, the contributions to the magnetic field in the corners of the coils increase and the magnetic peak field becomes larger.

Figure 4.9 and figure 4.10 present the relation between the operating current density (J_{op}), the coil corner radius (R) and the required magnetic field at the edges of the detector volume ($B_{edgereq}$). Both graphs illustrate that the operating current density becomes larger for increasing values of the radius and that it becomes smaller for increasing values of $B_{edgereq}$. As explained in section 2.1, the operating current density is fixed by the value of the magnetic peak field. Parameters that influence the magnitude of the magnetic peak field will therefore also affect the value of the operating current density. An increasing corner radius results in a smaller magnetic peak field and therefore a larger operating current density. An increasing required value for the magnetic field at the edge of the detector volume causes the magnetic peak field to become larger and therefore the operating current density decreases.

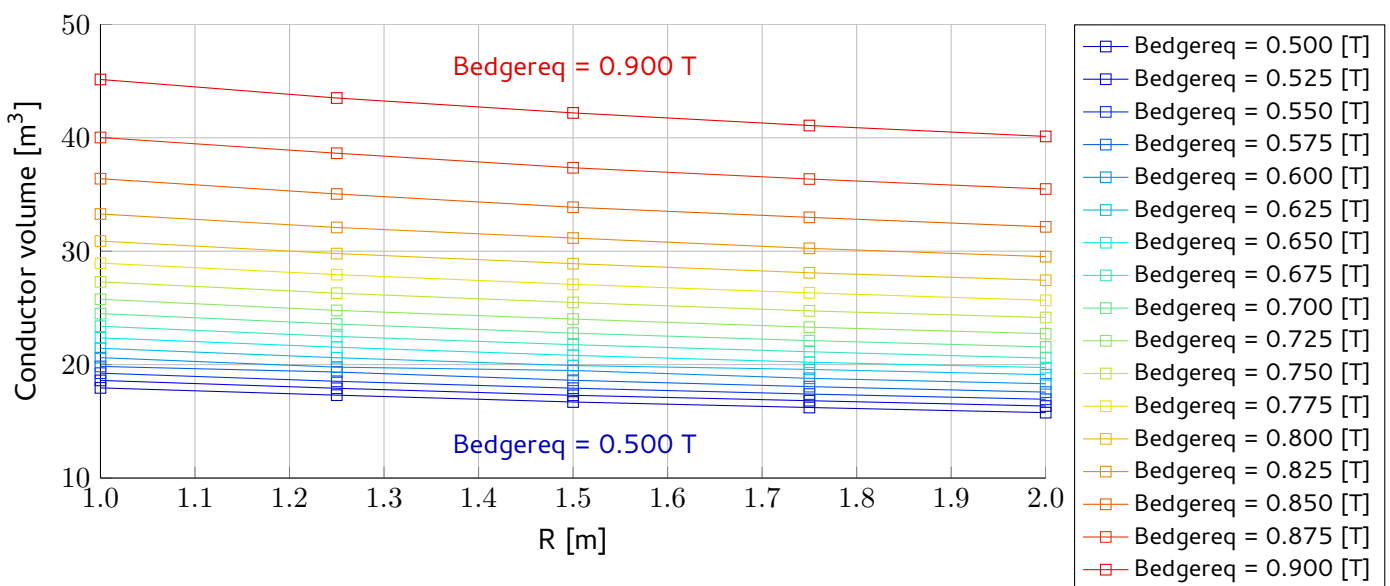


Figure 4.5: Conductor volume (V_c) as a function of the coil corner radius (R) for various values of the required magnetic field at the edges of the detector volume ($B_{edgereq}$).

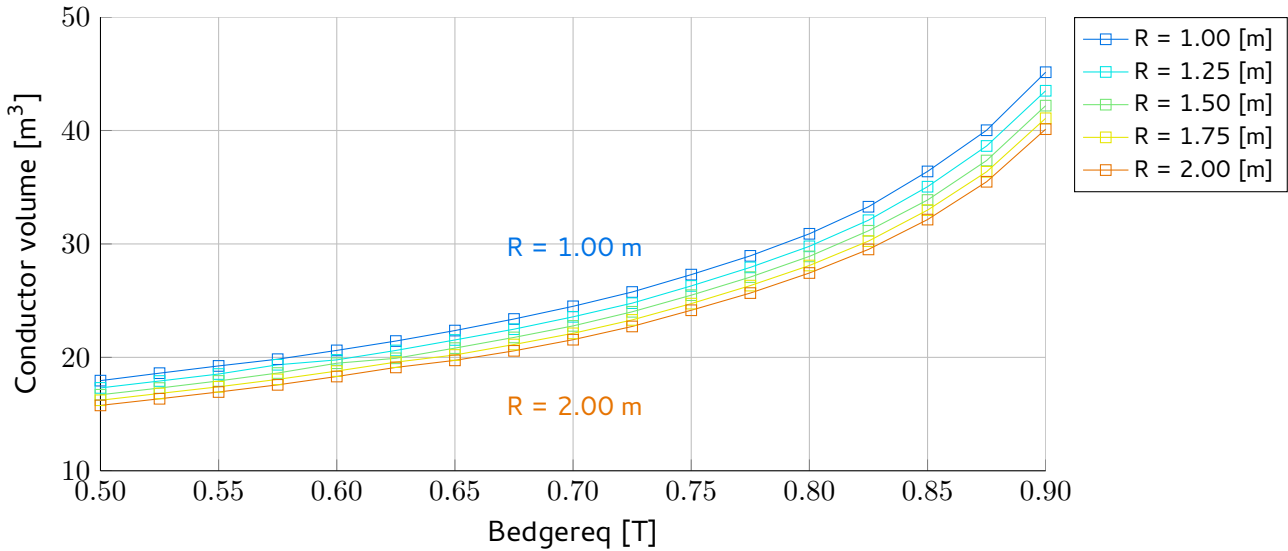


Figure 4.6: Conductor volume (V_c) as a function of the required magnetic field at the edges of the detector volume ($B_{edgereq}$) for various values of the coil corner radius (R).

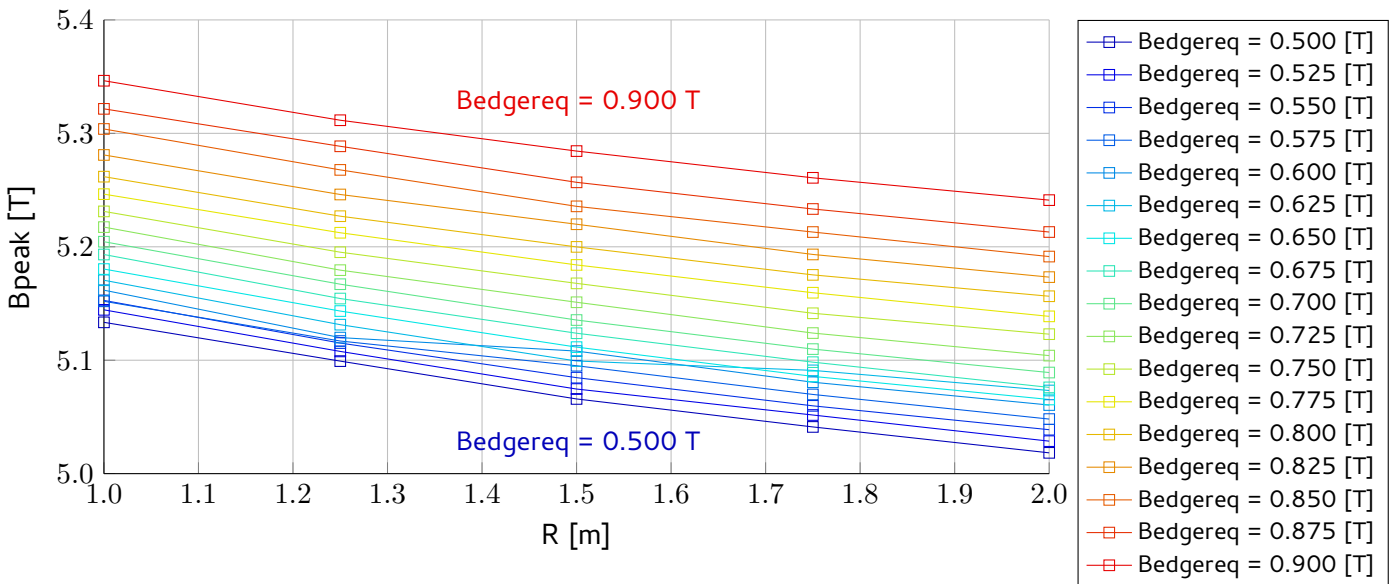


Figure 4.7: Magnetic peak field (B_{peak}) as a function of the coil corner radius (R) for various values of the required magnetic field at the edges of the detector volume ($B_{edgereq}$).

4.3.3 General results

At the beginning of this section, a remark was made about the fact that the results of both parametric studies are similar. As an addition to the specific results for each sweep presented in the preceding subsections, this section will give an overview of the general relations observed for the double racetrack system.

From the data tables in appendix B.1 and B.2 it can be deduced that for large values of the coil lengths (L_1 and L_2) the vertical distance between the coils ($hsplit$) increases. This relation originates from the fact that for both parametric studies $hsplit$ is chosen as the variable that has to maintain a homogeneous magnetic field in the center of the detector volume. Or in other words, has to set the third harmonic field (B_3) to zero (see table 4.5 and 4.6). The value of B_3 depends on the geometry of the coils and optimal homogeneity is achieved by placing the center of mass of the coils at a certain angle with respect to the x-

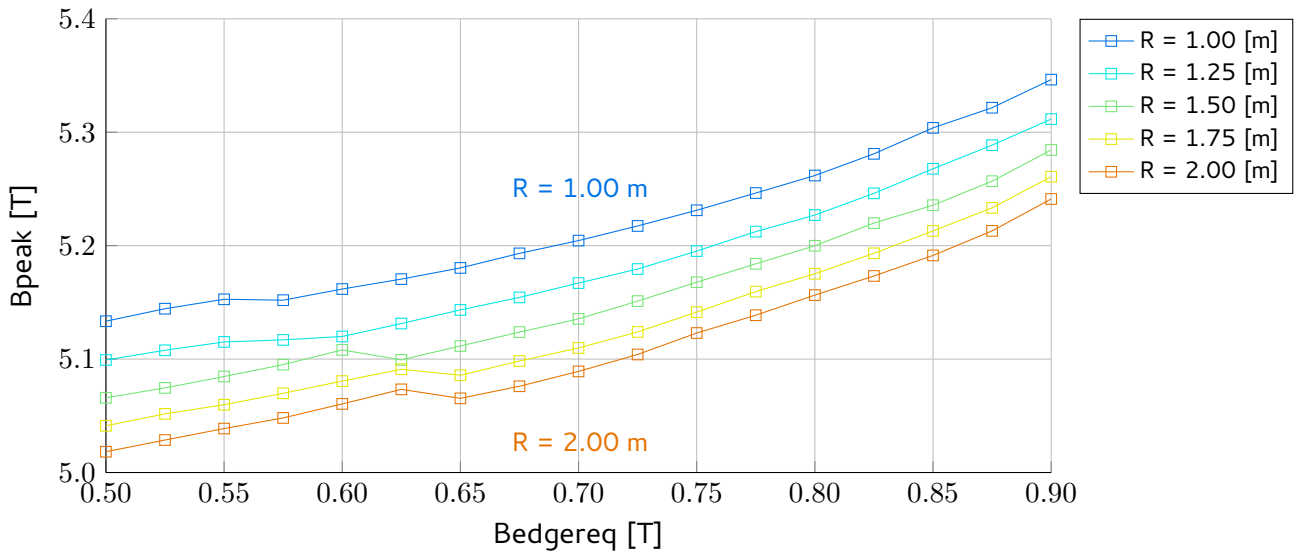


Figure 4.8: Magnetic peak field (B_{peak}) as a function of the required magnetic field at the edges of the detector volume ($B_{edgereq}$) for various values of the coil corner radius (R). The curve deviations are artefacts of the MLFMM algorithm used in this optimization study.

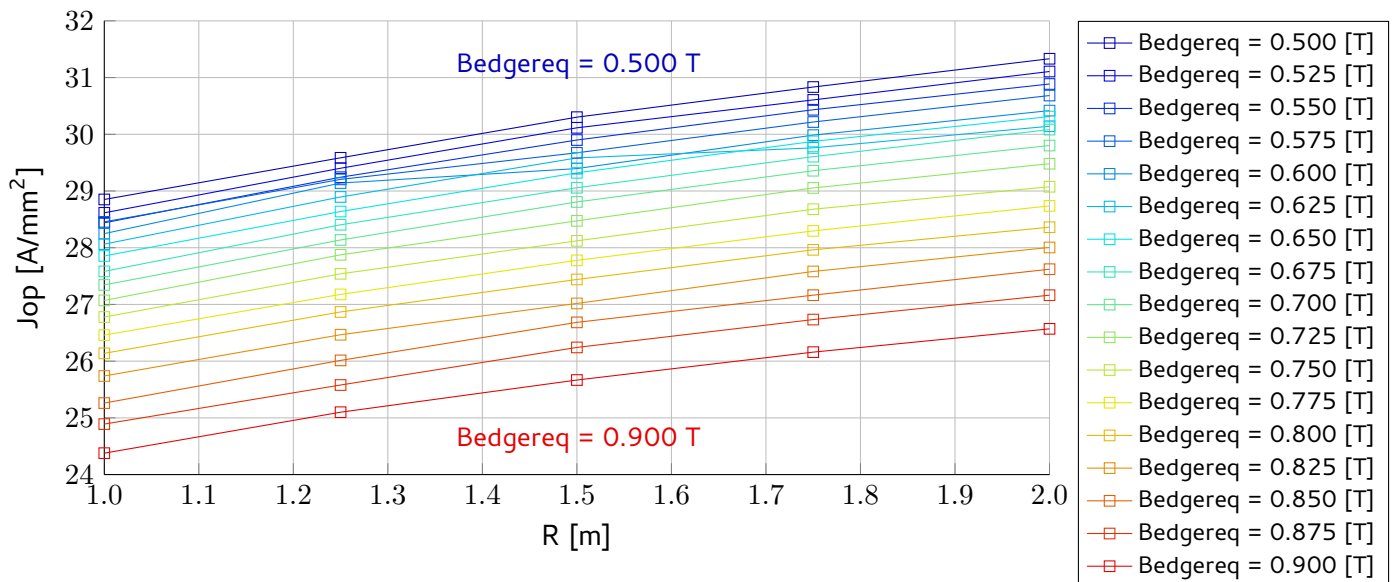


Figure 4.9: Operating current (J_{op}) as a function of the coil corner radius (R) for various values of the required magnetic field at the edges of the detector volume ($B_{edgereq}$).

and y-axis. When L1 and L2 become larger, this angle changes and B3 will no longer be zero.² In order to establish the same optimal angle between the coils and the axes, hsplit should be increased.

Furthermore, the data tables show that the horizontal width of the coils (dcoil) becomes larger for increasing coil lengths (L1 and L2). Due to the increasing distance between the coils and the detector a larger current is necessary to meet the magnetic field requirements at the center of the detector volume. Since the current density is limited by the critical surface (section 2.1), the only way to achieve the required magnetic field is to increase the conductor volume. Since the vertical coil height is fixed (section 4.2), the conductor volume can only be increased by increasing the horizontal width of the coils. Therefore, larger coil lengths lead to an increasing coil width and a larger conductor volume.

4.4 Working Model and Analysis

The parametric study presented in section 4.3 resulted in a list of optimized models for the double racetrack system. The choice for an optimal design has to be based on the final requirements for the neutrino detector magnet, which are at present not fully defined. Therefore an additional iteration with the people designing the detector itself is necessary. The results presented in this report serve as a basis for such an iteration and form a starting point for future design studies.

To be able to continue the preliminary design study of the double racetrack magnet a so-called working model is selected from the set of optimized systems of the parameter sweep over R and Bedgreq. All further analysis will be performed with respect to this model. The system that is chosen as a working model is the system with id number 43 which is listed in the data tables in appendix B.1. Table 4.7 gives an overview of the properties of the selected working model.

4.4.1 Magnetic Field

Figures 4.11 and 4.12 present a contour plot of the magnetic field magnitude on the cross section of the double racetrack working model for the xz and yz-direction respectively. In both figures, the detector volume is indicated by a black rectangle. It can be seen from both figures that the magnitude of the magnetic field in the detector volume is homogeneous to a large extent, which was one of the field requirements. However it is important to note that the presented cross sectional slices only provide information about the magnetic field magnitude in the center of the detector volume.

4.4.2 Magnetic peak field reduction

Since the magnetic peak field (B_{peak}) determines the operating current density and therefore directly influences the volume of conductor that is needed to satisfy the magnetic field requirements, it could be beneficial to reduce its magnitude. Next to a cost reduction, a decrease of the volume of conductor also leads to a decrease of the coil widths (dcoil) and therefore reduces the dimensions of the total system. This section presents the influence of three different design adjustments on the magnitude of the magnetic peak field of the double racetrack working model.

Addition of dummyturns

A dummyturn is a spacer that is inserted between the conductor windings at the inner edge of a coil (see figure 4.14). It is usually designed as a fake coil winding which creates a certain distance between the

²B3 will never become exactly zero, but if it is smaller than 1e-4 it will be denoted as zero.

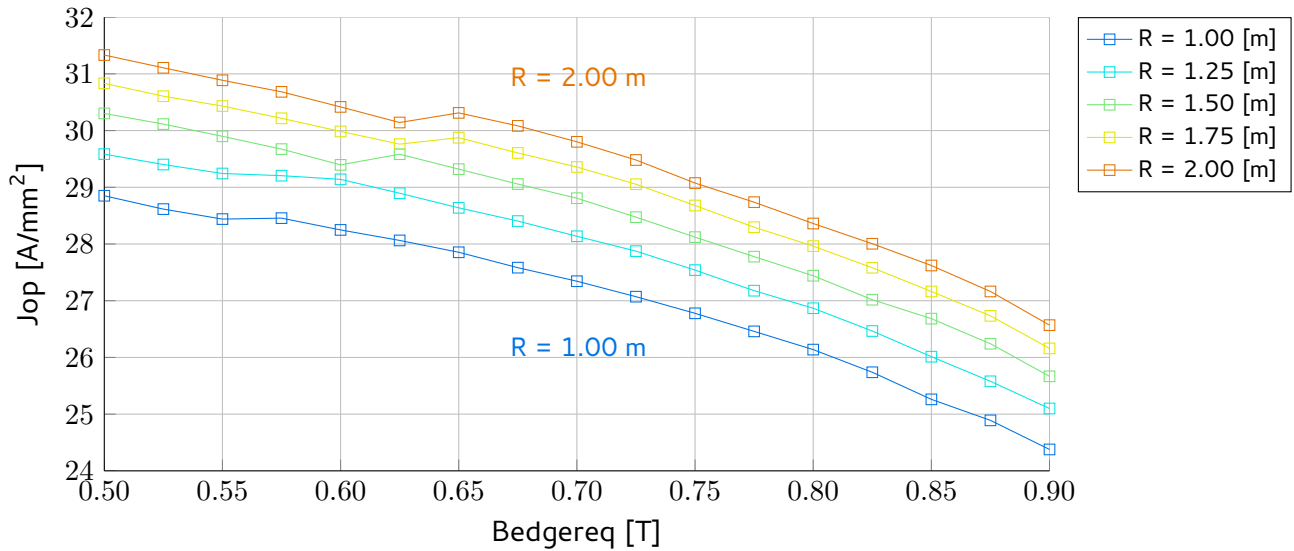


Figure 4.10: Operating current (J_{op}) as a function of the required magnetic field at the edges of the detector volume ($B_{edgereq}$) for various values of the coil corner radius (R). The curve deviations are artefacts of the MLFMM algorithm used in this optimization study.

Table 4.7: Summary of the properties of the selected working model for the double racetrack system.

Symbol	Value	Description
L1	12.68 m	Coil length in the x-direction
L2	9.84 m	Coil length in the y-direction
hsplit	6.01 m	Distance between the two racetrack coils in the z-direction
R	1.50 m	Coil corner radius
dcoil	1.05 m	Horizontal coil width
hcoil	0.1181 m	Vertical coil height
hdeck	0.05 m	Vertical spacing between two double pancake decks
Bcen	1.0 T	Magnitude of the magnetic field at the center of the detector volume
Bedge1	0.7 T	Magnitude of the magnetic field at the center of the short edge of the detector volume
Bedge2	0.7 T	Magnitude of the magnetic field at the center of the long edge of the detector volume
B3	-4.18e-06 T	Magnitude of the third harmonic field inside the detector volume
Vc	22.78 m ³	Total conductor volume
Bpeak	5.14 T	Magnitude of the magnetic peak field at the surface of the racetrack coils
Jop	28.81 A/mm ²	Operating current
I/Ic	65 %	Percentage along the loadline
Estored	1647.78 MJ	Stored Energy
L	6.907 H	Total Inductance
$\int B_z dV$	548.32 Tm ³	Volume integral over the detector volume for the z-component of the magnetic field

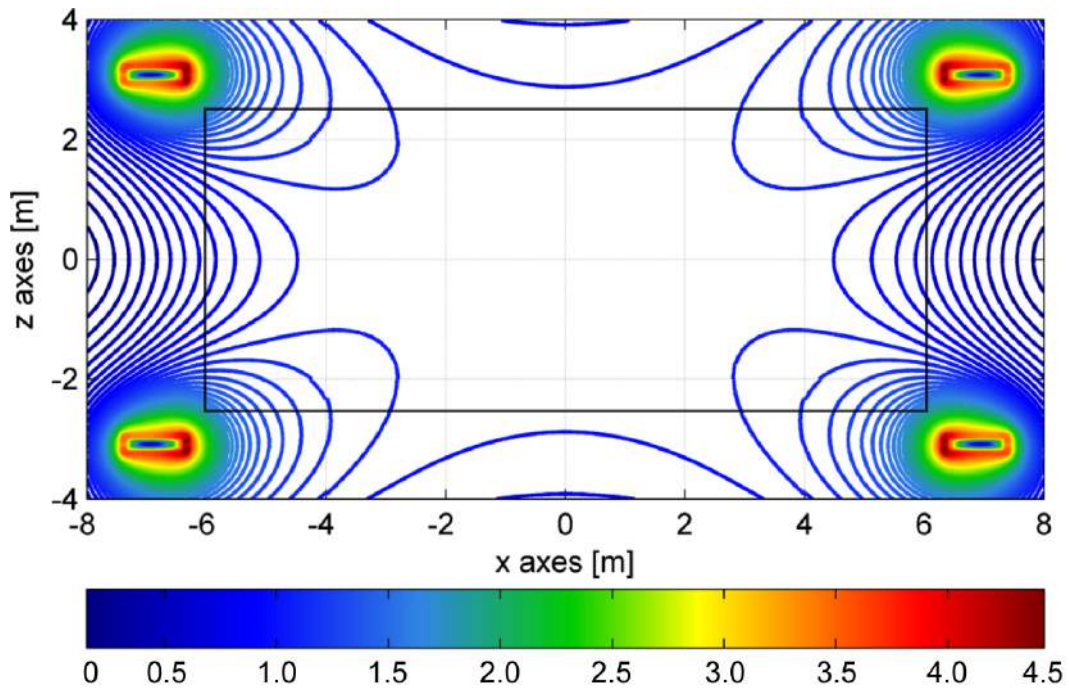


Figure 4.11: Contour plot of the magnetic field magnitude [T] in the xz -plane of the racetrack working model evaluated at $y = 0$. The detector volume is indicated by the black rectangle.

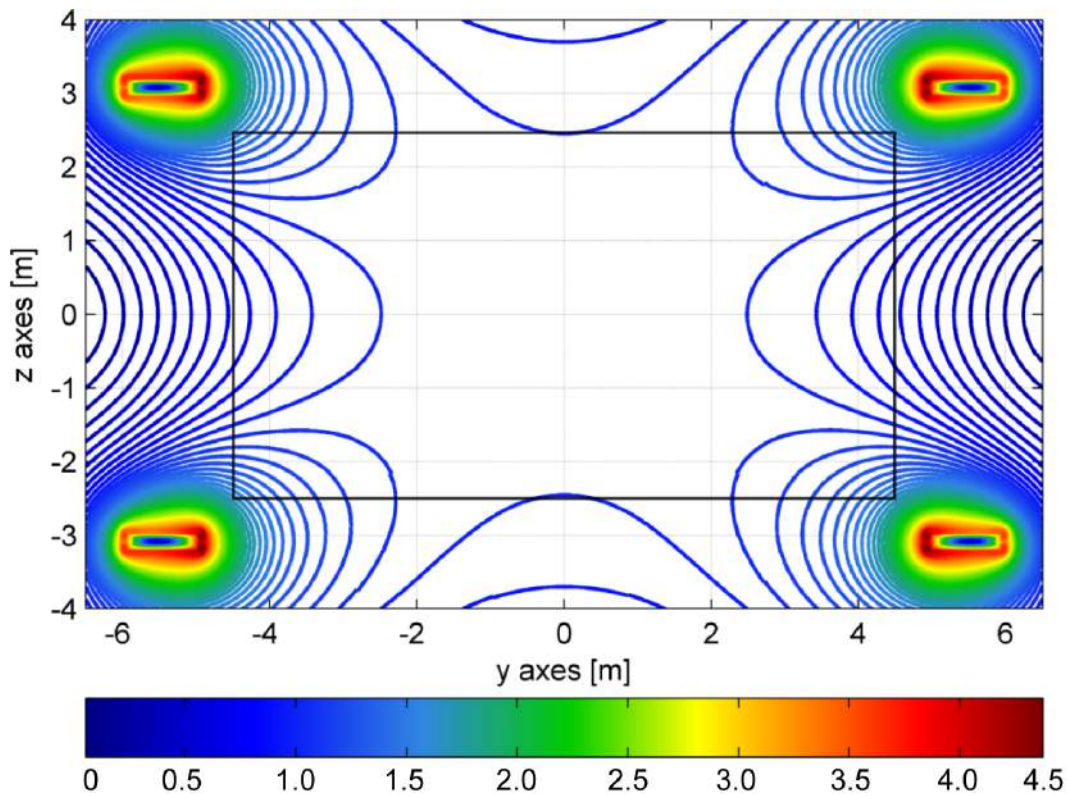


Figure 4.12: Contour plot of the magnetic field magnitude [T] in the yz -plane of the racetrack working model evaluated at $x = 0$. The detector volume is indicated by the black rectangle.

individual conductor windings of a superconducting coil. The concept of dummyturns has been successfully implemented in the ATLAS End Cap Toroids [23]. To obtain insight in the influence of dummyturns on the magnitude of the magnetic peak field of the double racetrack working model, a parametric sweep is performed. The amount of dummyturns is varied from 0 to 10 and similar to section 4.3.2 the design is optimized with respect to the set targets, which are (for comparison) equal to the magnetic field properties of the working model (see table 4.7). During the optimization, all other parameters are kept constant.

The relation between the number of dummyturns and the magnitude of B_{peak} is presented by figure 4.13. It can be seen that the addition of dummyturns decreases the magnitude of the peak field, which is also illustrated by figure 4.14. This decrease is caused by a decrease of the local effective current density, which is the result of the addition of dummyturns to the coil. Although the decrease of B_{peak} is only significant for a large number of dummyturns, figure 4.15 illustrates that the gain in operating current density and the accompanying decrease of the conductor volume are appreciable, even for a small number of dummyturns. Unfortunately, the addition of dummyturns makes coil production more difficult. However, the addition of dummyturns also has a lot of benefits and it could therefore be worthwhile to incorporate them into the double racetrack system.

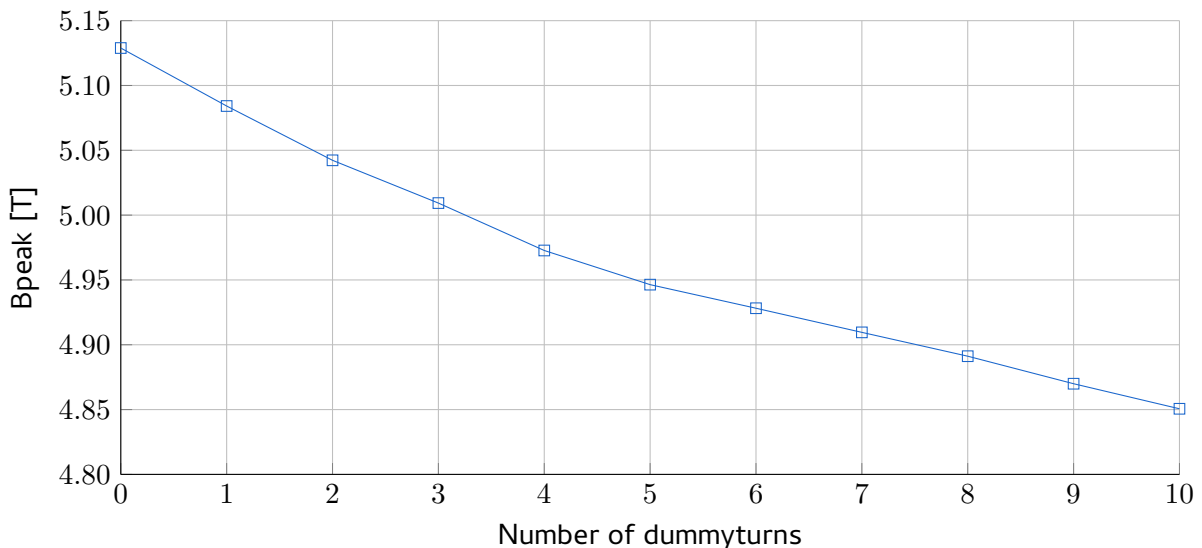


Figure 4.13: Magnitude of the magnetic peak field of the double racetrack working model as a function of the number of dummyturns.

Variation of hdeck and dshift

For the parametric study performed in section 4.3 the vertical distance between two double pancake decks (hdeck) was fixed at 50 mm, which is similar to the ATLAS Barrel Toroid [15]. The horizontal shift/displacement between two double pancake decks (dshift) was set at 0. To obtain insight in the relation between both distances and the magnitude of the magnetic peak field, two parametric sweeps are performed. Hdeck is varied from 0 mm to 2000 mm with increments of 50 mm and dshift is varied from 0 mm to 1500 mm with increments of 50 mm. Similar to section 4.3.2 the design is optimized with respect to the set targets, which are (for comparison) equal to the magnetic field properties of the working model (see table 4.7). During the optimization, all other parameters are kept constant.

Figure 4.16 illustrates the relation between the magnitude of B_{peak} and the vertical and horizontal distance between two double pancake decks. Since the combined contribution to the magnetic peak field

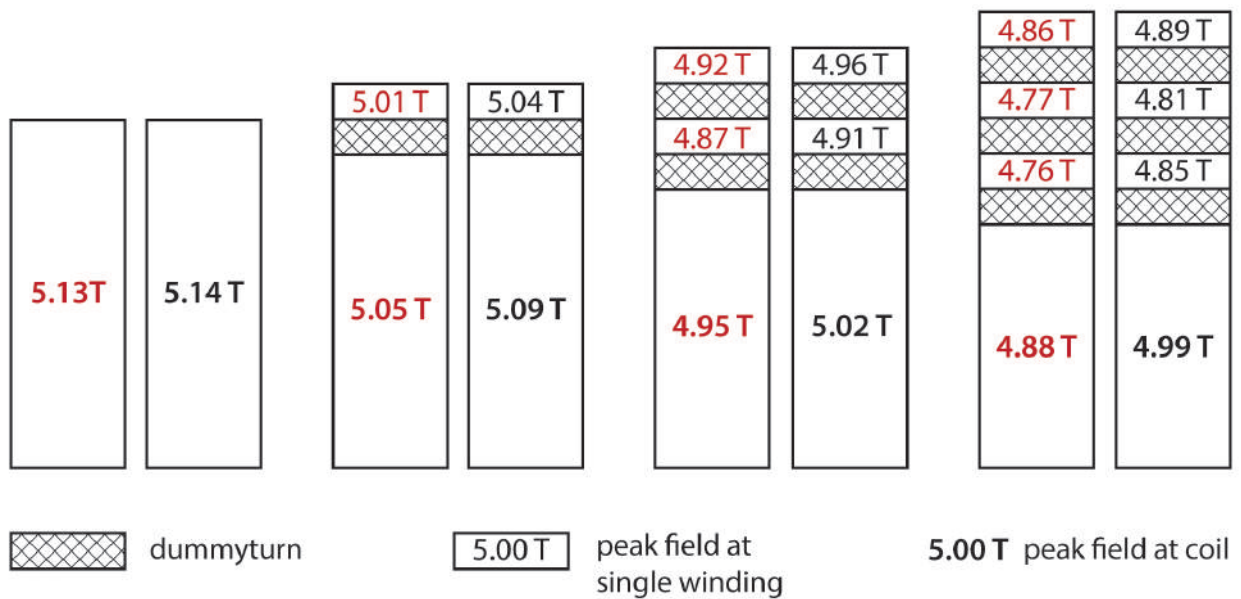


Figure 4.14: Effect of the addition of dummy turns on the magnitude of the magnetic peak field of the double racetrack working model. For each combination of two decks, the values on the left deck (indicated in red) refer to the peak field at the inner deck (which is closest to the origin) of a double racetrack configuration.

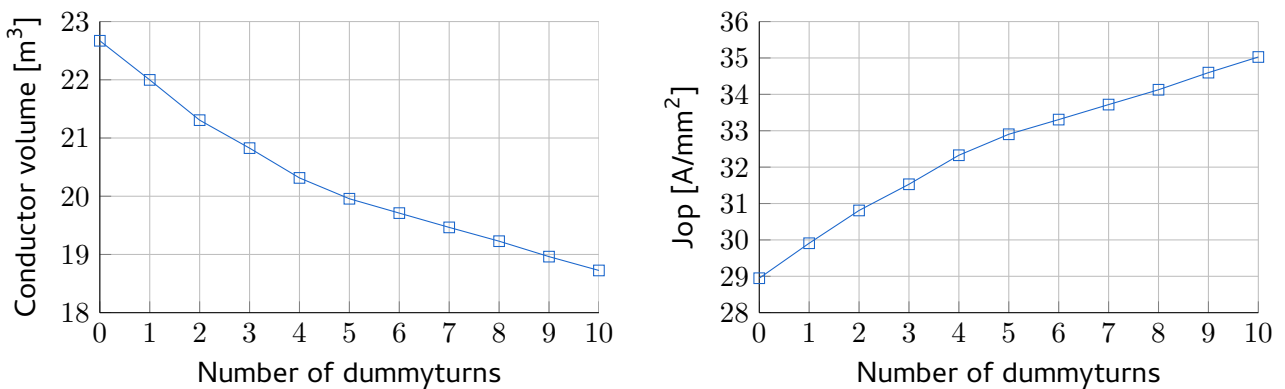


Figure 4.15: Conductor volume and operating current density as a function of the number of dummy turns for the double racetrack working model.

decreases when the decks are separated by a larger distance, B_{peak} reduces for increasing values of both h_{deck} and d_{shift} . However, reduction due to increase of h_{deck} saturates around a distance of 2000 m since from this distance on, the outer decks of both racetracks are sufficiently near by to influence each other. Since variation of both distances leads to a significant reduction of B_{peak} it could be useful to perform a more detailed study concerning their behaviour.

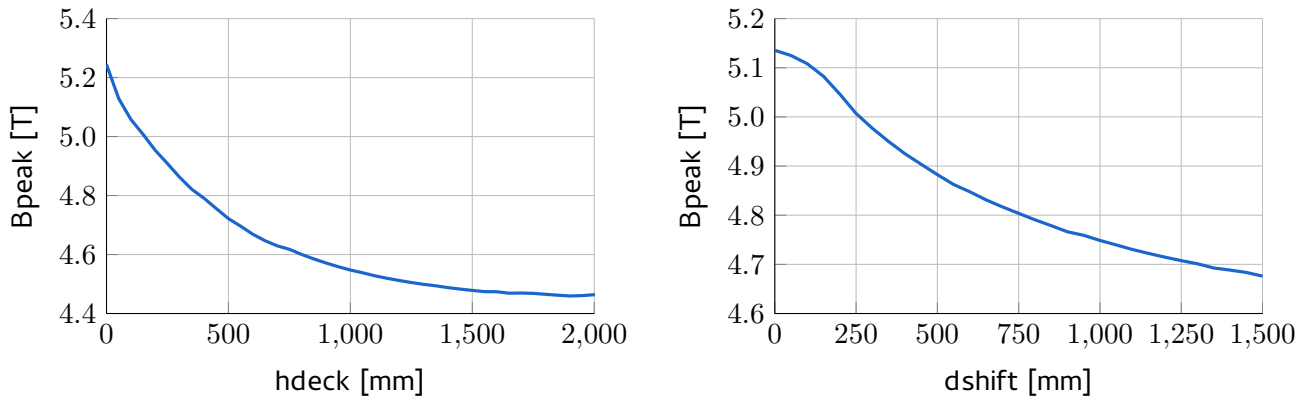


Figure 4.16: Magnitude of the magnetic peak field as a function of h_{deck} and d_{shift} for the double racetrack working model

4.5 Conclusion

A double parametric study has been performed on the double racetrack system. From the results it has become clear that the magnitude of the magnetic field on the edge of the detector volume depends on the length of the coils. By choosing the right coil dimensions, the desired magnetic field magnitude can be achieved. Since both a small system and a homogeneous magnetic field are required, a comparative assessment has to be made concerning the magnetic field magnitude at the edge of the detector volume and the accompanying coil lengths.

5 Solenoid Layout Optimization

This chapter presents the layout optimization performed for the solenoid configuration. First, the conductor settings are described followed by an overview of the design choices made concerning the geometrical design of the solenoid system. The optimization study of the solenoid system is a combination of a single optimization cycle accompanied by a parameter sweep. The aim of this sweep is to obtain insight in the relation between the geometrical parameters of the system and the properties of the magnetic field. The result of the layout study is a set of optimized models for the solenoid system. To be able to continue the preliminary design study, a so-called working model is selected. Further analysis is performed with respect to this model.

5.1 Conductor Settings

Similar to the double racetrack configuration, part of the properties of the conductor of the ATLAS barrel toroid are used as a basis for the optimization study of the solenoid magnet system. The only difference with respect to the ATLAS barrel toroid is that Magnesium di-Boride will be used as a conductor instead of Niobium Titanium. Since Magnesium di-Boride can be operated at a larger temperature range than Niobium Titanium, the operating temperature for the solenoid system will be set at 20 K instead of 4.5 K. This higher operating temperature lowers the cooling costs significantly as explained in section 3.2. The conductor settings used for the layout optimization of the solenoid are listed in table 5.1. All other parameters are equal to the racetrack system (see table 4.2 and table 4.3).

Table 5.1: Type and operating parameters of the conductor used for the layout optimization of the solenoid configuration.

Type	MgB ₂
Temperature of bath	20 K
Temperature margin	0 K
I/I _c along the loadline	65 %

5.2 Design Choices

Before performing the optimization study a few choices are made concerning the geometrical design of the solenoid system. These choices are based on experiences acquired in an earlier stage of the design study and are applied by setting the corresponding parameters to a fixed value. This section explains the reasoning behind all design choices. The fixed values for the corresponding parameters are summarized in table 5.2.

Horizontal coil width – dcoil Previous optimization steps revealed that there exists no optimal value for the horizontal width of the coils (dcoil). In order to produce the required magnetic field of 1 T in the center of the detector volume, the coil width tends to converge to very low values. Since the possibility

of manufacturing puts a lower limit on the width of the coil, d_{coil} is set to a realistic value. The fixed value for the horizontal coil width is based on the size of the conductor of the ATLAS barrel toroid (see table 4.2). The smallest possible value for the d_{coil} is the width of one winding of which the long side is placed along the vertical z -axis.

Coil length – L1 and L2 The values of the length of the coil in the x -axis (L1) and y -axis (L2) are fixed in such a way that the solenoid encloses the detector volume without any extra spacing between the detector volume and the magnet system. This choice originates from the fact that the magnitude of the magnetic field produced by the solenoid drops over the distance from the coil to the center of the detector volume. In order to create the required central magnetic field by means of the lowest possible current density, the coil has to be positioned as close as possible to the center of the detector volume. Since placement of the magnet system within the detector volume is not an option (see section 1.3), the fixed values for the coil lengths are bounded by the size of the detector volume.

Since the horizontal coil width is fixed to a value that is larger than the necessary width to create a magnetic field of 1 T in center of the detector, the central magnetic field will (for relevant values of h_{coil}) be larger than the required value of 1 T.

Table 5.2: Summary of the design choices made for the solenoid configuration, the corresponding parameters and their values.

Parameter	Value	Description
d_{coil}	59.05 mm	Horizontal coil width
L1	12.00 m	Coil length in the x -direction
L2	9.00 m	Coil length in the y -direction

5.3 Parametric Study R and h_{coil}

As described in section 3.3.2 the optimization study performed in this report is based on the combination of a single optimization cycle accompanied by a parameter sweep (see section 2.4). For the solenoid system a sweep is performed over h_{coil} and R. An important difference with respect to the parametric study performed for the double racetrack configuration (section 4.3) is that for the solenoid no loadline fit is performed during the optimization step (as explained in section 3.3.3). This choice originates from the fact that the magnitude of the magnetic field at the center of the detector (B_{cen}) is bounded by a lower limit due to the geometry of the solenoid (section 5.2). It will always exceed the required value of 1 T when the system is operated at a loadline percentage of 65%. To account for this over performance, the operating current (J_{op}) is optimized in order to achieve the desired value for B_{cen} .

For the parametric study of the radius of the coil and the coil height, the values of both R and h_{coil} are swept over a specific range. R is varied from 1.00 m to 2.00 m with steps of 0.25 m and h_{coil} is varied from 1.00 m to 10.00 m with steps of 0.25 m. For comparison, the parametric study is repeated for a solenoid containing Niobium Titanium as a conductor instead of Magnesium di-Boride. For the Niobium Titanium case, conductor settings similar to the racetrack configuration are applied (table 4.1). The targets and corresponding variables that are used to perform the optimization for each different combination of R and h_{coil} are presented in table 5.3.

The parametric study resulted in a list of optimized models for all values of R and h_{coil} . Because the values of the coil heights that are relevant for this design study lie in the range of 4.0 m to 6.5 m, only

Table 5.3: Explanation of the target and variable used for the parametric study of R and hcoil

Target	Variable	Description
Bcen = 1 T	Jop	Variation of the operating current will influence the magnitude of the magnetic field in the center of the detector. In order to achieve a central magnetic field of 1 T the operating current is adapted with respect to the coil cross-section of the solenoid.

specifications of the models that contain a coil height within this range are listed in appendix B.3. Since no loadline fit is performed for the optimization of the current density of the solenoid system, the resulting models are independent of conductor choice.

Figure 5.1 presents the operating current density (J_{op}) required to achieve a central magnetic field of 1 T as a function of the coil height (h_{coil}) of the solenoid. Furthermore, it illustrates the relation between h_{coil} and the engineering current density (J_e) of Magnesium di-Boride and Niobium Titanium at a temperature of 20 K and 4.5 K respectively. It can be seen that the engineering current density of MgB_2 is shifted with respect to that of Nb-Ti. This is caused by the difference in operating temperature between the MgB_2 and the Nb-Ti conductor. Next to that, the required J_{op} becomes smaller with increasing h_{coil} . This can be explained by the fact that for a larger coil height the total volume of superconductor increases. Therefore, less current per cross-sectional area is needed in order to achieve the same central magnetic field. The figure also shows that for a certain range of h_{coil} values the required operating current density is larger than the engineering current density of both MgB_2 and Nb-Ti. Therefore, all models with a coil height that lies within this range are not realizable.

The relation between the magnitude of the third harmonic field and the height of the coil is illustrated by figure 5.2. The plot shows that although the value of the third harmonic becomes closer to zero for increasing coil height, a true homogenous magnetic field in the detector volume is not possible since the magnitude of the third harmonic will never become smaller than $1e-4$ T.

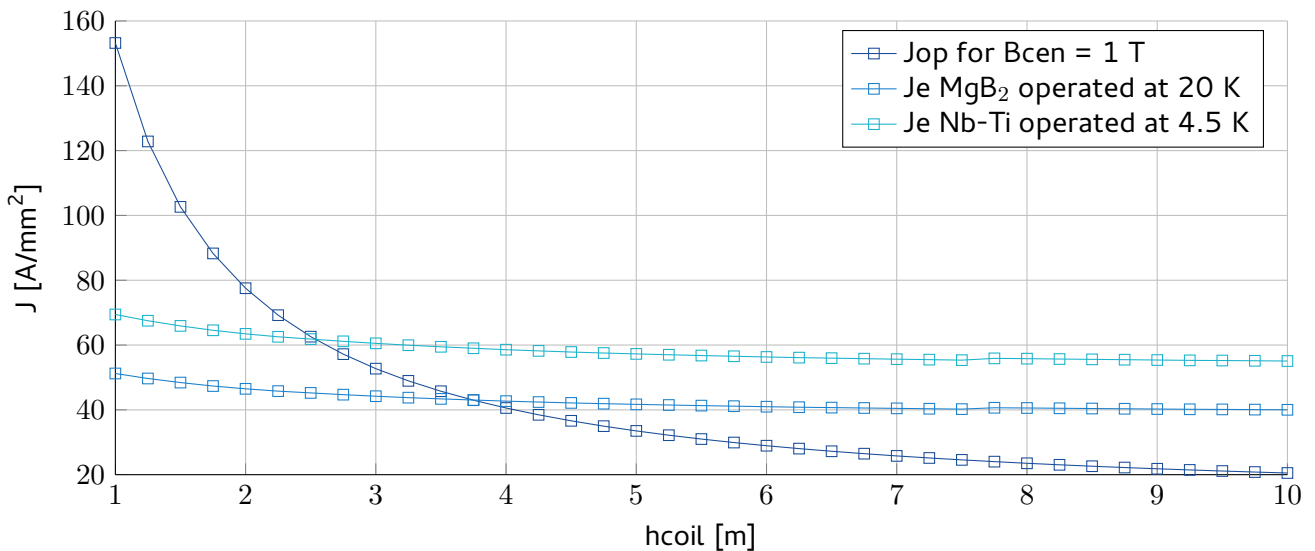


Figure 5.1: Operating current density (J_{op}) and engineering current density (J_e) of Nb-Ti and MgB_2 as a function of the height of the coil (h_{coil}). Note that only models with an operating current density smaller than the engineering current density are realizable.

5.4 Working Model and Analysis

The parametric study presented in section 5.3 resulted in a list of optimized models for the solenoid system. Similar to the double racetrack configuration (section 4.4) a working model is selected to perform further analysis on. The system that is chosen as a working model is the configuration with id number 93 which is listed in the data tables in appendix B.3. Table 5.4 gives an overview of the properties of the selected working model.

Table 5.4: Summary of the properties of the selected working model for the solenoid system.

Symbol	Value	Description
L1	12.00 m	Coil length in the x-direction
L2	9.00 m	Coil length in the y-direction
R	1.50 m	Coil corner radius
dcoil	0.05905 m	Horizontal coil width
hcoil	5.50 m	Vertical coil height
Bcen	1.0 T	Magnitude of the magnetic field at the center of the detector volume
Bedge1	1.47 T	Magnitude of the magnetic field at the center of the short edge of the detector volume
Bedge2	1.41 T	Magnitude of the magnetic field at the center of the long edge of the detector volume
B3	-206 mT	Magnitude of the third harmonic field inside the detector volume
Vc	12.86 m ³	Total conductor volume
Bpeak	2.16 T	Magnitude of the magnetic peak field at the surface of the solenoid
Jop	31.00 A/mm ²	Operating current
I/Ic MgB ₂	75 %	Percentage along the loadline for a working model with MgB ₂ as a conductor
I/Ic Nb-Ti	54 %	Percentage along the loadline for a working model with Nb-Ti as a conductor
Estored	640.95 MJ	Stored Energy
L	2.126 H	Total Inductance
$\int B_z dV$	578.82 Tm ³	Volume integral over the detector volume for the z-component of the magnetic field

5.4.1 Magnetic Field

Figures 5.3 and 5.4 present a contour plot of the magnetic field magnitude on the cross section of the solenoid working model for the xz and yz-direction respectively. In both figures, the detector volume is indicated by a black rectangle. It can be seen that the magnitude of the magnetic field varies over the total conductor volume and is therefore, as indicated in section 5.3, inhomogeneous. However, the magnetic field magnitude inside the detector volume never decreases below the value of 1 T, which is the required magnitude at the center of the detector. It is important to note that the presented cross sectional slices only provide information about the magnetic field magnitude in the center of the detector volume.

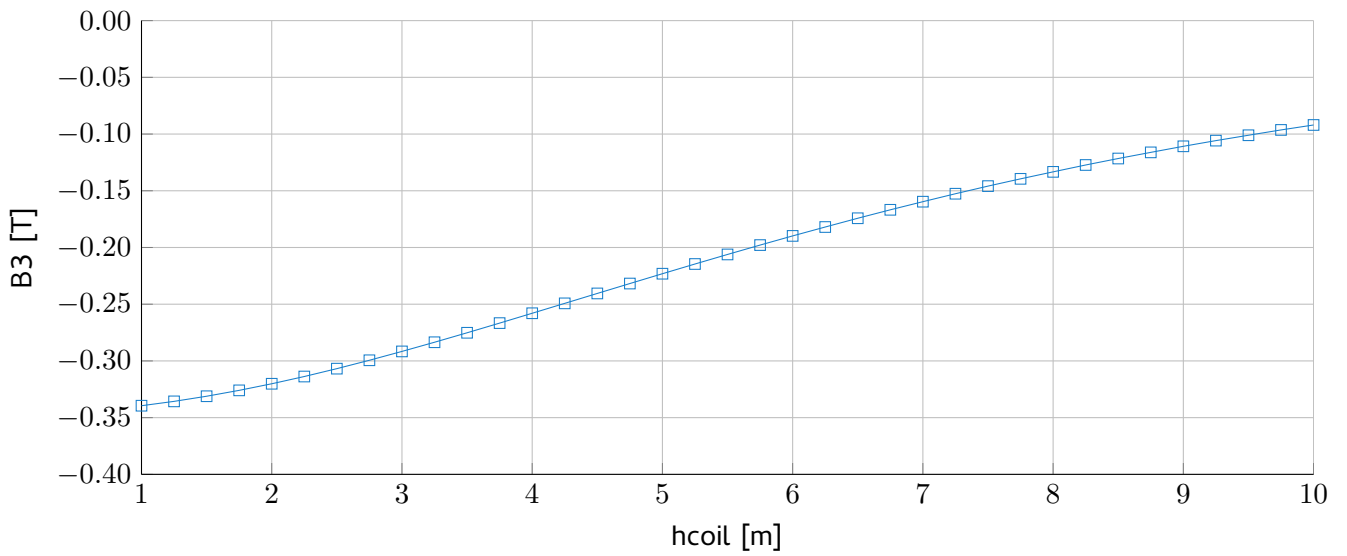


Figure 5.2: Magnitude of the third harmonic field (B_3) as a function of the height of the coil (h_{coil}). Note that for relevant coil heights the third harmonic field will never become smaller than the desired value of $1e-4$ T, therefore the magnetic field within the detector will never be truly homogeneous.

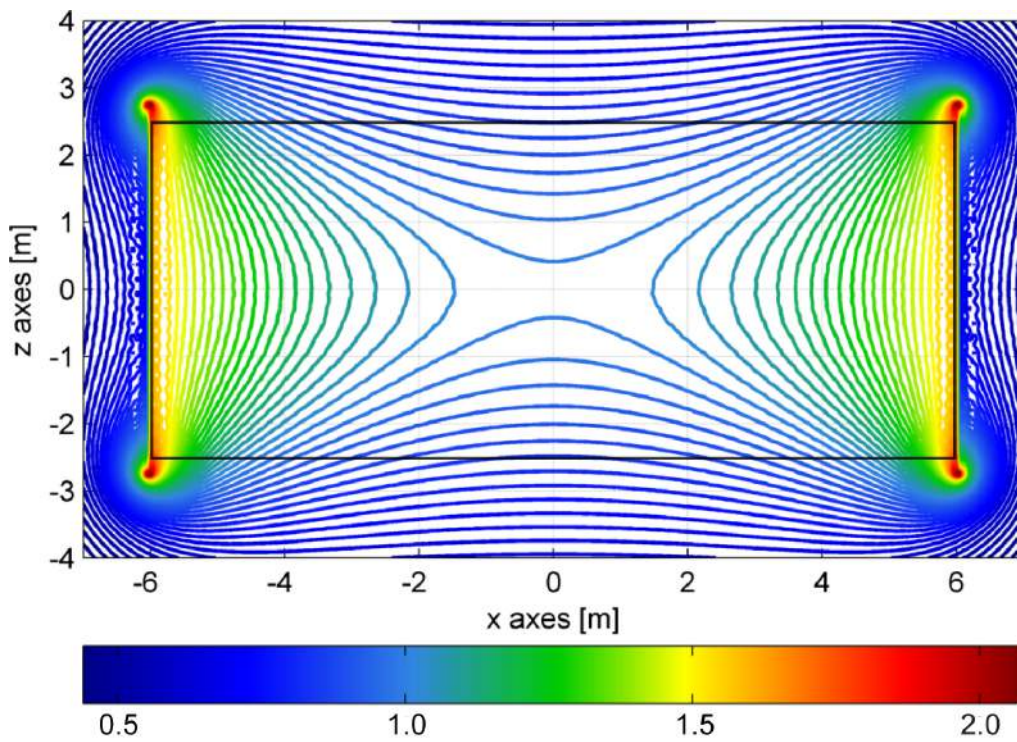


Figure 5.3: Contour plot of the magnetic field magnitude [T] in the xz -plane of the solenoid working model evaluated at $y = 0$. The detector volume is indicated by the black rectangle.

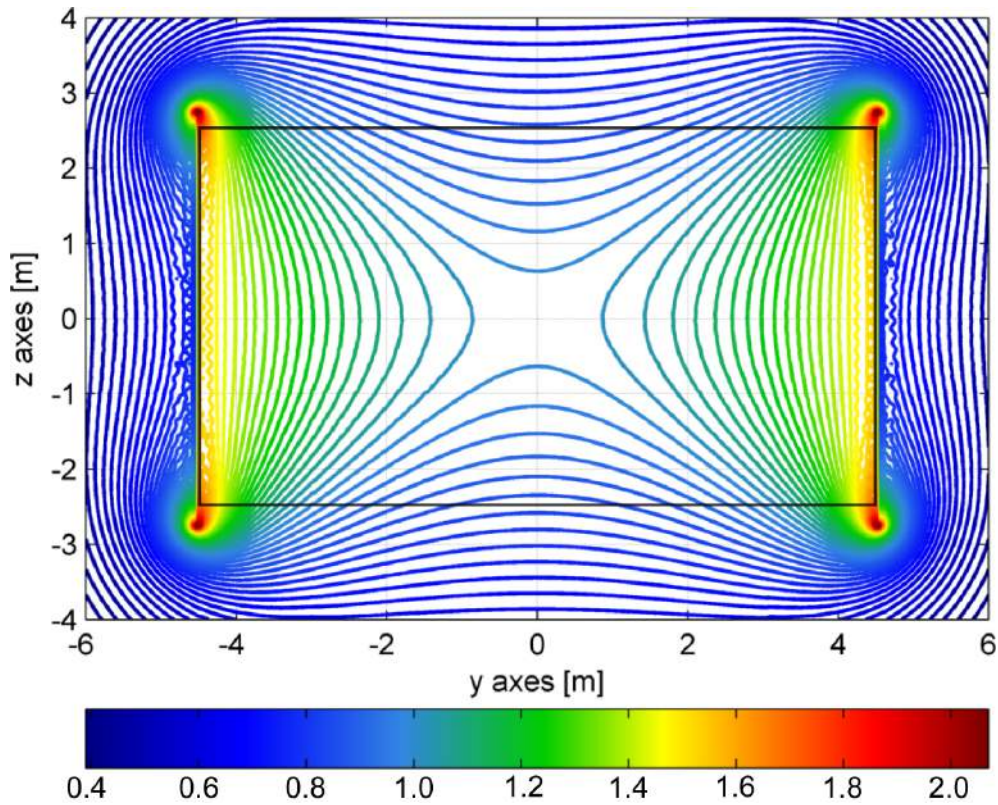


Figure 5.4: Contour plot of the magnetic field magnitude [T] in the yz -plane of the solenoid working model evaluated at $x = 0$. The detector volume is indicated by the black rectangle.

5.5 Conclusion

A parametric study has been performed on the solenoid system. From the results it has become clear that it is possible to meet the magnetic field requirements by making use of both Nb-Ti and MgB₂ as a conductor. Next to that, it was illustrated that it is impossible to achieve a true homogeneous magnetic field in the detector volume. On the other hand the required magnitude of the magnetic field can be easily generated by the solenoid system.

6 Quench Analysis

To obtain insight in the thermal behaviour of both the double racetrack and solenoid system a computational quench model was created. This chapter describes the methods used for the determination of the average temperature rise and peak temperature by means of this model. It presents the results of various temperature calculations and illustrates the influence of quench protection tools. The final section compares the quench model to the Tampere University quench code and provides a graphical illustration of the heat distribution after quenching.

6.1 Determination of the average temperature rise

The temperature increase due to quenching can cause serious damage to a superconducting coil. With regard to quench protection, it is important to know the (peak) value of the temperature a system attains after quenching. By making use of the heat equation [24] and assuming that the total amount of stored energy (equation 2.2) will be absorbed homogeneously by the conductor windings, the average temperature rise of the coils can be estimated by solving

$$\frac{1}{2}LI^2 = \int_{T_{bath}}^{T_{av}} C_p(T) dT, \quad (6.1)$$

where $C_p(T)$ is the heat capacity, T_{bath} is the operating temperature of the magnet and T_{av} is the average temperature that will be reached after absorption of the (total amount of) stored energy.

Since the conductor used in this design study is composed of multiple materials, the heat capacity has to be calculated separately for each, regarding their relative volume (the used specific heat capacities of the relevant materials are presented in figure 6.3). Table 6.1 presents the calculated average temperature rise for the double racetrack and solenoid working model (presented in section 4.4 and 5.4). For the double racetrack configuration the average temperature rise is determined for two cases, one in which the energy is absorbed by one coil and one in which the energy is spread over the total system of four coils. Because the volume increases by a factor four, the average temperature rise for a spread over the total system is much lower than for a spread over only one coil. Due to its relatively small stored energy, the solenoid configuration heats up much less compared to the double racetrack.

Table 6.1: Calculated average temperature rise (T_{av}) for the double racetrack and solenoid working model.

Configuration		T_{av}
Double racetrack	1 coil	222.1 K
	4 coils	114.1 K
Solenoid		98.3 K

Because the desired material property data for pure Aluminium was unavailable, calculations were performed using Aluminium5083 [25]. The material properties of G10 [26] were chosen for calculations of the fiberglass insulation layer. These choices could cause small deviations in the calculated average temperature rise. Nevertheless, the calculated average temperature rise provides some useful insights with respect to the extent of heating of the different systems.

6.1.1 Influence of the stabfactor

To obtain insight in the influence of the percentage of stabilizer (stabfactor) on the average temperature rise of the racetrack configuration, a parametric sweep is performed for both a spread over one coil and over four coils. Similar to the parametric study for the double racetrack configuration (section 4.3), the relevant variable is varied over a fixed range and for each different value the design is optimized with respect to the set targets. After the design optimization, the average temperature rise is determined. The stabfactor is varied from 20% to 90% with increments of 5%. For comparison, the targets are set equal to the magnetic field values of the racetrack working model (section 4.4). The relation between the stabfactor and the average temperature rise is presented in figure 6.1.

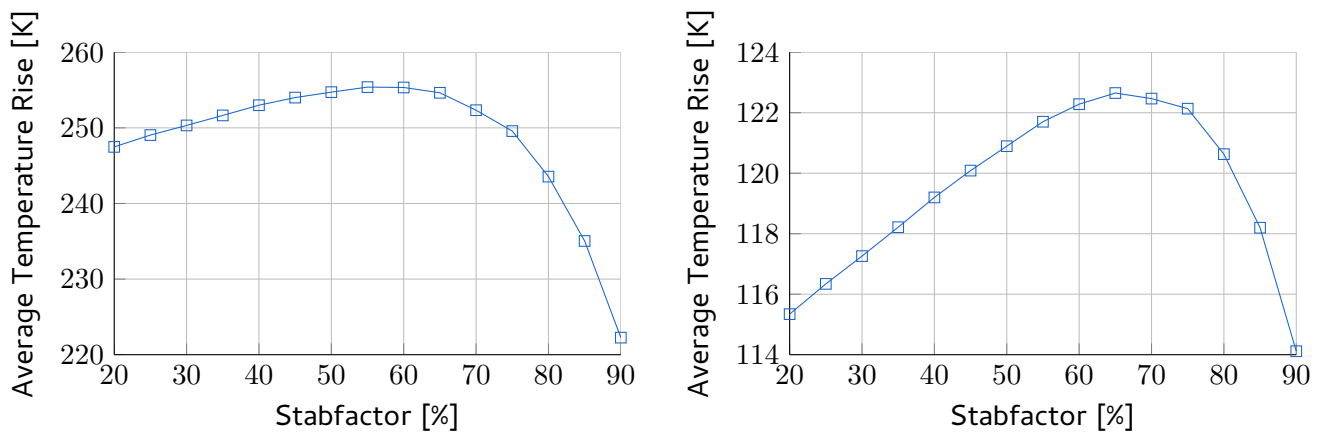


Figure 6.1: Average temperature rise as a function of the percentage of stabilizer in the conductor volume (stabfactor) for two cases of the double racetrack configuration. The left figure illustrates the relation for a single coil whereas the right figure illustrates the relation for a spread over four coils.

Both graphs illustrate that the average temperature rise (T_{av}) reaches a maximum for a stabfactor of approximately 60%. For large stabfactor values, the average temperature rise decreases. This can be explained by the large specific heat capacity of Aluminium (figure 6.3), which increases the total heat capacity and therefore decreases T_{av} . Furthermore, the average temperature rise also decreases for small stabfactor values. This seems contradictory, but can again be explained by looking at the specific heat capacities in figure 6.3. When the percentage of Aluminium decreases the volume of Copper and Nb-Ti increases proportionally (see figure 6.2). Although Copper and Nb-Ti have a smaller specific heat capacity than Aluminium, their densities are larger (by a factor three and two respectively) and therefore their contribution to the total heat capacity becomes, at a certain point, large enough to decrease T_{av} . It is important to note that for small stabfactor values, the volume of Copper increases by a large amount. Since Copper is very expensive and next to that, has a large density, it could be favourable to minimize its use.

Although a stabfactor smaller than 90% does not lead to a lower average temperature rise, it can still be favourable to allow a larger T_{av} (which can be compensated by all kinds of quench protection). When the relative amount of superconductor increases and the loadline percentage is kept constant, the current

density increases. This leads to a slight increase of the stored energy, but more important, allows dcoil to be much smaller (see figure 6.2). Since the system dimensions are considered as a limiting factor for this design study, smaller coil widths could be beneficial.

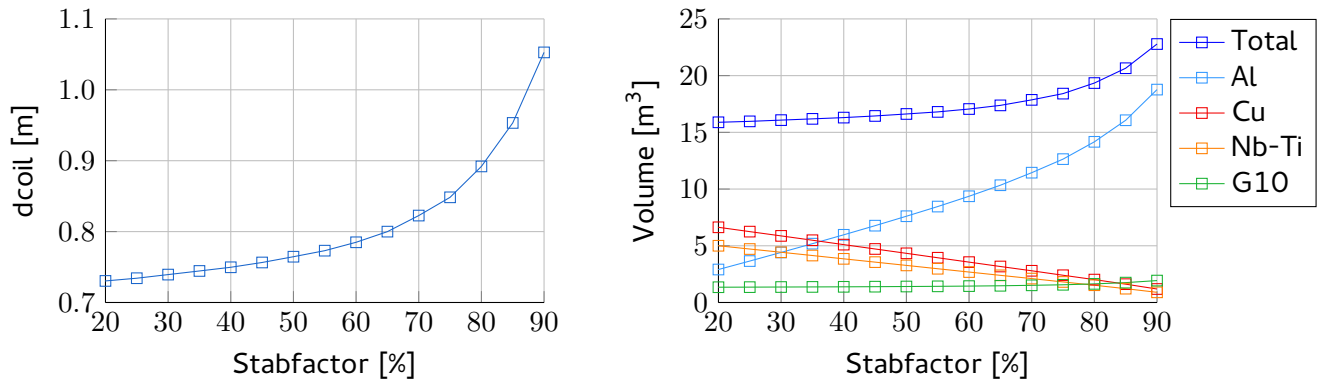


Figure 6.2: Coil width (left) and total conductor volume (right) as a function of the percentage of stabilizer in the conductor volume (stabfactor) for the double racetrack configuration. The right graph illustrates the variation of the total individual and combined volumes of the conductor materials.

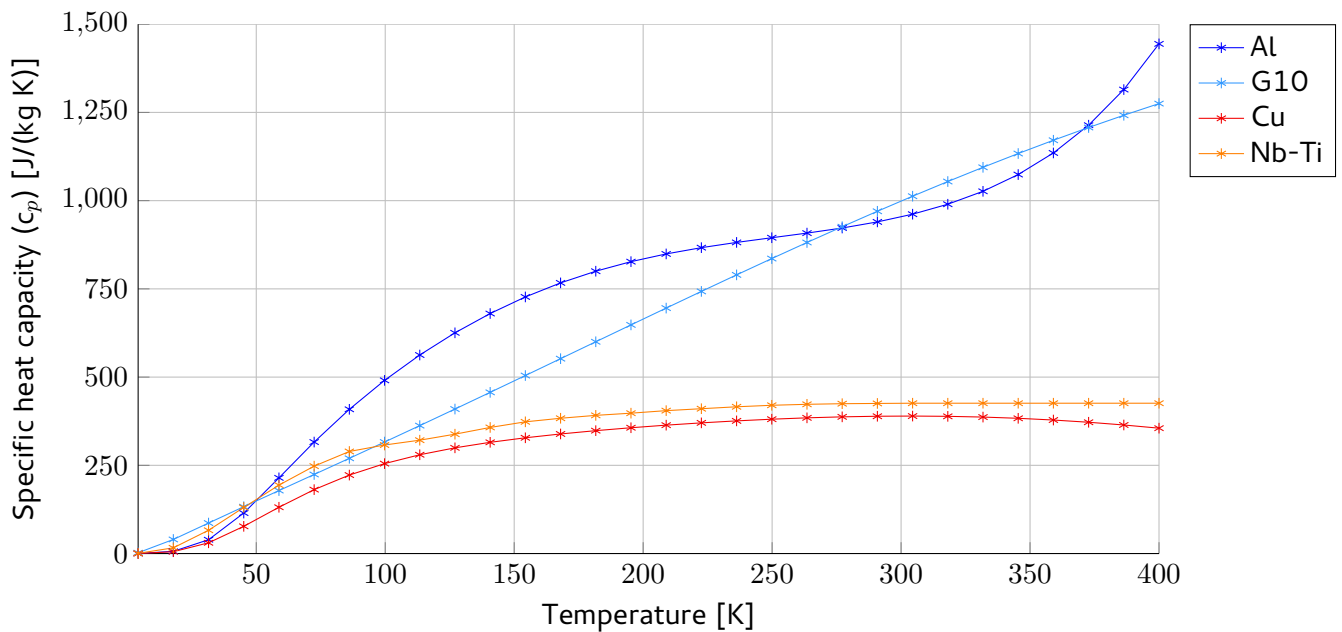


Figure 6.3: Specific heat capacity (c_p) as a function of temperature for Aluminium5083 (Al) [25], Fiberglass Epoxy (G10) [26], OFHC Copper (Cu) [27] and Niobium Titanium(Nb-Ti) [28] .

6.2 Determination of the peak temperature

The next step is to perform a more accurate calculation of the peak temperature (T_{peak}) that will be attained after quenching. To obtain the peak temperature, the coils are divided in multiple elements after which a discrete form of the heat equation [24] including the diffusion term can be solved using a finite difference method. The discrete form can be derived from Fourier's one-dimensional equation for heat conduction [29]. For each individual element, the amount of heat that enters and leaves the system and the heat production are considered.

A set of coupled differential equations is used to model the behaviour of the quench. The time-current

relation is given by

$$L \frac{dI}{dt} = -IR_{tot}, \quad (6.2)$$

where I is the current in A, L is the inductance in H and R_{tot} is the resistance of the total coil in Ω . In addition the time-temperature relation is given by

$$C_p \frac{dT}{dt} = -\kappa A \frac{dT}{dx} + I^2 \rho, \quad (6.3)$$

where T is the temperature in K, I is the current in A, κ is the thermal conductivity in $\frac{J}{Km}$, A is the cross-sectional area of the coil in m^2 , ρ is the electrical resistivity in Ωm and C_p is the heat capacity in $\frac{J}{K}$. The first part of the equation describes the heat transfer whereas the second part describes the heat production due to the transition to the normal state.

The Matlab function `ode15s` [30], which is especially meant for stiff problems, is used to solve the system of differential equations for each element. Table 6.2 presents the calculated peak temperatures for two cases of the double racetrack and the solenoid working model (presented in section 4.4 and 5.4). The material properties used for this calculation are similar to section 6.1. The peak temperatures for both the solenoid and the double racetrack configuration are much larger than the average temperature rise. This can be explained by the fact that for the calculation of T_{av} homogeneous heating over the total coil volume is assumed whereas T_{peak} is the local peak temperature reached by one of the coil elements. However, it should be noted that for the calculation of the peak temperature, it is assumed that the heat is only absorbed by the coil windings¹. The corresponding temperature and current development for the single double racetrack coil and solenoid system are presented in figures 6.4, 6.5 and 6.6.

Table 6.2: Calculated peak temperature (T_{peak}) for the double racetrack and solenoid working model.

Configuration		T_{peak}
Double racetrack	1 coil	346.5 K
	4 coils	198.6 K
Solenoid		179.7 K

Since temperatures below 120 K are considered safe (section 2.3.3), the peak temperatures of both the solenoid and double racetrack configuration are far above the safe region. It is possible to reduce the peak temperature by means of a quench protection system. However, it should be noted that a failure of this protection system is unacceptable.

6.2.1 Influence of an external dump resistor and quench heaters

The peak temperature of a system can be reduced by addition of an external dump resistor and quench heaters. This section presents the results of peak temperature calculations for the double racetrack and solenoid working model including both protection tools.

Figure 6.7 illustrates the temperature variation with time for a single double racetrack coil and solenoid system both containing an external dump resistor. For this calculation both coils are divided in 50 indi-

¹This is a worst case assumption since normally part of the heat is for instance absorbed by the mechanical structure or dissipated by a dump resistor.

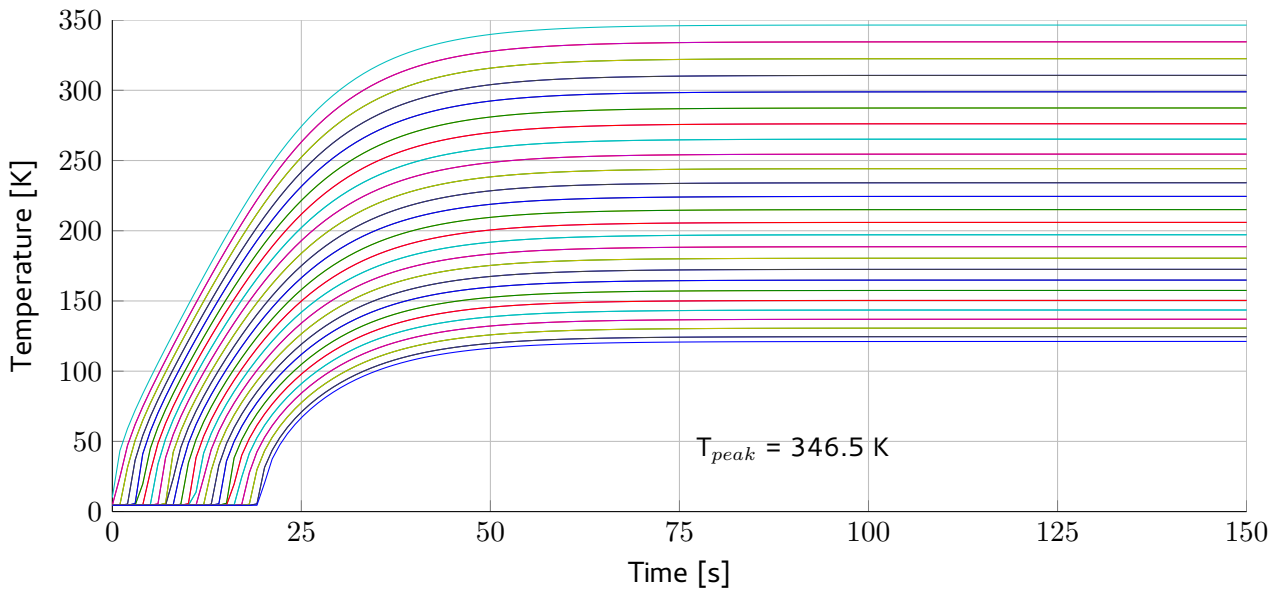


Figure 6.4: Temperature as a function of time for a single coil of the double racetrack working model (section 4.4), which is divided into 50 different elements. Each line presents the time-temperature relation for and individual element.

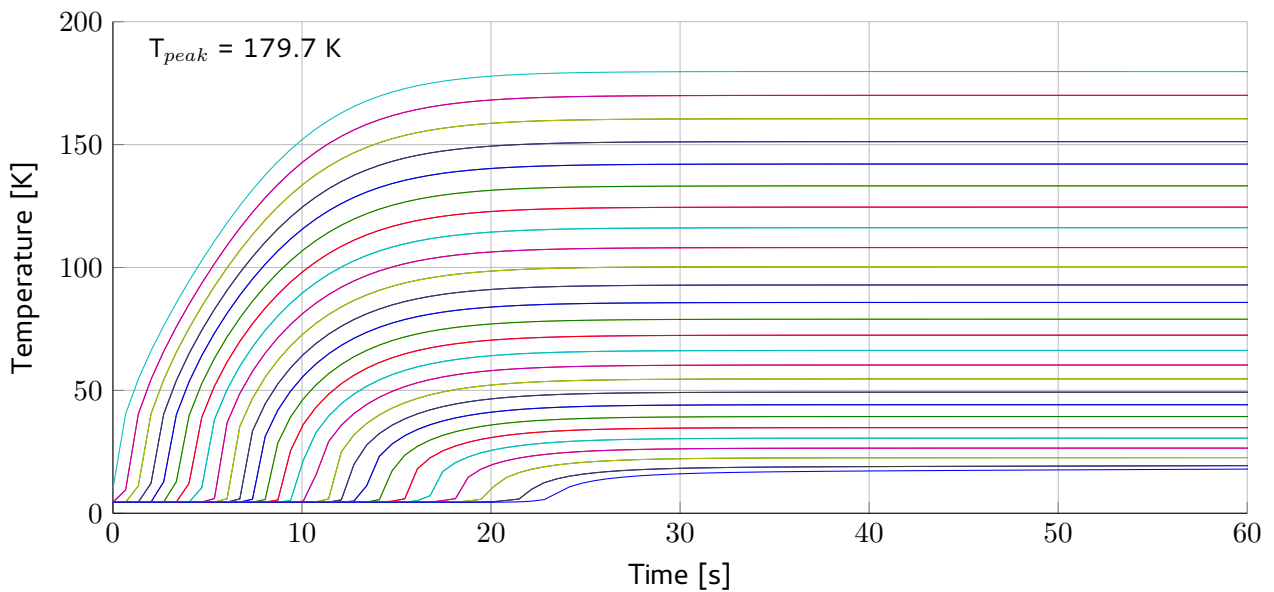


Figure 6.5: Temperature as a function of time for the solenoid working model (section 5.4), which is divided into 50 different elements. Each line presents the time-temperature relation for and individual element.

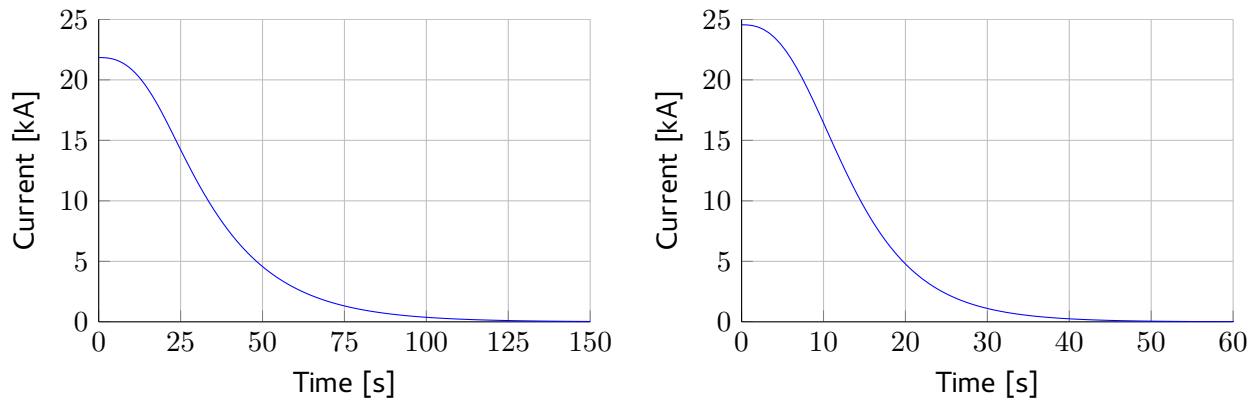


Figure 6.6: Current as a function of time for a single coil of the double racetrack working model (left) and for the solenoid working model (right). Both systems are divided in 50 different elements.

vidual elements. Because the voltage over the coil is commonly limited at 1 kV, the dump resistance is calculated by $R_d = \frac{1000}{I_0}$ where I_0 is the operating current of the system. Since part of the released energy is dissipated in the external resistor, the peak temperature for both systems decreases.

The influence of a quench heater on both the single double racetrack coil and solenoid system is presented in figure 6.8. For this calculation both coils are divided in 50 individual elements. Because by firing quench heaters extra heating spots are created, the heat is spread in a more uniform way over the coil and therefore the peak temperature decreases. For this model, a quench heater is designed as an individual element with an initial temperature above the critical temperature. It is important to note that the calculations presented in figure 6.8 could deviate from experimental results. This is a consequence of the position of the quench heater. For both systems the element positioned at the largest distance from the element that quenches is chosen to be the quench heater. This choice can be regarded as the best case scenario in which the effect of the quench heater is at maximum. Since the position of a quench is unpredictable, in many cases the peak temperature will become slightly larger than calculated. This effect reduces when multiple quench heaters are added to the system.

Previous calculations illustrate that the peak temperature of a single coil of the double racetrack working model is, even after addition of an external dump resistor and quench heaters, far above the safe region. Though the peak temperature can be further reduced by adding more quench heaters, it is also beneficial to spread the released energy over multiple coils (see section 6.2). To spread the heat over all four coils, quench heaters have to be placed at each coil. Figure 6.9 presents the variation of temperature and current with time for the total double racetrack working model with two quench heaters per coil. It can be seen that this is still not sufficient to lower the peak temperature to an acceptable value.

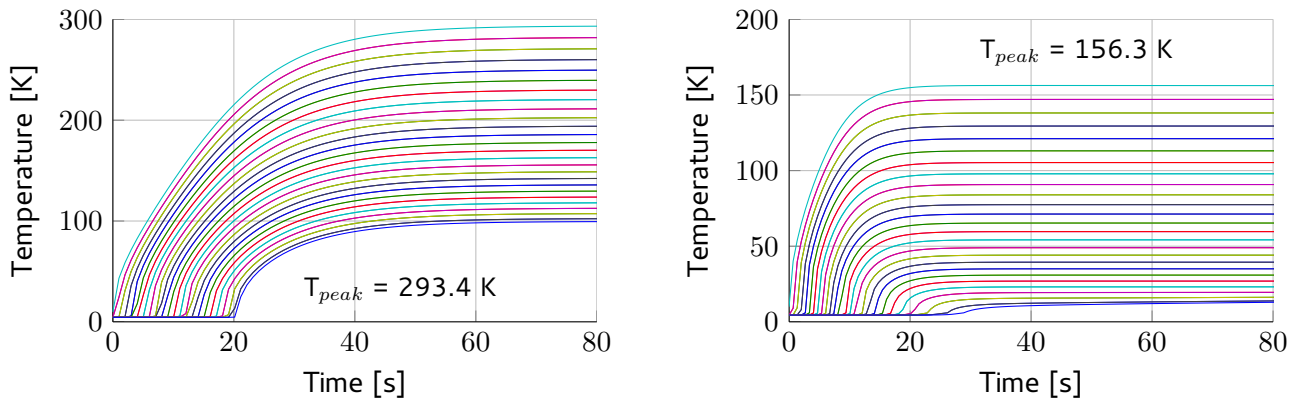


Figure 6.7: Temperature as a function of time after addition of an external dump resistor. The left graph illustrates the temperature-time relation for a single coil of the double racetrack working model whereas the right figure illustrates the temperature-time relation for the solenoid working model.

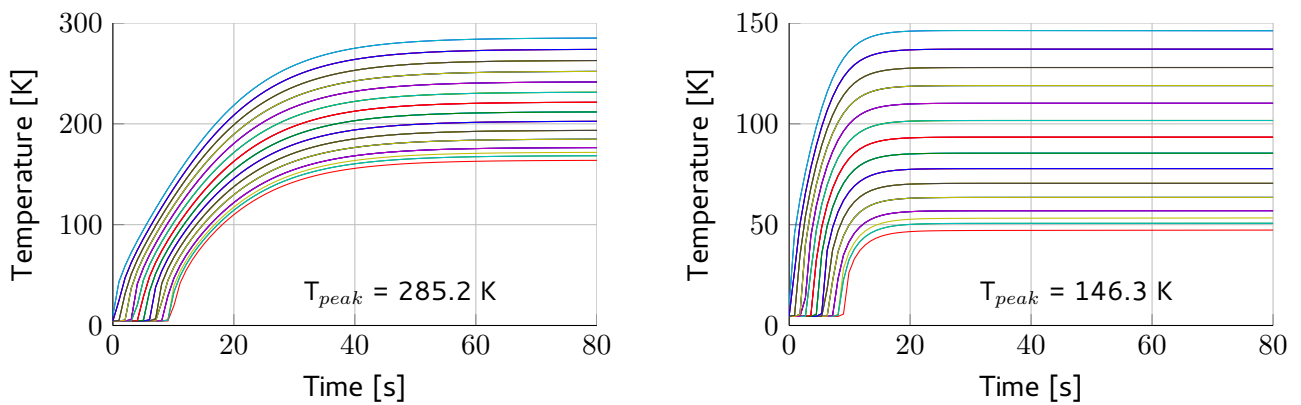


Figure 6.8: Temperature as a function of time after addition of a quench heater. The left graph illustrates the temperature-time relation for a single coil of the double racetrack working model whereas the right figure illustrates the temperature-time relation for the solenoid working model.

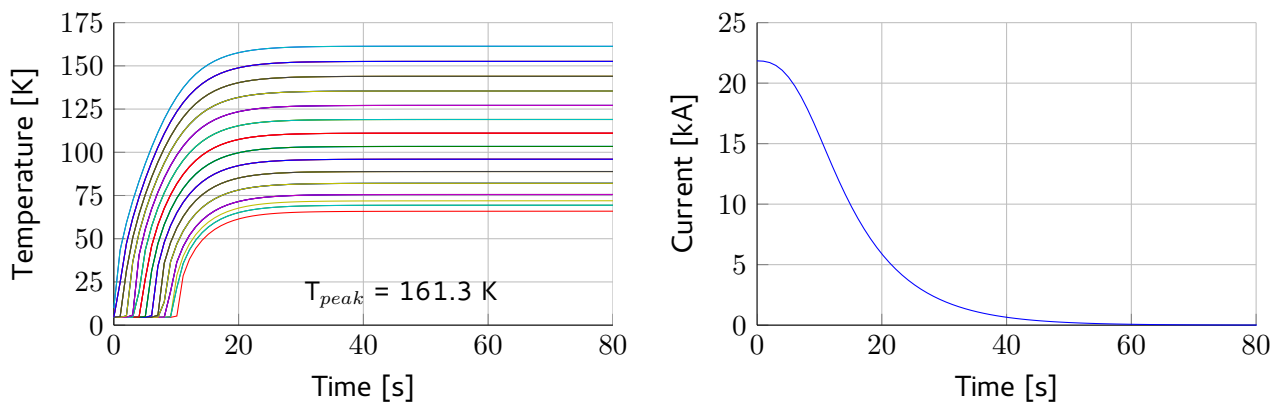


Figure 6.9: Temperature and current as a function of time for the total double racetrack working model. The heat is spread over the total system by two quench heaters per coil.

6.3 Comparison of the quench model

For the purpose of testing the Field mesh export functions that interact with the Tampere University (Finland) quench codes a test model was needed. To make double use of this opportunity it was decided to test the code on a single coil of the double racetrack working model (section 4.4). Figure 6.11 presents a graphical representation of the heat distribution over the coil volume for the first 21 seconds after quenching. It can be seen that the heat spreads relatively homogeneous over the coil volume. The numerical results from Tampere are plotted together with the results from equation 6.2 in figure 6.10. A comparison of the temperature-time relation is not presented since the calculations of Tampere were performed with different values for the specific heat capacity and the thermal conductivity and therefore yield deviating results. Since correct values of electrical resistivity were used to calculate the current-time relation, it was possible to compare these results to the calculations performed in this report.

Figure 6.10 illustrates that during the first 9 seconds the current development calculated in section 6.2 (indicated as simulated current) matches the results of Tampere (indicated as reference current). After 9 seconds, the simulated current decreases faster than the reference current.

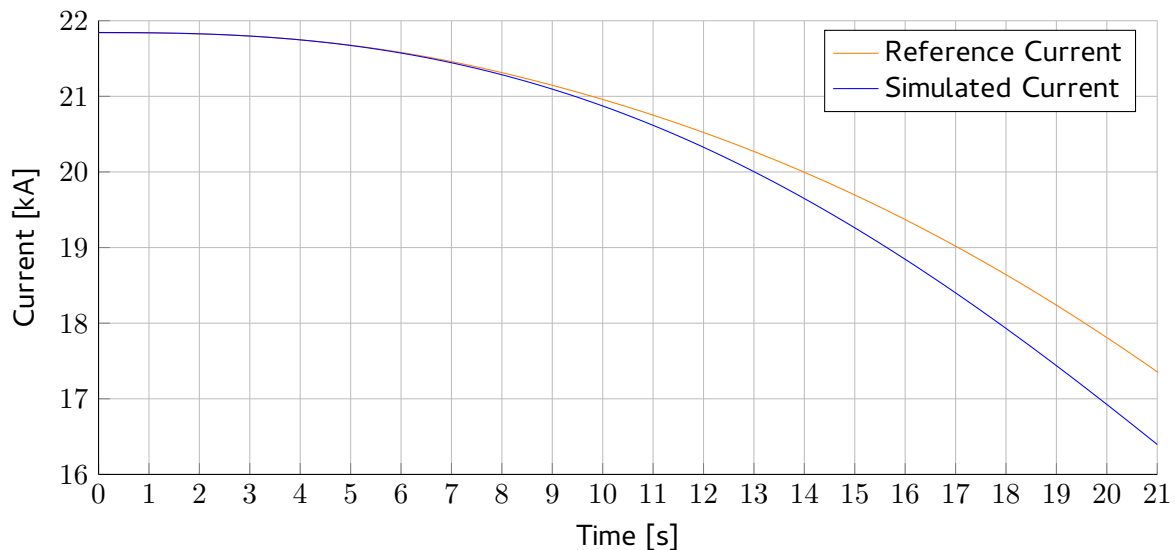


Figure 6.10: Current as a function of time for one coil of the double racetrack working model (section 4.4). The reference current is the time-current relation obtained by Tampere and the simulated current is acquired by the model described in section 6.2.

6.4 Conclusion

The purpose of the temperature calculations performed in this section is to provide insight in the quench behaviour of both the double racetrack and the solenoid system. Although the calculations are based on estimations, it has become clear for both systems that the peak temperature achieved after quenching is far above the safe limit. However, it is possible that the purity of the used Aluminium has affected the temperature calculations in a negative way. The results presented in this section can be used as a starting point for a more detailed study which has to be performed after decisions are made concerning the final magnet design.

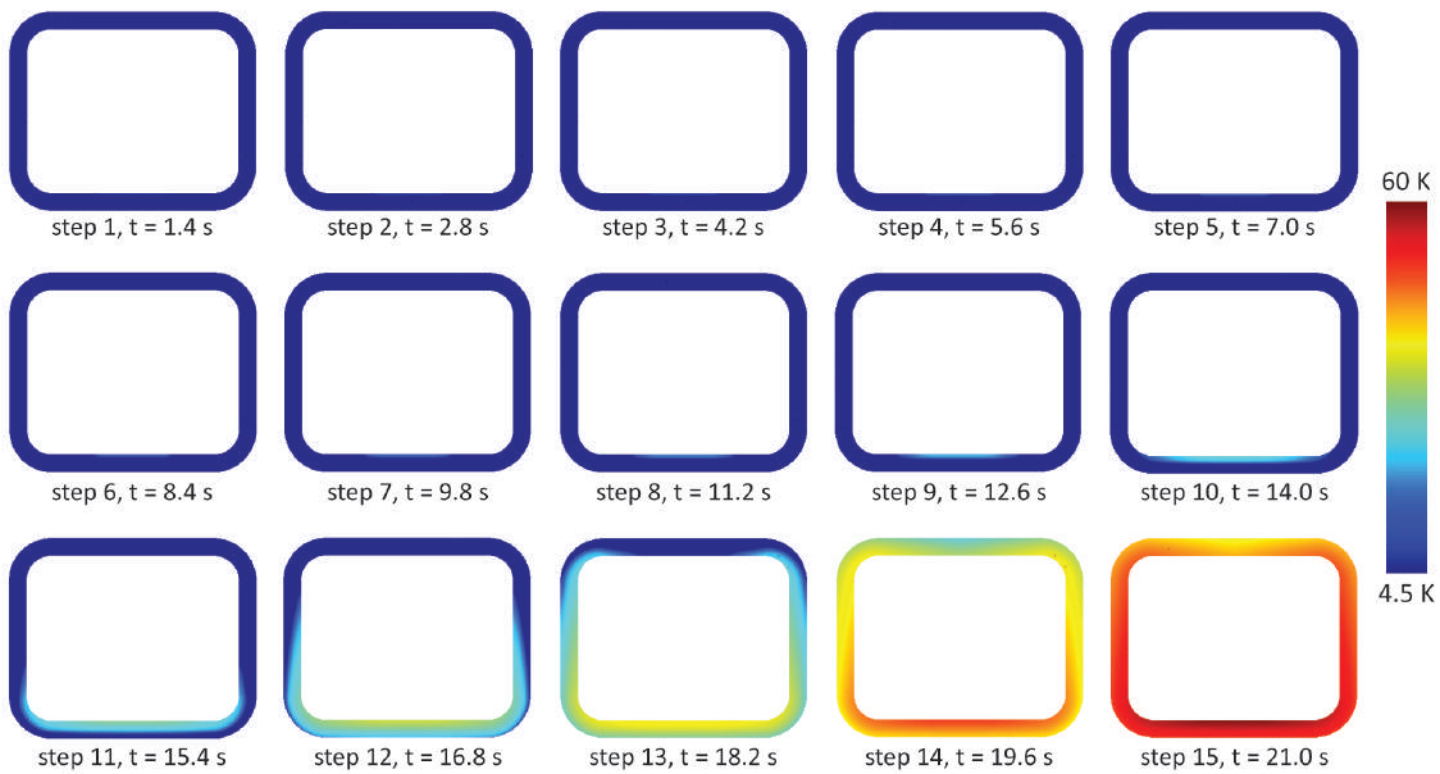


Figure 6.11: Graphical representation of the heat distribution after quenching for one coil of the double racetrack working model (section 4.4). Note that the heat spreads relatively homogeneous over the coil volume.

7 Mechanical Analysis

To obtain insight in the magnitude of the forces exerted on the conductor windings and the mechanical structure needed to take them away, a mechanical model was constructed for both design options. This chapter describes the layout of the mechanical models and presents the results of the force, deformation and stress calculations which are performed by means of a finite element method.

7.1 Forces

Due to their large operating current density (J_{op}), the conductor windings of both the double racetrack and solenoid working model (section 4.4 and 5.4) experience relatively large forces. To obtain insight in the order of magnitude of these forces, some rough calculations were performed. These estimations are based on the assumption that the coils of both systems can be pictured as two infinitely long current-carrying wires. Because the estimated magnitude of the forces were indeed very large, a more accurate calculation was performed for different sections of the working models using a finite element method (see table 7.1). Forces of this magnitude can cause serious damage to the conductor windings. It is therefore important to take them away from the coils using a mechanical structure.

Table 7.1: Calculated forces for different sections of the double racetrack and solenoid working model.

Configuration	Description	Estimated Force	Calculated Force
Double Racetrack	Total force exerted in the z-direction on a single racetrack coil. The force is directed towards the other racetrack.	17.8 MN	37.4 MN
Double Racetrack	Total force exerted in the y-direction on one half of a single racetrack coil (like hoop stress).	-	50.4 MN
Solenoid	Total force exerted in the y-direction on one of the long sides of the solenoid. The force is directed outwards.	27.0 MN	51.8 MN

7.2 Structure

To take away the forces from the conductor windings, a mechanical structure is needed. As explained in section 2.3.5 it is favourable to place this structure within the cryostat to reduce the heat leak. To obtain insight in the kind of mechanical structure needed to withstand the forces exerted on the coils, a mechanical model was constructed for both working models. The mechanical structures, created by means of COMSOL Multiphysics, are presented in figures 7.1 and 7.2. The structures are modelled using stainless steel (AISI Type 304) and are part of the cold mass of the magnet system. In order to meet the requirements concerning the accessibility of the detector volume, holes are incorporated at the top and for the double racetrack also at the side planes of the structure. Since arbitrary choices were

made in terms of shape and support, the calculations based on these structures can only be seen as estimations. However, they provide some useful insights regarding the amount of mechanical structure needed to take away the forces and protect the system from deformation.

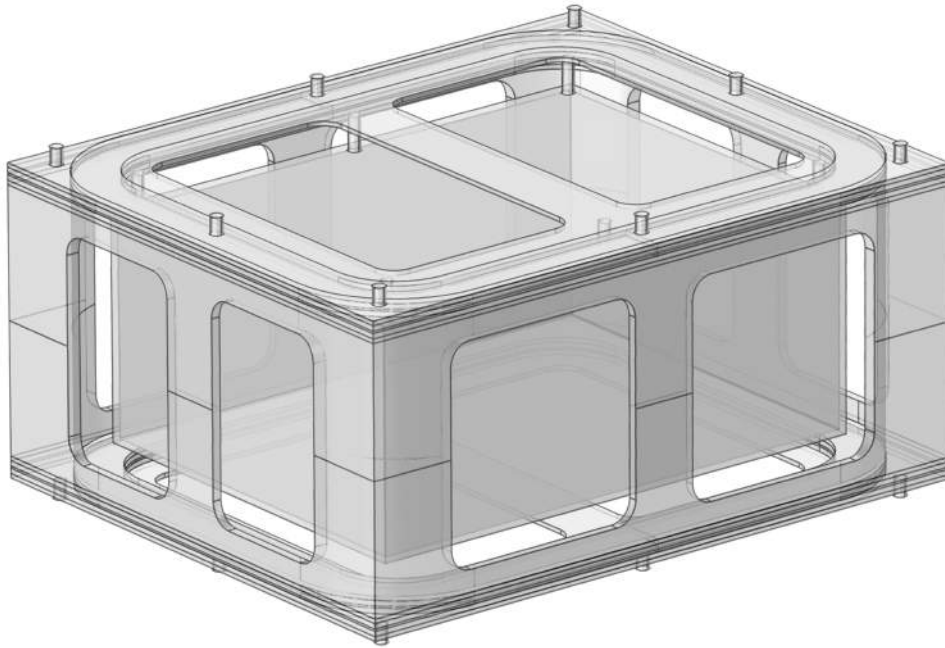


Figure 7.1: Mechanical structure of the double racetrack working model.

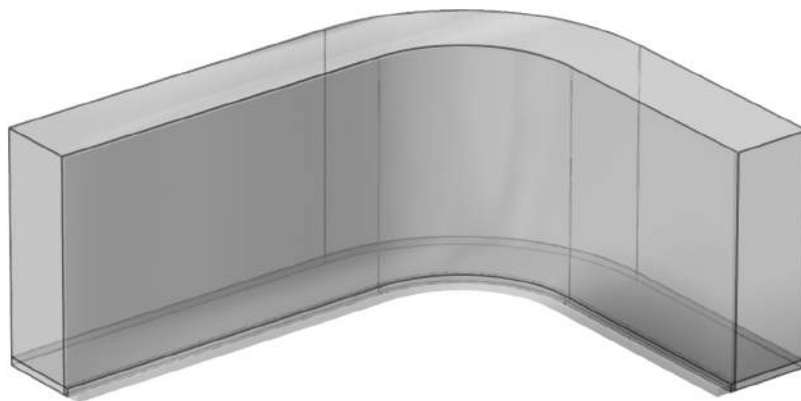


Figure 7.2: Mechanical structure of the solenoid working model.

7.3 Deformation and Von Mises stress

The mechanical models described in section 7.2 were used to perform calculations of the deformation and von Mises stress of the mechanical structures. The results are presented in this section.

7.3.1 Von Mises stress

The von Mises stress is a scalar stress value that is used to predict yielding of materials under any loading condition [31]. When the von Mises stress exceeds the yield strength of a material, the material will start to deform [32]. The calculated von Mises stresses are presented in table 7.2. Because the yield strength of the used stainless steel (AISI Type 304) is 215 MPa [33], this type of material can be used without any risk of deformation due to internal stresses.

Table 7.2: Calculated von Mises stress for the mechanical structures of the double racetrack and solenoid working model.

Configuration		von Mises stress
Double racetrack	cubic structure	20 MPa
	central beam	60 MPa
Solenoid		42 MPa

Since both mechanical structures are based on some arbitrary choices concerning the thickness and shape of different parts, these calculations are far from accurate. However, they provide some information about the order of magnitude of the internal stress.

7.3.2 Deformation

Deformation of a mechanical structure is only approved to a certain extent since it affects the stability of the system. To obtain insight in the relation between the deformation and the thickness of the mechanical structure, both structures are designed in such a way that their displacement (which is a measure of the deformation) is approximately equal. This common displacement is set to a safe value of 4 mm. Figures 7.3 and 7.4 present the calculated displacement field for the double racetrack and solenoid structure respectively. Both figures illustrate that it is possible to decrease the displacement to a safe value of several millimetres. However, it should be noted that in order to achieve this specific displacement for the solenoid system, a steel wall with a thickness of 1 m is required. The double racetrack configuration requires a relatively smaller wall with a thickness of 20 cm. Since the double racetrack has a very 'open' structure, the volume of steel needed for this displacement is only a small fraction of the volume of steel needed to support the solenoid.

The dimensions of the mechanical structure needed to take the forces from the solenoid system are very large. Therefore the size but also the weight of the total magnet system increases, which is undesirable. A solution to this problem is to replace the rectangle solenoid by a 'normal', circular solenoid. This does not directly imply that the shape of the detector volume has to be changed, but since a circular magnet system around a cubic detector will occupy an enormous amount of space, it is more convenient to change the shape of the detector volume. For comparison, the thickness of the structure needed to support a circular solenoid which encloses the same detector volume and generates a similar magnetic field as the rectangle solenoid is calculated. It turned out that for the circular solenoid a steel wall with a thickness of 1 cm was sufficient to reduce the peak displacement to 2 mm.

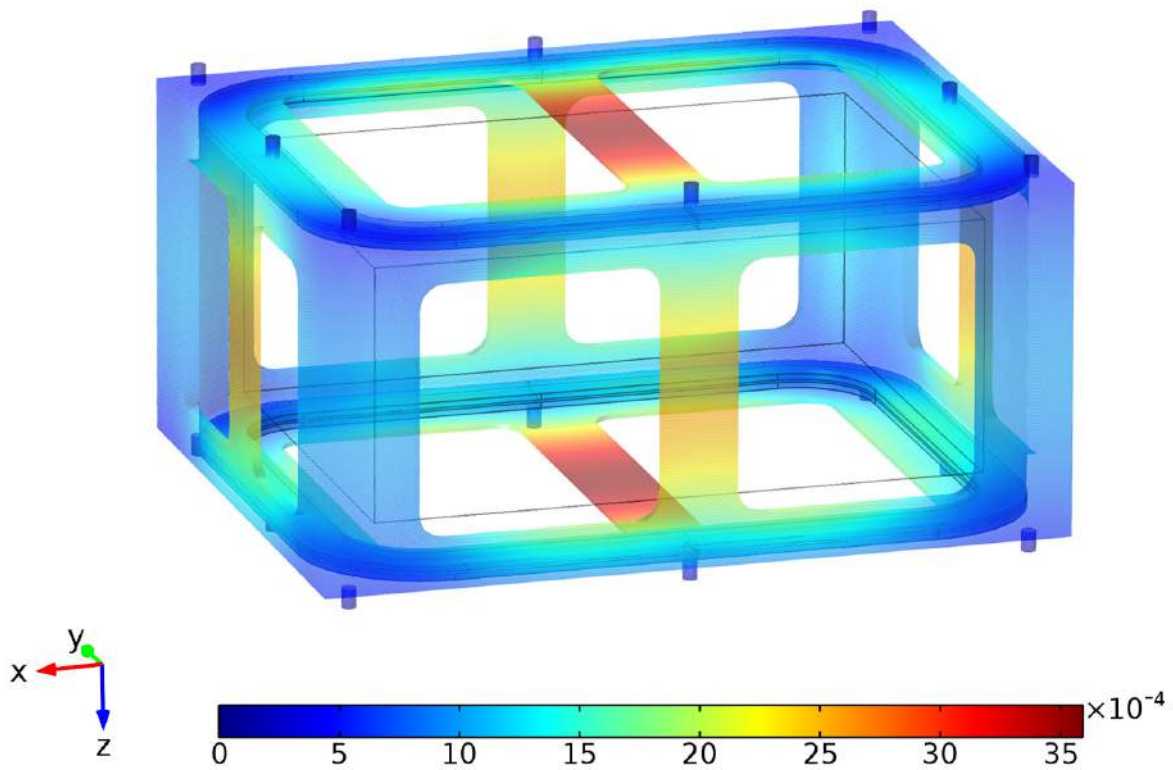


Figure 7.3: Surface plot of the total displacement [m] of the mechanical structure of the double racetrack configuration. The thickness of the surrounding steel wall is 20 cm. Note that due to their small cross-sectional area, the maximum displacement occurs at the central beams.

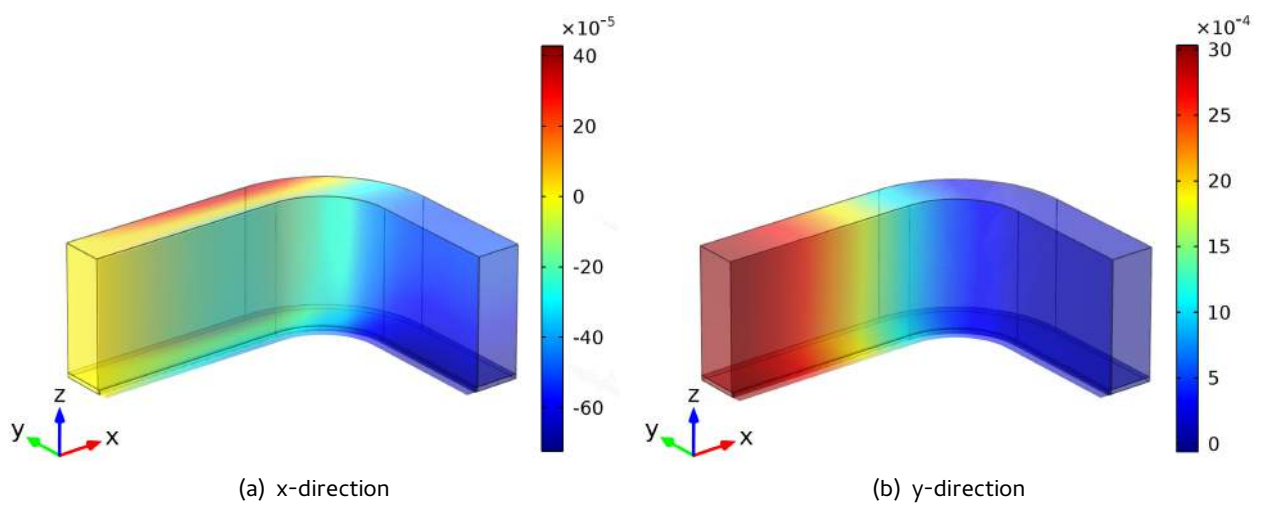


Figure 7.4: Surface plot of the displacement [m] in the x-direction and y-direction of $\frac{1}{8}$ of the mechanical structure of the solenoid system. The thickness of the surrounding steel wall is 1 m. Note that the displacement in the x-direction is much smaller than the displacement in the y-direction.

7.4 Conclusion

A mechanical analysis has been performed to study the mechanical properties of both working models. Although arbitrary choices were made concerning the shape and size of the mechanical structures, the calculations provided some useful insight regarding the amount of mechanical structure needed to take away the forces and protect the system from deformation. From the calculations it has become clear that the volume of mechanical structure needed to protect the solenoid system is more than five times as large as the volume needed to protect the double racetrack configuration. Furthermore, the calculated von Mises stress for both structures turned out to be much smaller than the yield strength of the material used to model the structures. The results presented in this section can be used as a starting point for a more detailed mechanical study which has to be performed after decisions are made concerning the final magnet design.

Conclusion

The goal of this assignment was to perform a design optimization of a new superconducting magnet system for a liquid Argon neutrino detector. The optimization study was focused on two design options, a double racetrack configuration and a uniformly wound solenoid. Both design options were optimized with respect to the magnetic field requirements and a parametric study was performed to obtain insight in the relations between the geometrical parameters and the shape and magnitude of the magnetic field.

The result of the optimization study is a set of optimized models for both the double racetrack and the solenoid option. As a result of the performed parametric sweeps, all models have a different geometry and satisfy different design requirements.

The obtained solenoid models all satisfy the imposed magnetic field requirements, but have a different operating current density and differ in homogeneity. The homogeneity is related to the height of the solenoid. A larger height leads to a more homogeneous system, but it should be noted that the magnetic field generated by the solenoid system will never become truly homogeneous. The optimization study for the solenoid was performed for two types of conductors, Nb-Ti and MgB₂. It turned out that it is possible to meet the magnetic field requirements by application of both materials, while respecting the imposed safety margins.

For the double racetrack configuration, the magnitude of the magnetic field at the center of the detector volume is equal for all models, but the magnitude at the edges of the detector volume differs. This value is related to the coil dimensions and becomes larger for increasing coil lengths. The optimization illustrated that due to decoupling of the coil lengths and the magnetic field magnitudes at the edges of the conductor volume, the double racetrack system can be seen as a combination of two independent two-dimensional planes. Furthermore, the magnetic field generated by all double racetrack models is homogeneous to a large extent.

From the mechanical and thermal analysis performed for both systems it can be concluded that construction and operation of both design options is only possible when some strong measures are taken concerning quench protection and mechanical support.

Discussion and Recommendations

Since the final requirements for the superconducting magnet system are at present not fully defined, it is impossible to choose an optimal design from the set of optimized models for both the double racetrack and solenoid system. In order to define the final requirements an additional iteration with the people designing the detector itself is necessary. The results presented in this report serve as a basis for such an iteration and form a starting point for future design studies.

Acknowledgements

First, I would like to thank my supervisor Herman Ten Kate for giving me the opportunity to perform my bachelor assignment at the ATLAS magnet group at CERN. I would also like to show gratitude to my second supervisor, Alexey Dudarev who supported me during my daily work.

Next, I would like to thank to Erkki Härö from Tampere University, for testing his quench code on our system providing useful data.

Last, but certainly not least, I would like to thank Jeroen van Nugteren for all his help concerning my assignment and the mental support he provided during the completion of this thesis. Cheers!

Bibliography

- [1] "Standard Model infographic." available from: http://www.isgtw.org/sites/default/files/Standard_model_infographic.png.
- [2] J. Nugteren van, "Internship Report: CERN, Software development for the Science and Design behind Superconducting Magnet Systems," tech. rep., Twente University: Energy Materials and Systems and CERN: ATLAS magnet team, 2011.
- [3] B. Pontecorvo, "Neutrino Experiments and the Problem of Conservation of Leptonic Charge," *reproduced and translated in Sov. Phys. JETP*, 1968.
- [4] C. Rubbia, "The Liquid-Argon Time Projection Chamber: a new concept for Neutrino Detectors," *CERN-EP*, 1977.
- [5] "A computer-generated detailed view of the ATLAS detector." available from: <http://www.atlas.ch/photos/full-detector-old.html>.
- [6] M. Wilson, *Superconducting Magnets*. Oxford Science Publications, 2nd ed., March 1987.
- [7] T. Berlincourt and R. Hake, "Pulsed-Magnetic-Field Studies of Superconducting Transition Metal Alloys at High and Low Current Densities," *Bull. Am. Phys. Soc. II* 7 408, 1962.
- [8] L. Bottura, "A Practical Fit for the Critical Surface of NbTi," *CERN, LHC-Division: IEEE Transactions on applied superconductivity*, vol. 10, March 2000.
- [9] Columbus Superconductors, *What has already been done*.
- [10] C. Buzea and T. Yamashita, "Review of the superconducting properties of MgB₂," *Superconductor Science and Technology*, vol. 14, pp. 115–146, 2001.
- [11] W. Fietz and W. Webb, "Hysteresis in superconducting alloys-temperature and field dependence of dislocation pinning in niobium alloys," *Physical Review*, vol. 178, pp. 657–667, February 1969.
- [12] F. Hovell, "Design estimates for a medium-sized SMES system based on different superconducting materials," Master's thesis, University of Twente, November 2008.
- [13] D. Griffiths, *Introduction to Electrodynamics*. Prentice Hall, third ed., 1999.
- [14] R. Feynman, R. Leighton, and M. Sands, *The Feynman Lectures on Physics*, vol. 2. Addison-Wesley Publishing Company, 1964.
- [15] ATLAS Magnet Project Collaboration, "ATLAS Barrel Toroid technical design report," tech. rep., CERN, 1997.
- [16] J. Hook and H. Hall, *Solid State Physics*. Manchester Physics Series, Wiley, second ed., 1991.

- [17] H. Ten Kate, "Superconductors for application in detector magnets," April 2013. Available from: <https://indico.cern.ch/event/301339/session/9/contribution/17/material/slides/1.pdf>.
- [18] V. Parma, "Cryostat design," May 2013. available from: <https://cas.web.cern.ch/cas/Erice-2013/Lectures/Ericelectures.htm>.
- [19] L. Greengard, "The rapid evaluation of potential fields in particle systems," tech. rep., Cambridge, 1988.
- [20] T. Flynn, *Cryogenic Engineering*. CRC Press, 2nd ed., November 2004.
- [21] K. Levenberg, "A Method for the Solution of Certain Problems in Least-Squares," *Quarterly Applied Mathematics* 2, pp. 164–168, 1944.
- [22] D. Marquardt, "An algorithm for least-squares estimation of nonlinear parameters," *SIAM Journal Applied Mathematics*, vol. 11, pp. 431–441, 1963.
- [23] ATLAS Magnet Project Collaboration, "ATLAS End-Cap Toroids technical design report," tech. rep., CERN, 1997.
- [24] A. Bejan, *Heat Transfer*. John Wiley & Sons, Inc, 1993.
- [25] D. Mann, ed., *LNG Materials and Fluids*. National Bureau of Standards, Cryogenics Division, First ed., 1977.
- [26] J. Hulst, *Thermal Conductivity Of Glass Fiber/Epoxy Composite Support Bands For Cryogenic Dewars*. Phase II NBS, Boulder 1984.
- [27] N. Simon, E. Drexler, and R. Reed, "Properties of Copper and Copper Alloys at Cryogenic Temperature," *NIST Monograph 177*, pp. 7–23, February 1992.
- [28] Eckels Engineering, *CryoComp 5.2 for Windows*.
- [29] B. Coleman and V. Mizel, "Thermodynamics and departures from fourier's law of heat conduction," *Archive for Rational Mechanics and Analysis*, vol. 13, no. 1, pp. 245–261, 1963.
- [30] L. F. Shampine and M. W. Reichelt, "The MATLAB ODE Suite," *SIAM Journal on Scientific Computing*, vol. 18, pp. 1–22, 1997.
- [31] R. von Mises, "Mechanik der festen Korper im plastich deformablen Zustand," *Gottin. Nachr. Math. Phys.*, vol. 1, pp. 582–592, 1913.
- [32] R. Hibbler, *Mechanics of Materials*. Prentice-Hall, 6th ed., 2005.
- [33] P. Harvey, ed., *Engineering Properties of Steels*. American Society for Metals, 1982.
- [34] S. Russenschuck, *Field Computation for Accelerator Magnets*. Wiley-VCH, 2010.
- [35] D. Brandt, *Proceedings of the CAS-CERN Accelerator School: Magnets, Bruges, Belgium, 16-25 June 2009*. CERN, April 2010.

Appendix A Field Harmonics

The optimization of the homogeneity is performed using two dimensional coil harmonics, a concept often used for the optimization of the field quality inside the aperture of accelerator magnets[34]. The magnetic field in the aperture of an accelerator magnet is governed by the Laplace equation and can be described by a set of Fourier coefficients which are also known as field harmonics. Each coefficient represents the magnitude of a specific harmonic and the total magnetic field within the aperture is defined in terms of a Fourier series.

To calculate the individual Fourier coefficients, A_{ncen} and B_{ncen} , for the central region of the magnet, the coils are approximated by simple straight line-current elements. The magnitude of the coefficients is obtained by summing over the contributions of all line-current elements. The contribution of each line current is defined as

$$A_{ncen}(r_0) = \frac{\mu_0 I}{2\pi r_c} \left(\frac{r_0}{r_c}\right)^{n-1} \sin(n\varphi_c), \quad (\text{A.1})$$

$$B_{ncen}(r_0) = \frac{\mu_0 I}{2\pi r_c} \left(\frac{r_0}{r_c}\right)^{n-1} \cos(n\varphi_c), \quad (\text{A.2})$$

where μ_0 is the permeability of vacuum, I is the current in the line element, r_c is the relative radial position coordinate of the element, φ is the relative azimuthal coordinate of the element, n is an integer value that corresponds to a specific harmonic constant of the field and r_0 is the reference radius, which can be chosen arbitrarily (but in this report is set to the common ratio of 2/3 of the aperture).

The total field in the central region of the magnet, which is a superposition of the field contribution of the individual coefficients, is given by

$$B_r(r, \varphi) = \sum_{n=1}^{\infty} \left(\frac{r}{r_0}\right)^{n-1} (B_{ncen}(r_0)\sin(n\varphi) + A_{ncen}(r_0)\cos(n\varphi)), \quad (\text{A.3})$$

$$B_\varphi(r, \varphi) = \sum_{n=1}^{\infty} \left(\frac{r}{r_0}\right)^{n-1} (B_{ncen}(r_0)\cos(n\varphi) - A_{ncen}(r_0)\sin(n\varphi)), \quad (\text{A.4})$$

where B_r and B_φ are the field components in cylindrical coordinates. It is important to note that due to the presence of n in the exponential function, the influence of higher order harmonics on the magnetic field components is negligible.

In order to optimize the field quality in the center of the magnet all the undesired harmonics have to

be reduced to zero. To achieve a homogeneous magnetic field in the center of the magnet studied in this report, all harmonics except of the dipole field have to be reduced to zero by changing the relative positions of the coils. Since the influence of higher order harmonics is very small, this can be achieved by reducing B_{3cen} to zero.

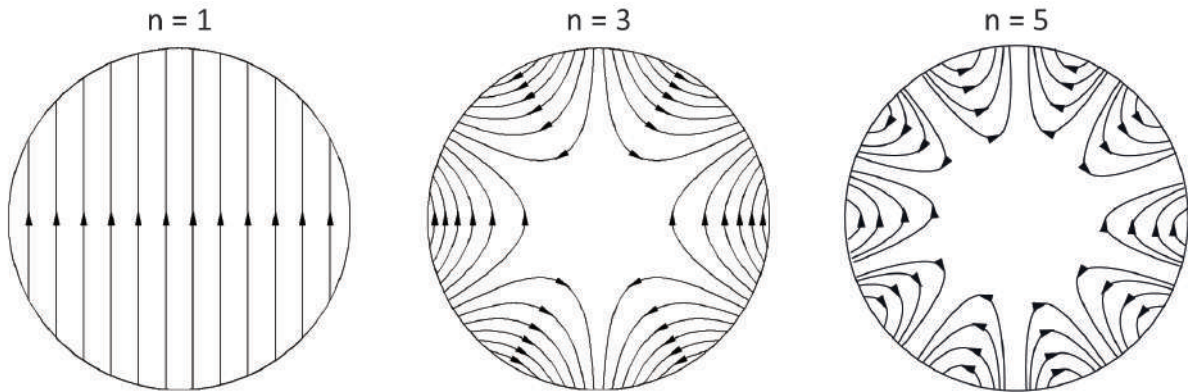


Figure A.1: Harmonic fields: dipole, hexapole, decapole. Adapted from Brandt [35]

Appendix B Data Tables

B.1 Double racetrack configuration: Parametric study R and Bedgreq

Table B.1: Properties of the optimized models for the parametric sweep over R and Bedgreq. Model 1 - 40.

id	Bedgreq	R	L1	L2	hsplit	dcoil	Bcen	Bedge	B3	Vc	Bpeak	Jop
1	0.500	1.00	11.41	8.55	5.22	0.92	1.0	0.500	3.7e-09	17.9	5.13	28.9
2	0.500	1.25	11.43	8.57	5.22	0.90	1.0	0.500	-2.2e-08	17.3	5.10	29.6
3	0.500	1.50	11.46	8.59	5.22	0.88	1.0	0.500	-1.3e-07	16.7	5.07	30.3
4	0.500	1.75	11.48	8.61	5.22	0.86	1.0	0.500	1.1e-08	16.2	5.04	30.8
5	0.500	2.00	11.49	8.62	5.22	0.85	1.0	0.500	2.3e-09	15.8	5.02	31.3
6	0.525	1.00	11.54	8.68	5.30	0.95	1.0	0.525	3.2e-06	18.6	5.14	28.6
7	0.525	1.25	11.56	8.70	5.30	0.92	1.0	0.525	-4.3e-10	17.9	5.11	29.4
8	0.525	1.50	11.59	8.72	5.30	0.90	1.0	0.525	-7.1e-08	17.3	5.07	30.1
9	0.525	1.75	11.61	8.73	5.30	0.88	1.0	0.525	-6.4e-08	16.8	5.05	30.6
10	0.525	2.00	11.63	8.75	5.30	0.86	1.0	0.525	-3.7e-06	16.3	5.03	31.1
11	0.550	1.00	11.67	8.81	5.38	0.96	1.0	0.550	-1.3e-05	19.2	5.15	28.4
12	0.550	1.25	11.69	8.83	5.38	0.94	1.0	0.550	7.2e-09	18.5	5.12	29.2
13	0.550	1.50	11.71	8.85	5.39	0.92	1.0	0.550	1.7e-08	17.9	5.08	29.9
14	0.550	1.75	11.73	8.87	5.39	0.90	1.0	0.550	5.8e-08	17.4	5.06	30.4
15	0.550	2.00	11.75	8.88	5.39	0.88	1.0	0.550	9.4e-08	16.9	5.04	30.9
16	0.575	1.00	11.81	8.95	5.47	0.98	1.0	0.575	1.3e-08	19.8	5.15	28.5
17	0.575	1.25	11.81	8.99	5.56	0.96	1.0	0.575	4.4e-03	19.3	5.12	29.2
18	0.575	1.50	11.86	8.99	5.48	0.94	1.0	0.575	1.4e-04	18.6	5.10	29.7
19	0.575	1.75	11.87	9.00	5.47	0.92	1.0	0.575	-3.2e-08	18.1	5.07	30.2
20	0.575	2.00	11.89	9.01	5.47	0.90	1.0	0.575	-7.8e-09	17.6	5.05	30.7
21	0.600	1.00	11.96	9.10	5.56	1.00	1.0	0.600	-2.4e-07	20.6	5.16	28.2
22	0.600	1.25	11.99	9.13	5.57	0.97	1.0	0.600	1.2e-08	19.8	5.12	29.1
23	0.600	1.50	12.02	9.15	5.62	0.96	1.0	0.600	2.6e-03	19.5	5.11	29.4
24	0.600	1.75	12.03	9.15	5.56	0.94	1.0	0.600	-5.1e-09	18.8	5.08	30.0
25	0.600	2.00	12.05	9.16	5.56	0.93	1.0	0.600	5.9e-09	18.3	5.06	30.4
26	0.625	1.00	12.11	9.26	5.67	1.03	1.0	0.625	4.9e-08	21.4	5.17	28.1
27	0.625	1.25	12.13	9.29	5.67	1.00	1.0	0.625	4.4e-09	20.6	5.13	28.9
28	0.625	1.50	12.16	9.31	5.67	0.97	1.0	0.625	-2.6e-08	19.9	5.10	29.6
29	0.625	1.75	12.17	9.32	5.67	0.96	1.0	0.625	9.5e-08	19.6	5.09	29.8
30	0.625	2.00	12.18	9.33	5.67	0.95	1.0	0.625	-1.8e-08	19.1	5.07	30.1
31	0.650	1.00	12.28	9.43	5.77	1.05	1.0	0.650	-2.1e-08	22.4	5.18	27.9
32	0.650	1.25	12.31	9.46	5.77	1.02	1.0	0.650	7.6e-08	21.5	5.14	28.6
33	0.650	1.50	12.33	9.48	5.78	1.00	1.0	0.650	-7.9e-09	20.8	5.11	29.3
34	0.650	1.75	12.36	9.50	5.78	0.98	1.0	0.650	6.4e-08	20.2	5.09	29.9
35	0.650	2.00	12.37	9.50	5.77	0.96	1.0	0.651	-6.7e-05	19.7	5.07	30.3
36	0.675	1.00	12.44	9.60	5.88	1.08	1.0	0.675	5.6e-09	23.4	5.19	27.6
37	0.675	1.25	12.47	9.63	5.89	1.05	1.0	0.675	-6.3e-09	22.5	5.15	28.4
38	0.675	1.50	12.50	9.66	5.89	1.02	1.0	0.675	4.7e-09	21.8	5.12	29.1
39	0.675	1.75	12.52	9.67	5.89	1.00	1.0	0.675	3.3e-08	21.1	5.10	29.6
40	0.675	2.00	12.54	9.69	5.89	0.99	1.0	0.675	1.8e-08	20.6	5.08	30.1

Table B.2: Properties of the optimized models for the parametric sweep over R and Bedgereq. The working model is indicated in yellow. Model 41 - 85.

id	Bedgereq	R	L1	L2	hsplit	dcoil	Bcen	Bedge	B3	Vc	Bpeak	Jop
41	0.700	1.00	12.64	9.79	6.00	1.11	1.0	0.700	-3.5e-07	24.5	5.20	27.3
42	0.700	1.25	12.67	9.82	6.01	1.08	1.0	0.700	9.8e-08	23.6	5.17	28.1
43	0.700	1.50	12.68	9.84	6.01	1.05	1.0	0.700	-4.2e-06	22.8	5.14	28.8
44	0.700	1.75	12.71	9.86	6.01	1.03	1.0	0.700	1.8e-07	22.1	5.11	29.4
45	0.700	2.00	12.73	9.87	6.01	1.02	1.0	0.700	2.8e-07	21.6	5.09	29.8
46	0.725	1.00	12.84	10.00	6.14	1.15	1.0	0.725	3.5e-08	25.8	5.22	27.1
47	0.725	1.25	12.87	10.03	6.14	1.11	1.0	0.725	3.5e-08	24.8	5.18	27.9
48	0.725	1.50	12.90	10.05	6.14	1.09	1.0	0.725	2.8e-08	24.0	5.15	28.5
49	0.725	1.75	12.92	10.07	6.14	1.06	1.0	0.725	-2.6e-08	23.3	5.12	29.1
50	0.725	2.00	12.94	10.08	6.14	1.05	1.0	0.725	-5.3e-08	22.7	5.10	29.5
51	0.750	1.00	13.07	10.25	6.30	1.19	1.0	0.750	9.4e-07	27.3	5.23	26.8
52	0.750	1.25	13.11	10.28	6.30	1.15	1.0	0.750	5.6e-10	26.3	5.20	27.5
53	0.750	1.50	13.12	10.31	6.30	1.13	1.0	0.750	-1.3e-06	25.5	5.17	28.1
54	0.750	1.75	13.14	10.32	6.30	1.10	1.0	0.750	-4.1e-07	24.7	5.14	28.7
55	0.750	2.00	13.16	10.34	6.30	1.09	1.0	0.750	-2.4e-08	24.2	5.12	29.1
56	0.775	1.00	13.31	10.51	6.46	1.23	1.0	0.775	8.0e-08	28.9	5.25	26.5
57	0.775	1.25	13.35	10.54	6.46	1.20	1.0	0.775	-2.5e-08	27.9	5.21	27.2
58	0.775	1.50	13.38	10.56	6.46	1.17	1.0	0.775	-4.7e-08	27.1	5.18	27.8
59	0.775	1.75	13.40	10.58	6.46	1.15	1.0	0.775	4.1e-08	26.3	5.16	28.3
60	0.775	2.00	13.42	10.60	6.46	1.13	1.0	0.775	1.4e-08	25.7	5.14	28.7
61	0.800	1.00	13.61	10.79	6.64	1.28	1.0	0.800	-5.5e-08	30.9	5.26	26.1
62	0.800	1.25	13.65	10.83	6.64	1.24	1.0	0.800	2.9e-08	29.8	5.23	26.9
63	0.800	1.50	13.67	10.85	6.64	1.22	1.0	0.800	-4.6e-08	28.9	5.20	27.4
64	0.800	1.75	13.69	10.87	6.65	1.19	1.0	0.800	1.7e-08	28.1	5.18	28.0
65	0.800	2.00	13.71	10.89	6.64	1.17	1.0	0.800	1.4e-08	27.4	5.16	28.4
66	0.825	1.00	13.92	11.14	6.86	1.34	1.0	0.825	-2.5e-06	33.3	5.28	25.7
67	0.825	1.25	13.96	11.17	6.86	1.30	1.0	0.825	-9.8e-09	32.1	5.25	26.5
68	0.825	1.50	13.98	11.20	6.86	1.27	1.0	0.825	-1.7e-09	31.2	5.22	27.0
69	0.825	1.75	14.01	11.22	6.86	1.25	1.0	0.825	-9.7e-08	30.3	5.19	27.6
70	0.825	2.00	14.03	11.24	6.86	1.23	1.0	0.825	-6.0e-08	29.5	5.17	28.0
71	0.850	1.00	14.32	11.55	7.12	1.41	1.0	0.850	-3.4e-08	36.4	5.30	25.3
72	0.850	1.25	14.36	11.59	7.13	1.37	1.0	0.850	-5.3e-08	35.0	5.27	26.0
73	0.850	1.50	14.39	11.62	7.13	1.34	1.0	0.850	2.9e-08	33.9	5.24	26.7
74	0.850	1.75	14.42	11.64	7.13	1.31	1.0	0.850	4.3e-08	33.0	5.21	27.2
75	0.850	2.00	14.44	11.66	7.12	1.29	1.0	0.850	-2.1e-08	32.1	5.19	27.6
76	0.875	1.00	14.79	12.05	7.44	1.50	1.0	0.875	2.3e-08	40.0	5.32	24.9
77	0.875	1.25	14.83	12.08	7.44	1.45	1.0	0.875	2.0e-08	38.6	5.29	25.6
78	0.875	1.50	14.87	12.12	7.44	1.42	1.0	0.875	3.4e-08	37.4	5.26	26.2
79	0.875	1.75	14.90	12.14	7.44	1.39	1.0	0.875	-3.9e-08	36.4	5.23	26.7
80	0.875	2.00	14.92	12.16	7.44	1.37	1.0	0.875	4.6e-08	35.5	5.21	27.2
81	0.900	1.00	15.40	12.69	7.84	1.61	1.0	0.900	1.5e-08	45.1	5.35	24.4
82	0.900	1.25	15.44	12.73	7.84	1.56	1.0	0.900	3.0e-09	43.5	5.31	25.1
83	0.900	1.50	15.48	12.76	7.84	1.52	1.0	0.900	-2.4e-05	42.2	5.28	25.7
84	0.900	1.75	15.51	12.78	7.84	1.49	1.0	0.900	-1.1e-08	41.1	5.26	26.2
85	0.900	2.00	15.53	12.81	7.84	1.47	1.0	0.900	7.2e-08	40.1	5.24	26.6

B.2 Double racetrack configuration: Parametric study L1 and L2

Table B.3: Properties of the optimized models for the parametric sweep over L1 and L2.

id	L1	L2	R	hsplit	dcoil	Bcen	Bedge1	Bedge2	B3	Vc	Bpeak	Jop	$\int B_z \, dV$
1	11.0	8.0	1.5	4.85	0.79	1.0	0.40	0.37	1.9e-08	14.2	5.02	31.3	397.6
2	11.0	8.5	1.5	5.15	0.86	1.0	0.41	0.48	2.2e-09	15.8	5.06	30.5	454.5
3	11.0	9.0	1.5	5.45	0.91	1.0	0.42	0.58	3.2e-08	17.3	5.08	30.0	479.7
4	11.0	9.5	1.5	5.74	0.96	1.0	0.43	0.65	2.8e-04	18.9	5.11	29.4	481.8
5	11.0	10.0	1.5	6.01	1.01	1.0	0.43	0.72	4.9e-08	20.4	5.12	29.2	483.6
6	11.0	10.5	1.5	6.29	1.07	1.0	0.44	0.77	3.3e-08	22.1	5.14	28.7	483.2
7	11.0	11.0	1.5	6.55	1.12	1.0	0.45	0.81	6.2e-08	23.9	5.16	28.2	481.9
8	11.0	11.5	1.5	6.80	1.18	1.0	0.45	0.85	7.7e-08	25.8	5.19	27.7	480.4
9	11.0	12.0	1.5	7.03	1.23	1.0	0.46	0.87	4.1e-08	27.6	5.20	27.4	479.0
10	11.0	12.5	1.5	7.26	1.28	1.0	0.47	0.90	3.4e-08	29.4	5.22	27.0	477.7
11	11.0	13.0	1.5	7.47	1.34	1.0	0.47	0.92	-2.0e-08	31.3	5.24	26.6	476.5
12	12.0	8.0	1.5	4.87	0.82	1.0	0.61	0.37	3.6e-08	15.5	5.03	31.0	507.3
13	12.0	8.5	1.5	5.18	0.89	1.0	0.60	0.48	-5.8e-08	17.2	5.07	30.2	539.0
14	12.0	9.0	1.5	5.48	0.94	1.0	0.60	0.58	7.5e-08	18.9	5.10	29.6	546.0
15	12.0	9.5	1.5	5.78	0.99	1.0	0.60	0.65	-5.7e-09	20.4	5.11	29.3	537.3
16	12.0	10.0	1.5	6.07	1.05	1.0	0.60	0.72	-3.9e-08	22.1	5.13	28.8	529.5
17	12.0	10.5	1.5	6.35	1.11	1.0	0.60	0.77	1.2e-08	24.0	5.16	28.3	522.9
18	12.0	11.0	1.5	6.63	1.17	1.0	0.59	0.81	-1.4e-08	26.0	5.18	27.9	517.2
19	12.0	11.5	1.5	6.90	1.23	1.0	0.59	0.84	-8.3e-08	28.0	5.20	27.4	512.7
20	12.0	12.0	1.5	7.16	1.29	1.0	0.59	0.87	-4.9e-08	30.1	5.22	27.0	509.1
21	12.0	12.5	1.5	7.40	1.34	1.0	0.60	0.89	4.5e-09	32.0	5.24	26.7	506.1
22	12.0	13.0	1.5	7.64	1.39	1.0	0.59	0.91	2.1e-08	34.0	5.25	26.4	503.2
23	13.0	8.0	1.5	4.89	0.85	1.0	0.79	0.37	2.3e-08	16.9	5.06	30.5	509.2
24	13.0	8.5	1.5	5.20	0.91	1.0	0.77	0.48	4.7e-10	18.7	5.09	29.9	551.5
25	13.0	9.0	1.5	5.42	0.96	1.0	0.76	0.58	-5.0e-03	20.2	5.11	29.3	571.8
26	13.0	9.5	1.5	5.81	1.02	1.0	0.75	0.65	-4.4e-09	22.0	5.12	29.1	558.1
27	13.0	10.0	1.5	6.11	1.08	1.0	0.74	0.72	-6.6e-08	24.0	5.15	28.5	549.9
28	13.0	10.5	1.5	6.41	1.14	1.0	0.73	0.77	3.4e-08	26.0	5.17	28.0	543.0
29	13.0	11.0	1.5	6.69	1.21	1.0	0.72	0.81	3.4e-09	28.0	5.19	27.6	536.9
30	13.0	11.5	1.5	6.97	1.27	1.0	0.72	0.84	-2.9e-08	30.2	5.21	27.1	531.9
31	13.0	12.0	1.5	7.25	1.33	1.0	0.71	0.87	-3.1e-08	32.3	5.23	26.8	527.7
32	13.0	12.5	1.5	7.51	1.39	1.0	0.71	0.89	-6.4e-08	34.7	5.26	26.3	524.1
33	13.0	13.0	1.5	7.76	1.44	1.0	0.71	0.91	-4.2e-08	36.8	5.27	26.0	520.9
34	14.0	8.0	1.5	4.90	0.87	1.0	0.92	0.37	-9.7e-09	18.2	5.07	30.3	512.1
35	14.0	8.5	1.5	5.22	0.94	1.0	0.90	0.48	3.4e-08	20.1	5.10	29.6	555.8
36	14.0	9.0	1.5	5.53	0.99	1.0	0.88	0.58	-3.1e-08	21.7	5.11	29.4	570.1
37	14.0	9.5	1.5	5.84	1.05	1.0	0.87	0.65	1.3e-08	23.7	5.14	28.8	563.5
38	14.0	10.0	1.5	6.15	1.12	1.0	0.85	0.72	-3.9e-08	25.8	5.16	28.2	556.7
39	14.0	10.5	1.5	6.45	1.18	1.0	0.84	0.77	4.5e-08	27.9	5.18	27.8	550.9
40	14.0	11.0	1.5	6.75	1.24	1.0	0.83	0.81	-9.7e-09	30.2	5.21	27.3	546.1
41	14.0	11.5	1.5	7.04	1.31	1.0	0.82	0.84	1.5e-08	32.4	5.23	26.9	541.9
42	14.0	12.0	1.5	7.32	1.37	1.0	0.81	0.87	1.7e-08	34.7	5.24	26.5	538.1
43	14.0	12.5	1.5	7.59	1.43	1.0	0.80	0.89	-2.4e-10	37.0	5.26	26.2	534.8
44	14.0	13.0	1.5	7.86	1.49	1.0	0.80	0.91	-6.2e-09	39.5	5.28	25.8	532.0
45	15.0	8.0	1.5	4.92	0.89	1.0	1.00	0.36	6.7e-08	19.5	5.08	30.1	511.6
46	15.0	8.5	1.5	5.23	0.96	1.0	0.98	0.48	4.3e-08	21.5	5.11	29.4	555.9
47	15.0	9.0	1.5	5.54	1.01	1.0	0.97	0.57	1.9e-08	23.3	5.12	29.1	570.0
48	15.0	9.5	1.5	5.86	1.08	1.0	0.95	0.65	-1.9e-08	25.4	5.15	28.5	564.4
49	15.0	10.0	1.5	6.17	1.15	1.0	0.93	0.72	1.4e-08	27.7	5.17	28.0	558.7
50	15.0	10.5	1.5	6.48	1.21	1.0	0.92	0.77	-8.1e-07	30.0	5.20	27.5	554.2
51	15.0	11.0	1.5	6.79	1.28	1.0	0.91	0.81	-2.5e-07	32.4	5.22	27.0	550.3
52	15.0	11.5	1.5	7.09	1.35	1.0	0.90	0.84	8.0e-10	34.8	5.24	26.6	546.9
53	15.0	12.0	1.5	7.38	1.41	1.0	0.89	0.87	3.2e-08	37.2	5.26	26.2	543.9
54	15.0	12.5	1.5	7.67	1.47	1.0	0.88	0.89	2.2e-08	39.6	5.27	25.9	541.0
55	15.0	13.0	1.5	7.95	1.53	1.0	0.87	0.91	1.2e-08	42.2	5.29	25.6	538.5

B.3 Solenoid configuration: Parametric study R and hcoil

Table B.4: Properties of the optimized models for the parametric sweep over R and hcoil. The working model is indicated in yellow.

id	hcoil	R	Bcen	Bedge1	Bedge2	B3	Je MgB ₂ 20 K	Je Nb-Ti 4.5 K	Vc	Bpeak	Jop
61	4.00	1.00	1.0	1.77	1.70	-2.58e-01	42.74	58.62	9.56	2.70	40.70
62	4.00	1.25	1.0	1.77	1.71	-2.58e-01	42.72	58.59	9.46	2.70	40.65
63	4.00	1.50	1.0	1.78	1.71	-2.58e-01	42.70	58.57	9.36	2.69	40.58
64	4.00	1.75	1.0	1.78	1.71	-2.58e-01	42.68	58.55	9.25	2.69	40.51
65	4.00	2.00	1.0	1.78	1.72	-2.58e-01	42.66	58.51	9.15	2.69	40.41
66	4.25	1.00	1.0	1.68	1.62	-2.50e-01	42.46	58.25	10.16	2.58	38.59
67	4.25	1.25	1.0	1.69	1.63	-2.49e-01	42.43	58.22	10.05	2.58	38.54
68	4.25	1.50	1.0	1.69	1.63	-2.49e-01	42.42	58.20	9.94	2.58	38.48
69	4.25	1.75	1.0	1.69	1.63	-2.49e-01	42.40	58.18	9.83	2.58	38.41
70	4.25	2.00	1.0	1.70	1.64	-2.49e-01	42.38	58.14	9.73	2.57	38.32
71	4.50	1.00	1.0	1.62	1.56	-2.41e-01	42.19	57.90	10.75	2.48	36.73
72	4.50	1.25	1.0	1.62	1.56	-2.41e-01	42.16	57.87	10.64	2.48	36.68
73	4.50	1.50	1.0	1.63	1.56	-2.41e-01	42.15	57.85	10.53	2.48	36.63
74	4.50	1.75	1.0	1.63	1.56	-2.40e-01	42.13	57.83	10.41	2.48	36.56
75	4.50	2.00	1.0	1.63	1.57	-2.40e-01	42.11	57.79	10.30	2.47	36.47
76	4.75	1.00	1.0	1.59	1.53	-2.32e-01	41.95	57.59	11.35	2.39	35.07
77	4.75	1.25	1.0	1.59	1.53	-2.32e-01	41.93	57.56	11.23	2.39	35.03
78	4.75	1.50	1.0	1.60	1.53	-2.32e-01	41.91	57.54	11.11	2.39	34.98
79	4.75	1.75	1.0	1.60	1.54	-2.32e-01	41.90	57.52	10.99	2.38	34.91
80	4.75	2.00	1.0	1.60	1.54	-2.31e-01	41.87	57.49	10.87	2.38	34.83
81	5.00	1.00	1.0	1.53	1.47	-2.23e-01	41.74	57.32	11.95	2.31	33.60
82	5.00	1.25	1.0	1.53	1.47	-2.23e-01	41.72	57.29	11.82	2.31	33.56
83	5.00	1.50	1.0	1.53	1.47	-2.23e-01	41.70	57.27	11.69	2.30	33.51
84	5.00	1.75	1.0	1.54	1.48	-2.23e-01	41.69	57.25	11.57	2.30	33.45
85	5.00	2.00	1.0	1.54	1.48	-2.23e-01	41.66	57.22	11.44	2.30	33.37
86	5.25	1.00	1.0	1.48	1.42	-2.15e-01	41.54	57.05	12.55	2.23	32.27
87	5.25	1.25	1.0	1.48	1.43	-2.15e-01	41.52	57.02	12.41	2.23	32.24
88	5.25	1.50	1.0	1.49	1.43	-2.15e-01	41.50	57.01	12.28	2.23	32.19
89	5.25	1.75	1.0	1.49	1.43	-2.14e-01	41.49	56.99	12.15	2.23	32.13
90	5.25	2.00	1.0	1.50	1.43	-2.14e-01	41.46	56.96	12.01	2.22	32.06
91	5.50	1.00	1.0	1.46	1.41	-2.06e-01	41.35	56.81	13.14	2.16	31.08
92	5.50	1.25	1.0	1.47	1.41	-2.06e-01	41.33	56.78	13.00	2.16	31.04
93	5.50	1.50	1.0	1.47	1.41	-2.06e-01	41.32	56.76	12.86	2.16	31.00
94	5.50	1.75	1.0	1.47	1.41	-2.06e-01	41.30	56.75	12.73	2.16	30.94
95	5.50	2.00	1.0	1.48	1.42	-2.06e-01	41.28	56.71	12.59	2.15	30.87
96	5.75	1.00	1.0	1.41	1.36	-1.98e-01	41.18	56.59	13.74	2.10	30.00
97	5.75	1.25	1.0	1.41	1.36	-1.98e-01	41.16	56.56	13.59	2.10	29.96
98	5.75	1.50	1.0	1.42	1.36	-1.98e-01	41.15	56.55	13.45	2.10	29.92
99	5.75	1.75	1.0	1.42	1.36	-1.98e-01	41.13	56.53	13.30	2.09	29.87
100	5.75	2.00	1.0	1.43	1.37	-1.98e-01	41.11	56.50	13.16	2.09	29.80
101	6.00	1.00	1.0	1.38	1.33	-1.90e-01	41.01	56.37	14.34	2.04	29.02
102	6.00	1.25	1.0	1.38	1.33	-1.90e-01	40.99	56.34	14.19	2.04	28.98
103	6.00	1.50	1.0	1.39	1.33	-1.90e-01	40.98	56.33	14.03	2.04	28.94
104	6.00	1.75	1.0	1.39	1.34	-1.90e-01	40.96	56.31	13.88	2.04	28.89
105	6.00	2.00	1.0	1.40	1.34	-1.90e-01	40.94	56.28	13.73	2.04	28.83
106	6.25	1.00	1.0	1.37	1.32	-1.82e-01	40.86	56.17	14.94	1.99	28.12
107	6.25	1.25	1.0	1.37	1.32	-1.82e-01	40.84	56.14	14.78	1.99	28.09
108	6.25	1.50	1.0	1.38	1.32	-1.82e-01	40.82	56.12	14.62	1.99	28.05
109	6.25	1.75	1.0	1.38	1.32	-1.82e-01	40.81	56.11	14.46	1.99	28.00
110	6.25	2.00	1.0	1.38	1.33	-1.82e-01	40.79	56.08	14.30	1.98	27.94
111	6.50	1.00	1.0	1.33	1.28	-1.74e-01	40.73	56.00	15.53	1.94	27.30
112	6.50	1.25	1.0	1.33	1.28	-1.74e-01	40.71	55.98	15.37	1.94	27.27
113	6.50	1.50	1.0	1.33	1.28	-1.74e-01	40.70	55.96	15.20	1.94	27.23
114	6.50	1.75	1.0	1.34	1.28	-1.74e-01	40.69	55.94	15.04	1.94	27.19
115	6.50	2.00	1.0	1.34	1.29	-1.74e-01	40.67	55.91	14.87	1.93	27.13